SIGNAL DETECTION AND SYNCHRONIZATION FOR ADVANCED MULTI-CARRIER SYSTEMS

A Thesis
Presented to
The Academic Faculty

By

Hyunwoo Cho

In Partial Fulfillment
of the Requirements for the Degree
Doctor of Philosophy in the
School of Electrical and Computer Engineering

Georgia Institute of Technology

December 2018

SIGNAL DETECTION AND SYNCHRONIZATION FOR ADVANCED MULTI-CARRIER SYSTEMS

Approved by:

Professor. Xiaoli Ma, Advisor
School of Electrical and Computer Engineering
Georgia Institute of Technology

Professor. Gee-Kung Chang
School of Electrical and Computer Engineering
Georgia Institute of Technology

Professor. John R. Barry
School of Electrical and Computer Engineering
Georgia Institute of Technology

Professor. Geoffrey Ye Li
School of Electrical and Computer Engineering
Georgia Institute of Technology

Professor. Hao-Min Zhou
School of Mathematics
Georgia Institute of Technology

Date Approved: November 5, 2018

To my family,

ACKNOWLEDGEMENTS

I would like to thank to my advisor Prof. Xiaoli Ma for her continuous support and encouragement during my Ph.D. study and research work. Through her training program, I can learn how to formulate the problems and to overcome challenges in the research. Without her leadership and mentoring, I could not achieve the goal. She always encouraged and inspired me when I had trouble with research problem.

I also would like to thank Prof. Gee-Kung Chang for his continuous support and great suggestions. He had given me a chance to work in FiWIN center. Collaboration with his group had a significant role in my Ph.D studies. I especially thank Dr. Feng Lu and Dr. Mu Xu from Prof. Chang's group for helping me understanding the radio-over-fiber systems and implementing prototypes. I also would like to thank Prof. John R. Barry, Prof. Geoffrey Ye Li, and Prof. Hao-Min Zhou for kindly accepting to serve on my thesis committee with useful comments.

I also would like to thank the members of my research group. Special thanks to Dr. Malik M. U. Gul for his help in implementing the test-bed, Dr. Qingsong Wen for his continuous friendship and support, and Yiming Kong for her useful comments and suggestions. Also I would like to thank Yahya M Alfadhli, Muhammad S Omar, Shuyi Shen, Rui Zhang, Shuang Yao, and Qi Zhou. I sincerely learned a lot from great discussions with them.

Last, I would like express special thanks my family, especially my wife. She is the energy of my life and helps me to overcome any difficulties during Ph.D studies.

TABLE OF CONTENTS

LIST OF TABLES

LIST OF FIGURES

SUMMARY

Orthogonal Frequency Division Multiplexing (OFDM) is widely adopted in modern wireless communication systems such as IEEE 802.11 wireless local area network (WLAN), long term evolution (LTE) in 4th generation (4G) network, and 5G new radio (5G-NR) systems. However, OFDM is very sensitive to synchronization mismatches. Moreover OFDM may not be applicable for fragment spectrum or dynamic resource allocation from the high out-of-band emission.

To reduce OOB emission and support relaxed synchronization requirements, filter-bank multi-carrier with offset quadrature amplitude modulation (FBMC-OQAM) and universal filtered multi-carrier (UFMC) systems are widely studied. Both FBMC-OQAM and UFMC systems provide higher spectral efficiency and more reliable communication than OFDM systems by adopting different waveform filters. Although FBMC-OQAM and UFMC systems are more robust to synchronization mismatch than that of OFDM, synchronization is one of the critical issues.

Timing synchronization estimate the timing offset and the starting index of the received signals. Timing synchronization failure introduces inter-symbol interference (ISI) due to multipath fading channels. Carrier frequency offset (CFO) estimation deals with the compensation of carrier frequency mismatch between the TX and RX pair. Also CFO estimation deals with the Doppler spread from the mobility of users. Without CFO estimation, severe performance degradation is introduced by inter-carrier interference (ICI).

This dissertation includes the analysis, design, and implementation of timing and carrier frequency synchronization schemes for FBMC-OQAM and UFMC systems. We have developed data-aid synchronization methods for both systems. First, we have analyzed the correlation properties in FBMC-OQAM to develop the signal detection, coarse TO, and CFO estimation algorithms. The proposed synchronization algorithms for FBMC-OQAM systems can be applicable not only burst/continuous transmission but also multi-

input multi-output(MIMO) with space time-block coding(STBC). Second, we have developed the criterion for filter parameter selection for UFMC systems to avoid loss of useful properties of training symbols in UFMC systems. Then, we proposed the normalization schemes to simplify setting a threshold for signal detection. Moreover, integer and fractional CFO estimation along with cell ID detection schemes are proposed for UFMC systems. We also present the coarse TO and CFO estimation for asynchronous multi-user uplink (UL) transmissions. As the received signal at the base station is the summation of all multi-user signals, we have proposed the sub-band-based filtering to avoid multi-user interference (MUI) from asynchronous transmission among multi-users. Moreover, we have proposed new filtering schemes to support multi-service communications (MSC). In MSC systems, multi-user and multi-service signals with different system specification are combined in same radio frequency. We have developed the service-based filtering schemes to reduce inter-service interference (IsvI) and multi-service interference (MsvI). Finally, we have demonstrated the over-the-air transmission to evaluate the performance of proposed asynchronous multi-user UL transmissions and MSC systems.

CHAPTER 1
INTRODUCTION

1.1 Motivation

Multi-carrier transmission techniques are widely adopted in wireless communication systems. Many applications such as long term evolution (LTE) [1] and IEEE 802.11n [2] are employed orthogonal frequency division multiplexing (OFDM) as the multi-carrier modulation technique. Compared to the single-carrier transmission scheme, OFDM systems are robust to frequency selective channels from sub-carrier-based resource allocation. Moreover, OFDM can support flexible resource allocation to multi-users. Finally, fast Fourier transform (FFT)-based modulation and one-tap frequency domain equalization (FDE) reduce the system complexity compared to single-carrier systems.

However, OFDM systems require strict timing and frequency synchronization at the receiver. Without proper synchronization, timing offset (TO) introduces inter-symbol interference (ISI) and carrier frequency offset (CFO) leads to inter-carrier interference (ICI) which lead to severe performance degradation [3]. Another drawback of OFDM systems is the high out-of-band (OOB) power emission of OFDM signals [4]. Therefore, OFDM systems may not be suitable in fragment spectrum or dynamic resource allocation for the multi-service communication systems [5].

Recently the 5th generation of cellular network communication systems (5G) are widely researched to support Internet of Things (IoT), enhanced mobile broadband (eMBB) [6], ultra-reliable and low latency communications (URLLC), and massive machine type communications (mMTC) which require higher data-rate, higher spectral efficiency, or lower latency than the current 4G communication systems [7, 8, 9]. Although 5G eMBB service will adopt the OFDM-based systems similar to current 4G LTE systems, new waveforms

has been considered and researched to support low OOB emission and relaxed synchronization requirements for various services in 5G. As an alternative to OFDM, filter-bank multi-carrier with offset quadrature amplitude modulation (FBMC-OQAM) systems have been investigated in [10, 11]. The FBMC-OQAM systems adopt time and frequency well localized pulse shaping filters. As results, the FBMC-OQAM systems offer following major merits: 1) the FIR filter is implemented with the Nyquist criterion [12] and it leads to overlap the continuous symbol waveform; 2) the out-of-band power radiation has dramatically suppressed which can reduce interference among users in adjacent channels; 3) well designed filters are robust to channel with time and frequency spreading [13, 11]; 4) the FBMC-OQAM systems do not require a cyclic prefix (CP) and provide the maximum spectral efficiency [14, 15]; and 5) finally, FBMC-OQAM is more robust to synchronization mismatch compared to OFDM systems[16, 17].

To support mMTC or URLLC services, universal filtered multi-carrier (UFMC) [18, 19, 20] have been widely researched [21, 22] as an alternative to OFDM and FBMC-OQAM. Unlike to FBMC-OQAM systems, UFMC systems employ sub-band, group of subcarriers,-based pulse-shaped filters to provide a flexible solution for satisfying the requirements for mMTC or URLLC in 5G networks. By using sub-band-based filtering, the UFMC systems offer the following major merits: 1) the out-of-band power emission has severely depressed which can reduce interference among adjacent services [19]; 2) sub-band-based resource allocation allows multi-service communication systems [5] or asynchronous multi-user transmission [23]; and 3 finally, short burst communication can be supported from shorter filter response. Similar to the OFDM systems, inverse-FFT and FFT-based modulation scheme can reduce the hardware implementation complexity. Moreover, UFMC systems support multiple input multiple output (MIMO) with space time block coding (STBC) [24] with minor modification of conventional algorithms in OFDM systems. Finally, UFMC systems are robust to timing and carrier frequency mismatches compared to OFDM systems [18, 25, 26].

Although both FBMC-OQAM and UFMC systems are more robust to synchronization mismatch than OFDM systems, the performance of FBMC-OQAM and UFMC systems are degraded without proper synchronization. Specifically, timing and carrier frequency mismatches still lead to ICI and ISI in both systems. ICI is usually generated by the CFO from the local oscillator mismatch or Doppler shift from the mobility of users at the receiver. Moreover, ICI, the loss of orthogonality between sub-carriers in frequency domain, leads to severe performance degradation. ISI is generated by the TO from the propagation delay. Specifically, a demodulation window contains not only desired signals but also adjacent signals in time domain which degrade the performance of system. Therefore, synchronization is a fundamental step in wireless communications

To compensate the effects of TO and CFO, synchronization in multi-carrier systems is a two-fold process : coarse and fine [27]. Coarse timing synchronization estimate the starting samples of the multi-carrier symbol or radio-frame, while fine timing estimation increase the accuracy of estimated TO. Similarly, coarse CFO synchronization estimates a large CFO while the residual CFO is estimated by fine frequency synchronization.

1.2 Thesis Contributions

Motivated by the performance degradation of multi-carrier systems from the synchronization impairments, we have developed and evaluated timing and frequency synchronization techniques for FBMC-OQAM and UFMC systems. The key contributions of this thesis are given as follows:

1. Joint timing and frequency synchronization algorithms have been developed for FBMC-OQAM systems. The proposed timing estimation does not require a threshold or matched filter to detect the training signals. Moreover, the proposed synchronization algorithms is applicable for burst, continuous transmission, and MIMO transmission by using two uncorrelated and independent training sequences.

2. Joint timing and frequency synchronization algorithms have been developed for DL UFMC transmission along with cell ID detection. We present the criterion for selecting filter parameters. We show that auto-correlation-based timing synchronization is robust to the integer CFO. Moreover, we develop an weight function to increase the accuracy of integer CFO estimation.

3. Single resource block-based timing estimation for UFMC systems has been proposed to support multi-user asynchronous UL transmission.

4. Blind timing estimation for UFMC systems has been developed to support multi-service communication. Service-based filtering techniques are proposed to reduce interference from other services.

5. A hardware testbed has been implemented for demonstrating over-the-air transmission with UFMC systems to evaluate the proposed synchronization algorithms.

1.3 Outline

The rest of the dissertation is organized as follow.

Chapter 2 presents an introduction to FBMC-OQAM and UFMC system models and signal description. Moreover, a literature survey of the existing synchronization algorithms are presented.

Chapter 3 presents a joint timing and frequency offsets estimation for FBMC-OQAM systems using two uncorrelated training signals. The details of training sequences design and algorithms are presented with the performance evaluation.

Chapter 4 provides cell search procedure, signal detection, and synchronization algorithms for UFMC systems in the presence of integer CFO.

Chapter 5 provides a receiver design with single resource block-based timing estimation with UFMC systems for dealing with asynchronous UL transmission.

Chapter 6 deals with asynchronous multi-user and multi-service communication with UFMC systems.

Chapter 7 concludes the dissertation with providing future research directions.

Notations. Column vectors are in lower case bold, $(\cdot)^T$ denotes the transpose, $\odot$ denotes the element-wise vector multiplication, $\triangleq$ stands for definition, $\angle$ denotes the arguments of the complex number, $(\cdot)^*$ denotes the conjugate, $\overleftarrow{(\cdot)}$ denotes the flip function, and $C\mathcal{N}(\cdot)$ represents the complex Gaussian distribution. $\lfloor \cdot \rfloor$ is the floor operation,

CHAPTER 2

BACKGROUND AND LITERATURE SURVEY

The objective of the dissertation is developing synchronization algorithms for FBMC-OQAM and UFMC systems. Due to the different system structures, system model and signal descriptions are presented. Moreover, the background of two multi-carrier systems and literature survey of existing synchronization schemes are presented in this chapter.

2.1 Filter-bank multi-carrier offset QAM transmission

In this section, we provide the system model of FBMC-OQAM transmissions along with the literature survey of conventional synchronization techniques.

2.1.1 FBMC-OQAM system model

Consider the discrete-time equivalent baseband model of the PPN-based FBMC-OQAM system with N sub-carriers [12]. We denote the nth sub-carrier at the ith frequency domain symbol as $A_{i,n} \in \mathbb{C}$. The in-phase and quadrature components of $A_{i,n}$ are represented as $A_{i,n}^I$ and $A_{i,n}^Q$. As shown in Fig. 2.1, data symbols are staggered in time domain by half of symbol duration $NT_s/2$ at the transmitter, where $T_s \triangleq T/N$ is the sampling period and T is the symbol duration. Then the m_sth samples at the gth transmitted FBMC-OQAM block in time domain can be written as

$$s[gN + m_s] = s^I[gN + m_s] + js^Q[gN + m_s - N/2],$$
$$m_s \in \{0, 1, \cdots, N-1\}, \tag{2.1}$$

where

$$
\begin{aligned}
s^I[gN+m_s] &\triangleq s^I((gN+m_s)T_s) \\
&= \sum_{i=0}^{\infty}\sum_{n=0}^{N-1} A_{i,n}^I e^{j\frac{2\pi(gN+m_s)T_s}{T}n}\beta_n \\
&\quad \times h((gN+m_s)T_s - iNT_s) \\
&= \sum_{i=0}^{\infty}\sum_{n=0}^{N-1} A_{i,n}^I e^{j\frac{2\pi m_s}{N}n}\beta_n h_{g-i}(m_sT_s), \\
s^Q[gN+m_s] &= \sum_{i=0}^{\infty}\sum_{n=0}^{N-1} A_{i,n}^Q e^{j\frac{2\pi m_s}{N}n}\beta_n h_{g-i}(m_sT_s),
\end{aligned} \tag{2.2}
$$

where $\beta_n = e^{jn\pi/2}$ is the phase rotation to the nth sub-carrier, $h_{g-i}(m_sT_s) \triangleq h\left((m_s+(g-i)N)T_s\right)$ is the real-valued symmetric pulse shaping filter [12] in both time and frequency domains. By defining

$$
b_{i,m_s}^I = \sum_{n=0}^{N-1} A_{i,n}^I \beta_n e^{j\frac{2\pi m_s}{N}n}, \tag{2.3}
$$

which is the N-point inverse fast Fourier transform (IFFT) output of $A_{i,n}^I\beta^n$ with respect to n, then Eq. (2.3) can be rewritten as

$$
\mathbf{b}_i^I = \text{IFFT}\left[\mathbf{A}_i^I \odot \boldsymbol{\beta}\right], \tag{2.4}
$$

where IFFT$[\cdot]$ is the $N-$point IFFT function, $\mathbf{A}_i^I$ is the $N\times 1$ in-phase data symbol vector of $\mathbf{A}_i = \mathbf{A}_i^I + j\mathbf{A}_i^Q$, and $\boldsymbol{\beta}$ is the $N\times 1$ phase shift vector. Then, the gth transmitted FBMC-OQAM block with the inphase data symbol can be rewritten as

$$
\mathbf{s}_g^I \triangleq \sum_{i=0}^{\infty} \mathbf{b}_i^I \odot \mathbf{h}_{g-i}, \tag{2.5}
$$

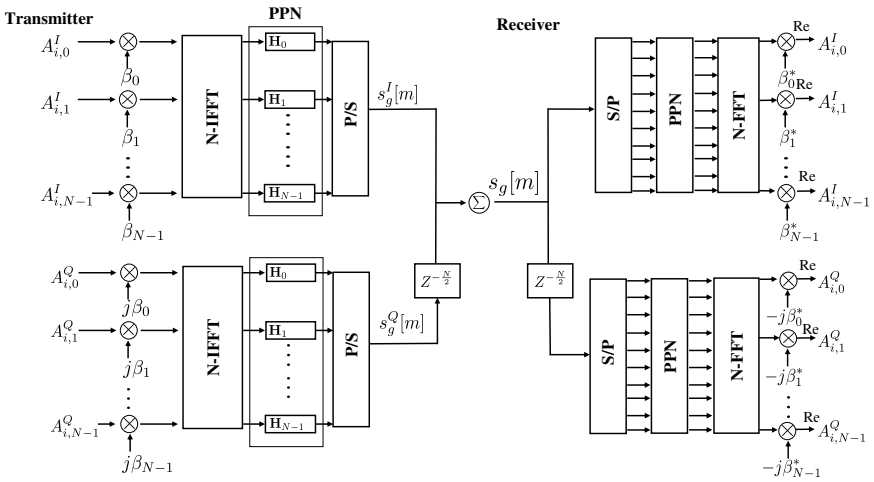

Figure 2.1: PPN-based FBMC-OQAM system model [12].

where $\mathbf{h}_{g-i}$ is a filter coefficient vector defined as

$$\begin{aligned}\mathbf{h}_{g-i} &= \left[h_{g-i,0}, \cdots, h_{g-i,N-1}\right]^T, \ \forall g-i \in \{0, \cdots, V-1\},\\ \mathbf{h}_{g-i} &= \mathbf{0}, \qquad\qquad \text{otherwise},\end{aligned} \tag{2.6}$$

$h_{g-i,m_s} = h_{g-i}(m_s T_s)$, and V is the overlapping factor. Eq. (2.5) shows that the gth transmitted FBMC-OQAM signal contains V adjacent overlapped signals with different filter coefficients. Finally, the gth transmitted PPN-based FBMC-OQAM block is written as

$$\begin{aligned}\mathbf{s}_g^I &= \mathbf{b}_g^I \odot \mathbf{h}_0 + \mathbf{b}_{g-1}^I \odot \mathbf{h}_1 + \cdots + \mathbf{b}_{g-(V-1)}^I \odot \mathbf{h}_{V-1},\\ \mathbf{s}_g^Q &= \mathbf{b}_g^Q \odot \mathbf{h}_0 + \mathbf{b}_{g-1}^Q \odot \mathbf{h}_1 + \cdots + \mathbf{b}_{g-(V-1)}^Q \odot \mathbf{h}_{V-1}.\end{aligned} \tag{2.7}$$

According to (2.1) to (2.7), the FBMC-OQAM signals have intrinsic interferences generated by overlapping the input symbols. By using phase rotation, adjacent sub-carriers interference can be avoided. Although FBMC-OQAM is more robust to timing and frequency mismatches than OFDM, CFO and timing offset TO still lead to ICI and inter-symbol interference ISI and thus degrade the performance of FBMC-OQAM systems [16, 17].

2.1.2 Literature Review of Synchronization algorithms for FBMC-OQAM systems

As similar as OFDM systems, various timing and frequency synchronization algorithms including non-data-aided blind methods [28, 29, 30] and data-aided methods [31, 32] for the FBMC-OQAM systems have been developed. In [28], the second-order cyclostationarity-based blind synchronization algorithm has been proposed. However, the slow convergence of the algorithm in [28] is not suitable for practical implementation. To cope with the drawbacks of [28], non-data-aided CFO estimation has been proposed based on the maximum-likelihood (ML) estimator by exploiting the properties of non-conjugate and conjugate cyclostationarity from the received FBMC-OQAM signal over multi-path channels [29]. However, the ML estimator leads to huge computational complexity. To reduce computational complexity, the closed form of the least-squares (LS) CFO estimator has been proposed in [30]. However, those estimators in [29, 30] require more FBMC-OQAM symbols to provide reliable performance than the data-aided methods.

In [31], data-aided joint TO and CFO estimation algorithms with robust acquisition properties in dispersive channels based on the LS approach have been proposed. Specifically, the cross correlation-based metric by exploiting the periodic training burst (named as TR2) in [31] provides a sharp peak. However, algorithms in [31] require the knowledge of the periodic training burst and relatively large number of training symbols to compensate the overlapped symbols interference. To reduce the number of training symbols while providing a sharp peak, matched filter-based timing metric has been proposed by exploiting the conjugate symmetric property in [32]. Since the matched filter can detect training blocks and estimate TO, the threshold can be avoid. Similar to [31, 33], correlation-based CFO estimation with identical signal blocks has been employed in [32]. However, the matched filter-based timing metric requires a long observation window. Moreover, the computational complexity is increasing because of another correlation function from the matched filter. Recently, the new synchronization sequences have been proposed to provide a sharp peak in [34]. The modified constant amplitude zero autocorrelation (CAZAC) signals are

generated by compensating overlapped symbol interferences by using the feedback from prior data symbols. Unlike [32], the timing metric in [34] is robust to continuous transmission mode. But the CFO estimation has not been considered in [34]. Moreover, prior symbols are always required to generate training sequences. Therefore, the data rate is reduced for the burst transmission mode. Finally, the identical training block based algorithms in [31, 32] are not applicable in the multi-input multi-output (MIMO) FBMC systems with a space-time block coding (STBC) [35].

The proposed solution is the training-based synchronization method. By using two uncorrelated training sequences, we observe the unique correlation patterns at the receiver. We also modify the conjugate-symmetric (CS) property by considering null sub-carriers. Unlike to the timing metric in [32], the proposed detection algorithm does not require a long observation window and the matched filter. Therefore, the proposed schemes reduce the computational complexity. Different from the conventional correlation-based CFO estimators with identical signal blocks in [31, 32, 33], the proposed ratio-based CFO estimator does not require identical training sequences. Therefore, the proposed schemes are robust to interference from the overlapped FBMC symbols and applicable for the MIMO-FBMC systems with STBC. Moreover, a single auto-correlation-based architecture can be used for signal detection, and thus require less resource for TO and CFO estimation. Finally, the proposed schemes are generally applicable to both burst and continuous transmission. The details can be found in Chapter 3 and [36].

2.2 Universal Filtered Multi-Carrier Transmission

As mentioned in Section. 1.1, FBMC-OQAM may not be applicable for short packet transmission in mMTC or URLLC from longer filter responses. In this section, we provide the system model of UFMC transmissions with synchronization techniques. UFMC systems have sub-band-based waveform filter which reduce OoB level but supporting similar spectral efficiency as OFDM.

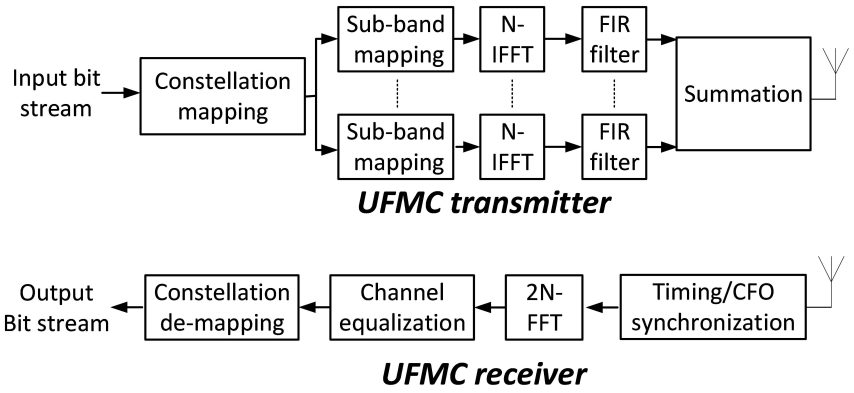

Figure 2.2: UFMC transmitter and receiver system blocks

2.2.1 UFMC system model

Lets consider the discrete-time equivalent baseband of the UFMC systems with N sub-carriers. We denote the kth sub-carrier at the bth sub-band symbol as $X_b[k] \in \mathbb{C}$. As shown in Fig. 2.2, the UFMC transmitted signals are consisted of the summation of multiple sub-bands output as

$$s[n] = \sum_{b=0}^{B} s_b[n], \quad 0 \leq n \leq N + L - 1, \tag{2.8}$$

where $s[n]$ is the transmitted UFMC signals, $s_b[n]$ is the bth sub-band output, N is the size of IFFT, and L is the waveform filter length. Moreover, the bth sub-band output is written as

$$s_b[n] = \sum_{l=0}^{L-1} f_b[l] x_b[n-l], \quad 0 \leq n \leq N + L - 1. \tag{2.9}$$

In (2.9), the bth sub-band output $s_b[n]$ is generated by the linear convolution of the bth filter responses $f_b[l]$ and the IFFT output of bth sub-band $x_b[n]$ defined as

$$x_b[n] = \frac{1}{N} \sum_{k \in RB_b} X_b[k] e^{j\frac{2\pi k}{N} n}, \quad 0 \leq n \leq N-1,$$
$$f_b[l] = f[l] e^{j\frac{2\pi l}{N} c_b}, \quad 0 \leq l \leq L-1, \tag{2.10}$$

where RB_b is the allocated sub-carrier indices at the bth sub-band, c_b is the center sub-carrier index of the bth sub-band, and $f[l]$ is the lth component of the reference filter responses. Then, the bth sub-band filter responses are easily calculated by combining the discrete phase shifter with c_b. Specifically, the output in (2.8) is equivalent to the OFDM modulated signal without the CP insertion when the filter length $L = 1$ and $f[0] = 1$. Finally, discrete received UFMC signals in the presence of TO and CFO are represented as

$$r[n] = e^{j\frac{2\pi}{N} fn} \sum_{m=0}^{M-1} h[m] s[n-d-m] + w[n], \tag{2.11}$$

where $h[m] \in \mathbb{C}, 0 \leq m \leq M-1$ is the CIR with M taps and $w[n]$ is the complex additive white Gaussian noise (AWGN) with zero mean and band-limited power spectral density $N_0/2$. Although the UFMC systems support relaxed synchronization requirements [18, 25, 26], synchronization mismatches still introduce ICI and ISI.

2.2.2 Literature Review of Synchronization algorithms for UFMC systems

In the literature, numerous synchronization algorithms for the OFDM systems with data-aid methods have been researched. As one type of data-aided methods, auto-correlation-based synchronization schemes use the properties of identical or symmetric signal blocks of training symbols [37, 38, 39, 40]. Since auto-correlation-based timing synchronization is robust to large CFO, it can be applicable for downlink (DL) initial synchronization with unknown CFO. In contrast, cross-correlation-based TO estimation schemes with time-domain gener-

ated local templates at the receiver provide better timing accuracy in the absence of integer CFO [41, 42]. As a DL synchronization and cell search procedures in LTE, Zadoff-Chu (ZC) sequences-based [43] timing synchronization has been employed [1]. However, the performance of cross-correlation-based TO estimation severely degrades by the affect of integer CFO. To avoid the performance degradation of TO estimate, joint fine timing and CFO estimation with using two ZC sequences has been proposed in [44]. By exploring the properties of cross-correlation with ZC sequences, synchronization schemes in [44] estimate joint TO and CFO with combining channel impulse response (CIR) estimation in [42]. However, the conventional synchronization methods in OFDM systems may not work or may require a modification for the UFMC systems because of the sub-band waveform filters. Due to the lack of the CP in the UFMC systems, the CP-based TO or CFO estimation cannot be applicable. In contrast to the large volume of synchronization algorithms for the OFDM systems, there are lack of synchronization solutions for the UFMC systems. Recently, time-domain generated preamble with PN sequences have been proposed [45] to avoid sub-band filter effects. By combining auto-correlation and cross-correlation of received preamble, the performance of TO estimation is improved. However, the CFO estimation and channel estimation have not been considered.

As an initial synchronization, we proposed joint timing and frequency synchronization schemes including cell search procedures in the presence of large CFO with single training symbol for UFMC systems. We also presented the criterion for choosing the filter length to keep the useful properties of the training symbol. By using the proposed normalization techniques for signal detection, we can avoid estimating noise variance and channel estimation for setting the threshold. Moreover, we propose an integer CFO estimation with using frequency domain correlation by adding a proposed weight function. The weight function is generated by analyzing the relationship between frequency shift from the integer CFO and resource allocation with null-sub carriers. Finally our proposed coarse synchronization schemes provide signal detection, the estimation of coarse TO, integer and fractional CFO

estimation, channel frequency response estimation, and cell ID detection. The details can be found in Chapter 4.

2.3 Uplink Transmission with UFMC systems

As part of the dissertation, signal detection and timing estimation for UFMC with frequency-division multiple access (FDMA) UL transmission has been studied. This section presents system model to support asynchronous multi-user and multi-service UL transmission.

2.3.1 Asynchronous Multi-user Uplink Transmission

In 4G LTE system with single-carrier FDMA (SC-FDMA) UL transmission requires synchronous transmissions among multi-users (MU) with timing advanced scheme (TAS) [46]. However, the synchronous UL transmissions introduce additional signaling overhead. Therefore, it may not be suitable for the mMTC scenario. In the literature, numerous research efforts are carried out on UFMC to support advanced applications for 5G communication systems. Coordinated multi-point with UFMC (UFMC-CoMP) schemes for multiple BSs and UEs have been proposed in the presence of multiple CFOs [18]. Moreover, the new UFMC system structures with reducing system complexity to support MU-machine type communications have been proposed [47]. However, both systems in [18, 47] require synchronous uplink transmissions. To support asynchronous uplink transmissions, interleave division multiple access (IDMA) with UFMC, including elementary signal estimator (ESE) for asynchronous multi-user detection, has been proposed [48]. However, UFMC-IDMA cannot be compatible with current 4G systems from different multiple access schemes.

To support asynchronous uplink transmission, we propose a new UFMC-FDMA receiver structure which can support the coexistence of 4G systems. Since UFMC transmitter contains multiple sub-band filters, we adopt equivalent filters at the receiver to separate different sub-band signals from asynchronous users. Moreover, we suggest the coarse timing

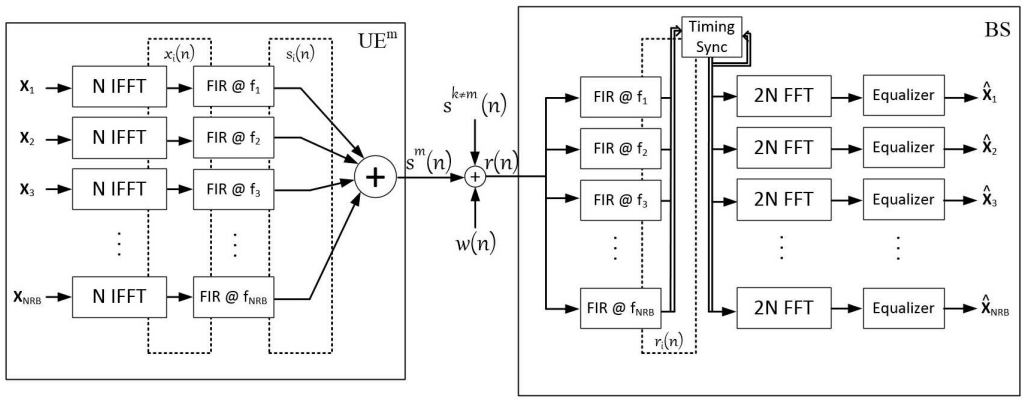

Figure 2.3: Proposed UFMC transceiver system block diagram.

synchronization algorithm to detect target user signals. Specifically, we added a sub-band filters at the receiver with single resource block-based signal detection and timing estimation illustrated in Fig. 2.2. To support asynchronous uplink transmissions, we adopt equivalent filters at the transmitter to the receiver as illustrated in Fig. 2.3. Therefore, filtered received signal corresponding to the ith sub-band from (2.11) can be written as following

$$r_i(n) = \sum_{l=0}^{L-1} f_i(l) r(n-l). \tag{2.12}$$

If users are assigned at the single sub-band, (2.12) can be re-written as

$$r_i(n) = \sum_{l=0}^{L-1} f_i(l) s_i^{m_i}(n-l-\tau_{m_i}) + \omega_i(n), \tag{2.13}$$

where m_i is the corresponding user, who is allocated at the ith sub-band and $\omega_i(n) = \sum_{l=0}^{L-1} f_i(l) w(n-l)$ is the filtered noise.

To detect target user signals, we proposed a single resource block-based with using 7-lengths of ZC sequences and auto-correlation-based signal detection. The details can be found in Chapter 5 and [23].

2.3.2 Multi-Service Communication systems with UFMC-FDMA

As mentioned in Chapter 1.1, 5G services are categorized into three main scenarios: eMBB, mMTC, and URLLC. The easiest way to support three different services is designing a separate standalone radio systems. However, the standalone radio systems will be complex and lead to inefficient network usage. By utilizing scalable numerology for diverse spectrum bands and scalable bandwidth [49], unified radio frame structures, divide the system bandwidth for different type of services with several bandwidth to meet the requirements for all types of services, have been considered [50, 51] as multi-service communication (MSC) systems. The flexible resource allocation for multi-service system can be supported by combining some techniques for cognitive radio networks [52, 53]. However, combining different frame-structures of services in single frequency band will introduce inter-service interference (IsvI) and destroy the orthogonality of multi-carrier systems. By assuming pre-compensation of CFO at UE devices and semi-synchronous MU transmission in each services, the received signal is written as

$$r(n) = \sum_{k=1}^{N_K} r_{sv_k}(n - \tau_{sv_k}) + w(n), \tag{2.14}$$

where N_K is total number of services, $r_{sv_k}(n) = \sum_{m=0}^{M_k-1} s^m_{sv_k}(n-\tau_{m,sv_k})$ is the received MU received signal in the kth service, and $\tau_{sv_k} = \frac{1}{M_k}\sum_{m=0}^{M_k-1} \tau_{m,sv_k}$ is the average timing offsets of MU signals in the kth service. Although the received MU signals in each services are satisfying the synchronous transmission, combining different services leads to not only the IsvI but also multi-service interference (MsvI). As a part of the dissertation, we present the all-in-one receiver structure with proposed filtering techniques to support the MSC systems by reducing the MsvI and IsvI. The details are presented in chapter 6 and experiment results with proposed systems can be found in [54].

CHAPTER 3
GENERALIZED SYNCHRONIZATION ALGORITHMS FOR FBMC-OQAM SYSTEMS

This chapter presents a joint timing and frequency synchronization algorithms for FBMC-OQAM systems. The proposed algorithms is data-aided with using two uncorrelated binary sequences with null sub-carriers in frequency domain. The design of training sequences for FBMC-OQAM is first discussed followed by analyzing the statistics of auto-correlation output of the received training symbol at the receiver. Based on the relationship between two training sequences, the correlation output provides unique patterns. The analysis shows that distance between two consecutive peaks is same as symbol duration when two training sequences are independent and uncorrelated. Based on the analysis, we develop the signal detection and TO estimation without setting a threshold or matched filter. Moreover, the fractional CFO is estimated by deriving the ratio of two consecutive correlation gain. This chapter concludes with simulation results with comparing the performance of existing synchronization algorithms in the literature.

3.1 Synchronization Sequence Design for FBMC-OQAM

The CS property has been applied for synchronization sequence, e.g., the real input case is investigated in [55]. Also the approximate CS property in FBMC-OQAM has been investigated with in-phase input data symbols [32, 56]. We extend the CS property to the RCS by employing a binary training sequence with null sub-carriers, where the training sequence is denoted as $A_{i,n}^{TR} \in \{\pm 1\}$. Then, to apply the RCS property, the even indices of

sub-carriers are only carrying training sequences as

$$\begin{aligned} A_{i,n}^{TR,I} &= 0, \qquad \text{if } n \text{ is odd,} \\ A_{i,n}^{TR,I} &\in \{\pm 1\}, \quad \text{if } n \text{ is even,} \\ A_{i,n}^{TR,Q} &= 0, \qquad \forall n. \end{aligned} \tag{3.1}$$

Therefore, the phase shift vector $\boldsymbol{\beta}$ in (2.4) does not convert $A_{i,n}^{I}$ into the complex symbols as

$$\begin{aligned} A_{i,n}^{TR,I}\beta_n &= 0, \qquad \text{if } n \text{ is odd,} \\ A_{i,n}^{TR,I}\beta_n &\in \{\pm 1\}, \quad \text{if } n \text{ is even.} \end{aligned} \tag{3.2}$$

Then, the IFFT output $\mathbf{b}_i^I$ in (2.4) holds not only the CS property but also the repetition property. Specifically, the IFFT output $\mathbf{b}_i^I$ satisfying (3.1) shows the following properties (c.f. [57]):

$$\begin{aligned} b_{i,m_s}^{TR,I} &= b_{i,\frac{N}{2}-m_s}^{TR,I^*}, \quad m_s \neq 0,\ \frac{N}{4}, \\ b_{i,m_s}^{TR,I} &= b_{i,\frac{N}{2}+m_s}^{TR,I}, \quad m_s \in \{0, \cdots, \frac{N}{2}-1\}. \end{aligned} \tag{3.3}$$

The proposed training sequences can be mapped at the beginning of a radio frame (e.g., IEEE 802.11n [2]), for the burst transmission as

$$\mathbf{A}_0^{TR}, \mathbf{A}_1^{TR}, \mathbf{A}_2, \cdots, \mathbf{A}_{N_f-1}, \tag{3.4}$$

while mapped between data symbols (e.g., long term evolution (LTE) [1]) for the continuous transmission as

$$\mathbf{A}_0, \cdots, \mathbf{A}_{i-1}, \mathbf{A}_i^{TR}, \mathbf{A}_{i+1}^{TR}, \mathbf{A}_{i+2}, \cdots, \mathbf{A}_{N_f-1}, \tag{3.5}$$

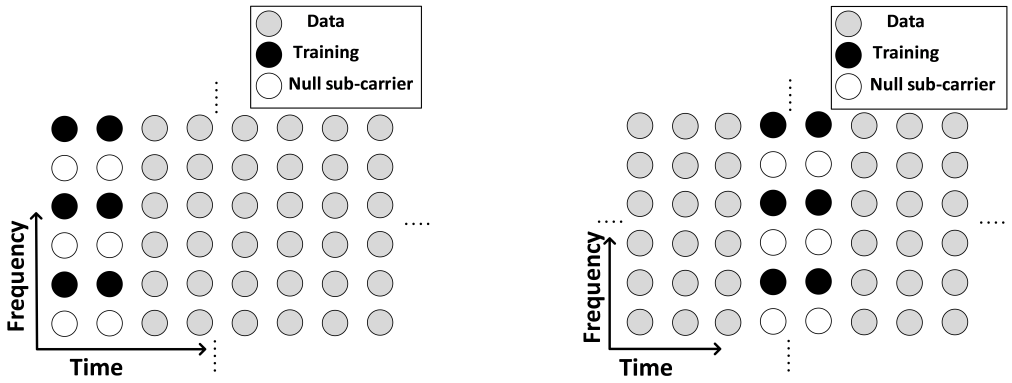

(a) Burst transmission mode.

(b) Continuous transmission mode.

Figure 3.1: Generalized frame structure with proposed training sequences. Training sequences are used for both synchronization and channel estimation.

where $\mathbf{A}_i^{TR} = \left[A_{i,0}^{TR}, 0, A_{i,2}^{TR}, 0, \cdots, 0, A_{i,N-2}^{TR}, 0\right]$ is the ith $N \times 1$ real training symbol vector and N_f is the total number of symbols including training and data symbols in each radio frame. Finally, the proposed training sequences can be generally adopted for both burst and continuous transmission as illustrated in Fig. 3.1.

3.1.1 Statistics of Correlation output

In the presence of TO and CFO, the mth sample of the received signal can be written as

$$y[m] = e^{j\frac{2\pi}{N}fm} \sum_{p=1}^{P} c_p s[m - d - \tau_p] + w[m], \quad m \in [-\infty, \infty] \tag{3.6}$$

where c_p is the base-band channel impulse response with P taps, τ_p is the pth multipath delay spread, d is the TO from the first multipath delay, f is the normalized CFO, and $w[m]$ is a complex additive white Gaussian noise (AWGN) with zero-mean and band-limited power spectral density σ_w^2. We assume flat fading channels, d is an integer value, $\tau_1 = 0$, and $P = 1$, to simplify the following derivation. Then, the correlation output at the kth

observation window is written as

$$r_k[l] = \frac{1}{N}\sum_{m=0}^{N-1} y[kN+l+m]y[(k+2)N+l-m]. \tag{3.7}$$

By applying (3.6) into (3.7), we obtain

$$\begin{aligned} r_k[l] = & \frac{1}{N}\sum_{m=0}^{N-1} c_0^2 e^{j\frac{2\pi}{N}f((2k+2)N+l)} \\ & \times s\left[kN+m+l-d\right] s\left[(k+2)N+l-n-d\right] \\ & + \frac{1}{N}\sum_{m=0}^{N-1} c_0 e^{j\frac{2\pi}{N}f(kN+m+l)} \\ & \times s\left[kN+m+l-d\right] w\left[(k+2)N+l-m\right] \\ & + \frac{1}{N}\sum_{m=0}^{N-1} c_0 e^{j\frac{2\pi}{N}f((k+2)N+l-m)} \\ & \times s\left[(k+2)N+l-m-d\right] w\left[kN+m+l\right] \\ & + \frac{1}{N}\sum_{n=0}^{N-1} w\left[kN+m+l\right] w\left[(k+2)N+l-m\right]. \end{aligned} \tag{3.8}$$

As each noise and signal samples are assumed to be uncorrelated, a strong correlation gain can be expected with a certain correlation lag l. We investigate the relationship between correlation outputs in (3.7) and training sequences in (3.1). Based on different training sequence patterns mapped to the burst transmission mode at Fig. 3.1 (a), we observe the following properties with the different overlapping factors V:

Proposition 1. *If two consecutive training sequences* $A_{0,n}^{TR}, A_{1,n}^{TR},\ n \in [0, N-1]$ *are identical with* $V \in \{2, 4\}$*, the highest peak will be located at* $\left|r_{\frac{V-2}{2}}[\frac{N}{2}]\right|$.

Proof. See Appendix A. □

Proposition 2. *If two consecutive training sequences* $A_{0,n}^{TR}, A_{1,n}^{TR},\ n \in [0, N-1]$ *are uncorrelated and independent with* $V \in \{2, 4\}$*, unique peak patterns are repeated where the highest peaks in each pattern are located at* $\left|r_{\frac{(V-2)}{2}}[0]\right|$ *and* $\left|r_{\frac{V}{2}}[0]\right|$.

Proof. See Appendix B. □

As shown in Fig. 4.3, multiple peaks are observed at specific correlation indices with different correlation gains based on training sequence patterns. According to (3.3), the training sequence with null sub-carriers generates the repeated conjugated symmetric signal in time-domain. Therefore, the distance between adjacent peak indices from the correlation output in (3.7) is $\frac{N}{4}$ and we denote the set of indices providing the correlation gains for $\forall k$ as the "peak region" given as

$$\mathcal{R}_{peak} = l \in \{d, \frac{N}{4} + d, \frac{N}{2} + d, \frac{3N}{4} + d\}. \tag{3.9}$$

Finally, the correlation outputs in (3.8) are approximately distributed as follows:

$$\begin{aligned} r_k[l] &\sim C\mathcal{N}\left(0, \frac{c_0^2 E_{k,l}\sigma_w^2}{N} + \frac{c_0^2 \breve{E}_{(k+2),l}\sigma_w^2}{N} + \frac{\sigma_w^4}{2N}\right) \\ &= C\mathcal{N}\left(0, \sigma_1^2\right), \quad l \notin \mathcal{R}_{peak}, \\ r_k[l] &\sim C\mathcal{N}\left(c_0^2\mu_{k,l}, \frac{c_0^2 E_{k,l}\sigma_w^2}{N} + \frac{c_0^2 \breve{E}_{(k+2),l}\sigma_w^2}{N} + \frac{\sigma_w^4}{2N}\right) \\ &= C\mathcal{N}\left(c_0^2\mu_{k,l}, \sigma_2^2\right), \quad l \in \mathcal{R}_{peak}, \end{aligned} \tag{3.10}$$

where

$$\begin{aligned} \mu_{k,l} &= \frac{1}{N}\sum_{m=0}^{N-1} |s\left[kN + m + l - d\right] s\left[(k+2)N + l - m - d\right]|, \\ E_{k,l} &= \frac{1}{N}\sum_{m=0}^{N-1} |s\left[kN + m + l - d\right]|^2, \\ \breve{E}_{k+2,l} &= \frac{1}{N}\sum_{m=0}^{N-1} |s\left[(k+2)N + l - m - d\right]|^2, \end{aligned} \tag{3.11}$$

and σ_w^2 is the noise variance.

We assume that $E_{k,l} = \breve{E}_{k+2,l} \simeq E_s$, where $E_s = \frac{1}{VN}\sum_{m=0}^{VN-1} |s\left[m + l - d\right]|^2$ is the

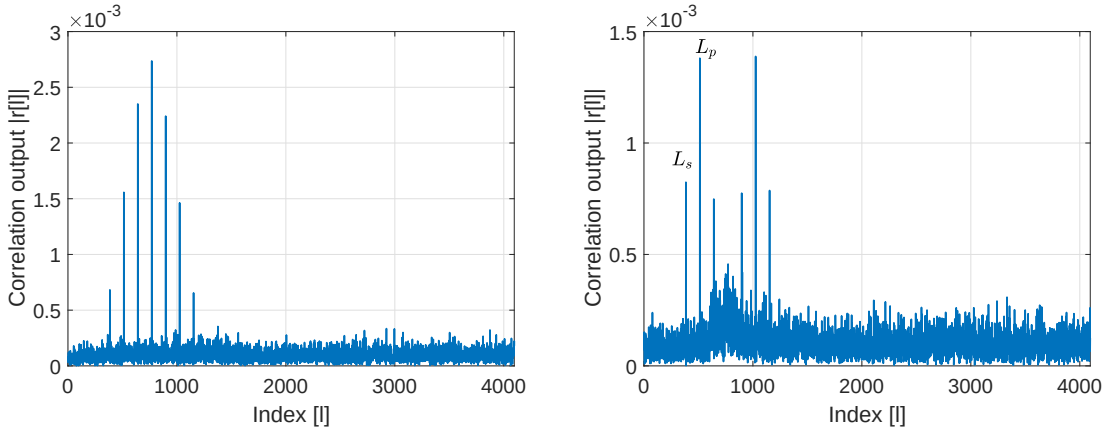

(a) Training sequences with Proposition. 1.

(b) Training sequences with Proposition. 2.

Figure 3.2: The visualization of the correlation output with serializing $r_k[l]$ in (3.7) for SNR $= 0$ dB, $N = 512$, and $V = 4$. In the absence of TO, multiple peaks are observed: (a) The highest peaks are located at $\frac{3N}{4}$, N, $\frac{5N}{4}$, $\frac{6N}{4}$, $\frac{7N}{4}$, $2N$, $\frac{9N}{4}$ (b) 6 correlation peaks are located at $\frac{3N}{4}$, N, $\frac{5N}{4}$, $\frac{7N}{4}$, $2N$, $\frac{9N}{4}$.

average energy of transmitted training blocks, and then $\sigma_1^2 = \sigma_2^2 = \sigma_r^2$ in (3.10).

3.2 Proposed joint Timing and Carrier Frequency Offsets estimation

As illustrated in Fig. 4.3, the multiple correlation peaks with different correlation gains are observed with two training sequences satisfying both Proposition 1 and Proposition 2. Therefore, a threshold should be well designed to detect proper peak while avoiding high probability of false alarm. Otherwise, the alternative algorithms should be considered to detect a training block and estimate the TO. Since the energy gap between desired peak and side peaks are small in Fig. 4.3. (a), it is difficult to design the fine threshold. To avoid setting the fine threshold to detect the desired peak, the highest peak location can be detected by finding the maximum value of the correlation outputs during one radio frame duration. To reduce the probability of false alarm, a matched-filter is considered. Then the highest peak is detected when the matched-filter output is maximum. However, it requires the long observation window and increases the hardware complexity to avoid setting the threshold.

In this section, we derive the statistical detection model to detect training block generated based on Proposition 2. Then we propose a new algorithm to detect the training block and estimate the TO and the CFO. The proposed algorithm does not require the prior knowledge about the noise variance or channel state information.

3.2.1 Neyman-Pearson Detection

As we derived the statistics of correlation output samples $|r_k[l]|$ in (3.10), the threshold can be designed based on the statistical model. To detect the desired peak which is L_p against the side peak L_s in Fig. 4.3 (b), we adopt the Neyman-Pearson (NP) test [58]. The NP test evaluates the absolute values of each correlation output samples $|r_k[l]|$ for the decision-making with the following hypotheses defined as

Null Hypothesis $(\mathcal{H}_0)$:

$$|r_k[l]| \sim \frac{x}{\sigma_r^2} \exp\left(-\frac{x^2}{2\sigma_r^2}\right), \tag{3.12}$$

Alternative Hypothesis 1 $(\mathcal{H}_1)$:

$$|r_k[l]| \sim \frac{x}{\sigma_r^2} \exp\left(-\frac{x^2 + c_0^2\mu_{1,d}^2}{2\sigma_r^2}\right) I_0\left(\frac{x c_0^2 \mu_{1,d}}{\sigma_r^2}\right), \tag{3.13}$$

Alternative Hypothesis 2 $(\mathcal{H}_2)$:

$$|r_k[l]| \sim \frac{x}{\sigma_r^2} \exp\left(-\frac{x^2 + c_0^2\mu_{0,\frac{3}{4}+d}^2}{2\sigma_r^2}\right) I_0\left(\frac{x c_0^2 \mu_{0,\frac{3}{4}+d}}{\sigma_r^2}\right), \tag{3.14}$$

where I_0 is the modified Bessel function of the first kind with order zero. We employ the fact that the absolute value of a complex Gaussian random variable with zero mean has Rayleigh distribution while Rician distribution with non-zero mean. Moreover, we use two different alternative hypotheses $(\mathcal{H}_1, \mathcal{H}_2)$ instead of the null hypothesis. The Alternative Hypothesis 1 is derived based on the statistics with an index L_p while an index L_s is used

for the Alternative Hypothesis 2. Therefore, the NP test with given hypotheses is written as follows

$$\frac{\Pr\left[r[l]|\mathcal{H}_1\right]}{\Pr\left[r[l]|\mathcal{H}_2\right]} = \exp\left(c_0^2 \frac{-\mu_{1,d}^2 + \mu_{0,\frac{3}{4}+d}^2}{2\sigma_r^2}\right) \times \frac{I_0\left(c_0^2 \frac{|r_k[l]|\mu_{1,d}}{\sigma_r^2}\right)}{I_0\left(c_0^2 \frac{|r_k[l]|\mu_{0,\frac{3}{4}+d}}{\sigma_r^2}\right)} > \gamma, \tag{3.15}$$

where γ is the threshold. Eq. (3.15) can be simplified to

$$\begin{aligned}
&\sqrt{\frac{\mu_{0,\frac{3}{4}+d}}{\mu_{1,d}}} \exp\left(c_0^2 \frac{-\mu_{1,d}^2 + \mu_{0,\frac{3}{4}+d}^2}{2\sigma_r^2} + c_0^2 \frac{\mu_{1,d} - \mu_{0,\frac{3}{4}+d}}{\sigma_r^2} |r_k[l]|\right) \\
&\simeq \sqrt{\frac{2}{3}} \exp\left(-\frac{5c_0^2 \mu_{0,\frac{3}{4}+d}^2}{8\sigma_r^2} + \frac{c_0^2 \mu_{0,\frac{3}{4}+d}}{2\sigma_r^2} |r_k[l]|\right) > \gamma \\
&\simeq -\frac{5c_0^2 \mu_{0,\frac{3}{4}+d}^2}{8\sigma_r^2} + \frac{c_0^2 \mu_{0,\frac{3}{4}+d}}{2\sigma_r^2} |r_k[l]| > \gamma',
\end{aligned} \tag{3.16}$$

where we assume that $\mu_{1,d} = \frac{3}{2}\mu_{0,\frac{3}{4}+d}$, by using the asymptotic expansions of the modified Bessel function (c.f. [59, p. 377])

$$I_0(z) \sim \frac{\exp(z)}{\sqrt{2\pi z}} \left(1 + \frac{1}{8z} + \cdots\right), \tag{3.17}$$

and γ' is the threshold satisfying a given probability of false alarm P_{FA}

$$\Pr\left[-\frac{5c_0^2 \mu_{0,\frac{3}{4}+d}^2}{8\sigma_r^2} + \frac{c_0^2 \mu_{0,\frac{3}{4}+d}}{2\sigma_r^2} |r_k[l]| < \gamma'\right] = P_{FA}. \tag{3.18}$$

Finally, the corresponding index is chosen as the estimated TO $\hat{d}$ as

$$\hat{d} = kN + l, \quad \text{if } |r_k[l]| > \left(\frac{2\sigma_r^2}{c_0^2 \mu_{0,\frac{3}{4}+d}} \gamma' + \frac{8}{5} c_0^2 \mu_{0,\frac{3}{4}+d}\right). \tag{3.19}$$

In (3.19), the test statistic compares the energy of correlation output samples with the

threshold. To obtain the TO estimate, we search for the first l crossing the threshold. However, the condition in (3.19) can be satisfied early from the side peak L_s due to the repetition property of FBMC-OQAM. Moreover, the test still requires the knowledge of noise variance and channel coefficient to calculate σ_r^2. However, those parameters may not be available and may be time-varying.

3.2.2 Timing offset estimation

In the previous section, we derived a statistical model to detect training blocks by using the NP test. However, the NP test requires the knowledge of noise variance which is unknown and a correlation gain which is easily affected by fading channels. To avoid setting the threshold, a matched filter has been considered to detect the training block and estimate the TO. As shown in Fig. 4.3 (a), the matched filter similar to the one in [32] is used to detect training blocks and estimate TO with the following impulse response

$$\begin{aligned} f_{MF}[n] \triangleq\ & \alpha_1 \delta\left[n - \frac{3}{4}N\right] + \alpha_2 \delta\left[n - \frac{1}{2}N\right] \\ & + \alpha_3 \delta\left[n - \frac{1}{4}N\right] + \delta\left[n\right] \\ & + \alpha_3 \delta\left[n + \frac{1}{4}N\right] + \alpha_2 \delta\left[n + \frac{1}{2}N\right] \\ & + \alpha_1 \delta\left[n + \frac{3}{4}N\right], \end{aligned} \tag{3.20}$$

where $\delta[n]$ is the Kronecker delta function and α_1, α_2, and α_3 are scaling factors. Then the TO can be estimated as

$$\hat{d} = MF_{max} - \frac{3}{4}N, \tag{3.21}$$

where MF_{max} is the corresponding index which maximizes the matched filter output. However, the matched filter-based detection requires a long observation window and increases the computational complexity. Therefore, we propose a new joint TO and CFO estimation

algorithm.

In our approach, we do not require any knowledge of noise variance, fading channel coefficients, or correlation gain. Moreover, neither the threshold nor the matched filter is required. As illustrated in Fig. 4.3 (b), training sequences with Proposition. 2 provide repeated peak patterns. By analyzing the unique patterns from the correlation output at Fig. 4.3 (b), we propose a new algorithm to detect training blocks and estimate the TO. Specifically, we define an N correlation output vector at the kth correlation window in (3.7) as

$$\mathbf{R}_k = [r_k[0], r_k[1], \cdots, r_k[N-2], r_k[N-1]]^T, \tag{3.22}$$

where $\mathbf{R}_k$ is updated after collecting N correlation output samples in (3.7). Once we obtain $\mathbf{R}_k$, the index of the maximum value T_k is easily obtained as

$$[T_k,\ r_k[T_k]] = \underset{\forall m \in [0,N-1]}{\operatorname{argmax}} \{r_k[m]\}, \tag{3.23}$$

where $T_k \in \{0, \cdots, N-1\}$. As we proved in Proposition 2, we observed peaks at $r_1[0]$ and $r_2[0]$ when $d = 0$. Therefore, the training blocks are detected when two consecutive peak indices of T_k and T_{k+1} are the same. Based on our observation, we propose a new TO estimator by comparing the indices of the maximum value from current and previous correlation windows as

$$\begin{aligned} [T_{k-1}, r_{k-1}[T_{k-1}]] &= \underset{\forall m \in [0,N-1]}{\operatorname{argmax}} \{r_{k-1}[m]\}, \\ [T_k, r_k[T_k]] &= \underset{\forall m \in [0,N-1]}{\operatorname{argmax}} \{r_k[m]\}. \end{aligned} \tag{3.24}$$

Finally, the estimated TO can be obtained as

$$\hat{d} = (k-1)N + T_{k-1}, \quad \text{if } T_k = T_{k-1}. \tag{3.25}$$

Table 3.1: Proposed Joint TO and CFO estimation

Algorithm 1 : Joint TO and CFO estimation algorithm

Data : Correlation output N vector $\mathbf{R}_k$

Result : Timing offset $\hat{d}$, Carrier frequency offset $\hat{f}$

Initialization $k = 0$;

$[T_k,\ r_k[T_k]] = \text{argmax}\{\mathbf{R}_k\}$;

if $T_k == T_{k-1}$ **then**

  $\hat{d} = (k-1)N + T_{k-1}$;

  $\hat{f} = \frac{1}{4\pi}\angle\left(\frac{r_k[T_k]}{r_{k-1}[T_{k-1}]}\right)$;

else

  Failed synchronization;

end

$k = k + 1$;

3.2.3 Carrier frequency offset estimation

As a CFO estimation requires the knowledge of the symbol boundaries, the TO estimate is used for the CFO estimation. We can use correlation-based CFO estimation schemes similar to proposed in [31, 32, 33] when the training sequences are satisfying Proposition 1. Then, the CFO is estimated as

$$\Lambda_{cr} = \sum_{m=0}^{N-1} y\left[m + \hat{d} + N\right] y^*\left[m + \hat{d} + 2N\right],$$
$$\hat{f}_{cr} = \frac{1}{2\pi}\angle\Lambda_{cr}. \tag{3.26}$$

The correlation-based CFO estimation is robust to the interference from multi-path fading channels. However, the performance of correlation-based CFO estimation can be degraded over the continuous transmission mode where the training symbols are transmitted during data transmissions.

To reduce the interference from adjacent data symbol blocks, we propose the ratio-based CFO estimation algorithm with Proposition 2. Then, the correlation outputs in (3.7)

Table 3.2: Comparison of the computational complexity of timing offset estimation and the required number of training symbols or data symbols with overlapping factor V.

Method	Real multiplication	Required number of training symbols	Transmission mode
Proposed	$\mathcal{O}(N)$	2	Burst, Continuous
TR2 [31]	$\mathcal{O}(N^2)$	V + 2	Burst, Continuous
[32]	$\mathcal{O}(N^2)$	2	Burst
[34]	$\mathcal{O}(N)$	V (data symbols for feedback)	Continuous

with the corresponding peak indices in (3.24) are defined as

$$\begin{aligned} r_{k-1}[T_{k-1}] &\triangleq e^{j4\pi fk} r_{k-1,f0}[T_{k-1}], \\ r_{k}[T_{k}] &\triangleq e^{j4\pi f(k+1)} r_{k,f0}[T_{k}], \end{aligned} \tag{3.27}$$

where $r_{k-1,f0}[T_{k-1}]$ and $r_{k,f0}[T_k]$ are the correlation output with zero CFO. To estimate the CFO, we use the ratio between $r_{k-1}[T_{k-1}]$ and $r_k[T_k]$ as

$$\begin{aligned} \Lambda &\triangleq \frac{r_k[T_k]}{r_{k-1}[T_{k-1}]} = e^{j4\pi f} \frac{r_{k,f0}[T_k]}{r_{k-1,f0}[T_{k-1}]}, \\ \hat{f} &= \frac{1}{4\pi} \angle \Lambda. \end{aligned} \tag{3.28}$$

Finally, the proposed joint TO and CFO estimation algorithm is summarized in Table 3.1. We only use a single correlation function to estimate both TO and CFO which require less resource usage. Specifically, the computational complexity is $\mathcal{O}(N)$ same as [34]. However, we do not require the feedback from prior data transmissions. Moreover, the number of training symbols is 2 same as [32]. Finally, the proposed ratio-based CFO estimate can be utilized for both continuous and burst transmissions. The comparison of the existing schemes and the proposed algorithms is summarized in Table 3.2.

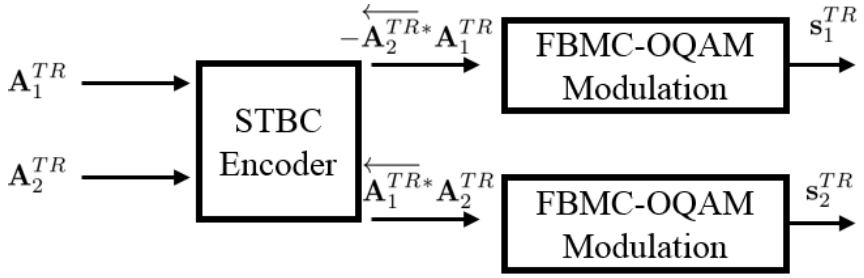

Figure 3.3: The MIMO-FBMC transmitter with a space-time block coding [35] with the proposed training sequence.

3.2.4 Synchronization for STBC-MIMO

So far, we introduced our TO and CFO estimators through Sections **??** and 4.2 by exploiting the properties of correlation with the proposed training sequences for SISO-FBMC systems. But the proposed joint TO and CFO estimation algorithms are also applicable at MIMO-FBMC systems. Consider the MIMO-FBMC system with a space-time block coding (STBC) [35] illustrated in Fig. 3.3. Because of the structure of the STBC, the conventional identical training symbol-based synchronization methods (e.g., [32, 31, 33]) are not applicable. However, the proposed synchronization algorithms with Proposition 2 are still applicable with an STBC encoder. Specifically, $\mathbf{A}_1^{TR}$ and $\mathbf{A}_2^{TR}$ in Fig. 3.3 are identical training sequences for two different antennas. Then, two training-block sequences are obtained for the two antennas as

$$\begin{aligned}\mathbf{Input}_1 &= \left[\mathbf{A}_1^{TR}, -\overleftarrow{\mathbf{A}_2^{TR*}}\right] \\ \mathbf{Input}_2 &= \left[\mathbf{A}_2^{TR}, \quad \overleftarrow{\mathbf{A}_1^{TR*}}\right].\end{aligned} \tag{3.29}$$

As shown in (3.29), the STBC encoder with identical training sequences produces two uncorrelated training sequences which are satisfying Proposition 2. Therefore, the proposed joint TO and CFO algorithm in Table 3.1 is still applicable.

3.3 Simulation Results

In this section, we compare the performance of the proposed algorithms with some of the existing schemes in the literature through Monte Carlo simulations. The sampling frequency is $1/T_s = 7.68$ MHz and the number of sub-carriers is $N = 512$. The CFO for each iteration is generated randomly from $[-f_{\max}, f_{\max}]$, where $f_{\max} = 0.25$ is the normalized CFO by the sub-carrier spacing. The PHYDYAS filter [12] is adopted as the filter $h[n]$ with the overlapping factor $V = 4$. As an input of the OQAM, the number of $N_D = 15$ data symbols with $4-$QAM and $N_{TR} = 2$ training symbols with BPSK modulation are employed. For the continuous transmission mode, the training symbols are inserted at the 6th symbols while inserted at the beginning of the radio frame for the burst transmission mode. The channel is modeled as the Rayleigh fading with the extended vehicular A (EVA) channel model [60]. For the MIMO-FBMC simulation, 2×2 MIMO systems with the STBC are considered. Moreover, we assume that the input data streams of the STBC are uncorrelated and independent. Finally, the MIMO channels are modeled as flat fading channels.

3.3.1 Performance of the Training Block Detection

Fig. 3.4 shows a comparison of the simulated NP test and the proposed algorithm for the training block detection in (3.19). To derive the threshold $\gamma^{'}$ in (4.19) for different target P_{FA}, we employ the Gaussian approximation with given noise variance σ_w^2 and channel coefficient c_0^2. Then P_m for the NP test is calculated as $P_m = 1 - P_d + P_w$, where P_d is the probability of detection at the desired peak L_p and P_w is the probability of false detection from the side peak L_s in Fig. 4.3 (b). The results for the proposed scheme are measured based on (3.25). Specifically, the probability of miss P_m is calculated when $T_k = T_{k-1}$ is not satisfied. As shown in Fig. 3.4, the performances of the training block detection with the derived threshold are illustrated with different mark notations for different target

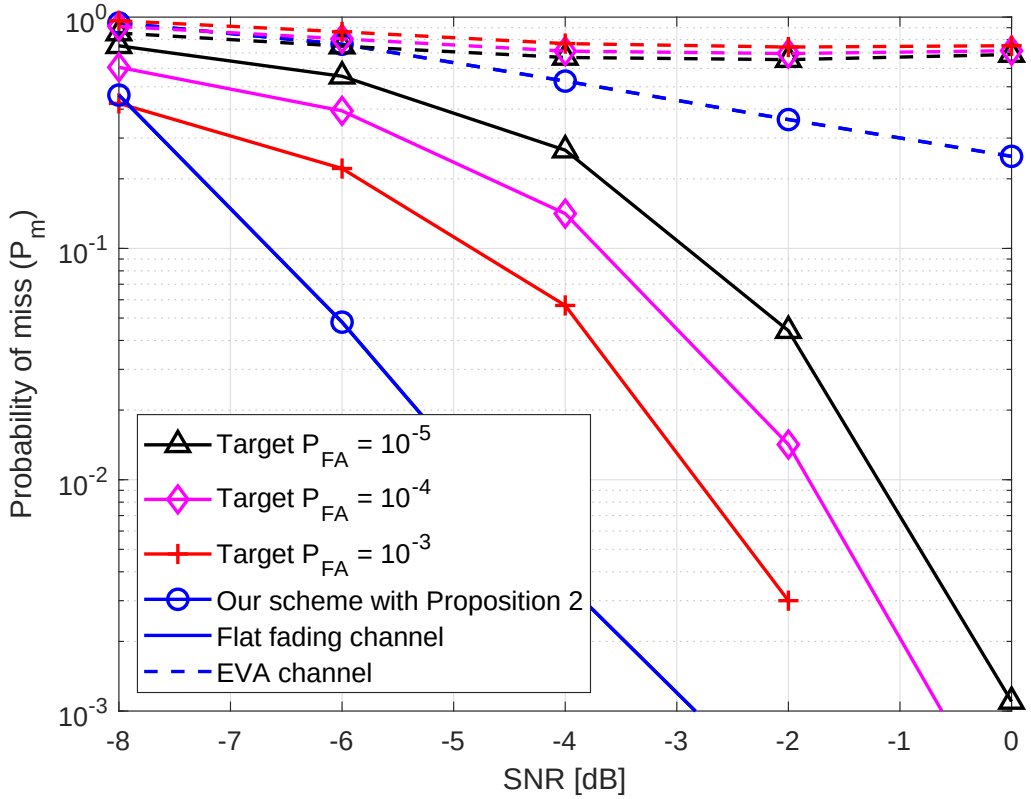

Figure 3.4: Comparison of the probability of miss P_m for the training block detection in (3.19) for different target P_{FA} and the proposed scheme in (3.25).

false alarm rates $P_{FA} = 10^{-3}, 10^{-4}, 10^{-5}$. Moreover, all the solid lines and the dash lines present flat fading channels and multipath fading channels with the EVA channel model, respectively. The proposed scheme shows better performance than the NP test with both flat fading channels and multipath fading channels. Since the threshold-based detection with the NP test can be triggered earlier because of the side peak L_s, the performance is easily affected by multi-path effects. Due to strict requirements in (3.25), the performance is degraded with using proposed method over multipath fading channels. However, the proposed scheme still shows better detection performance than the threshold-based detection.

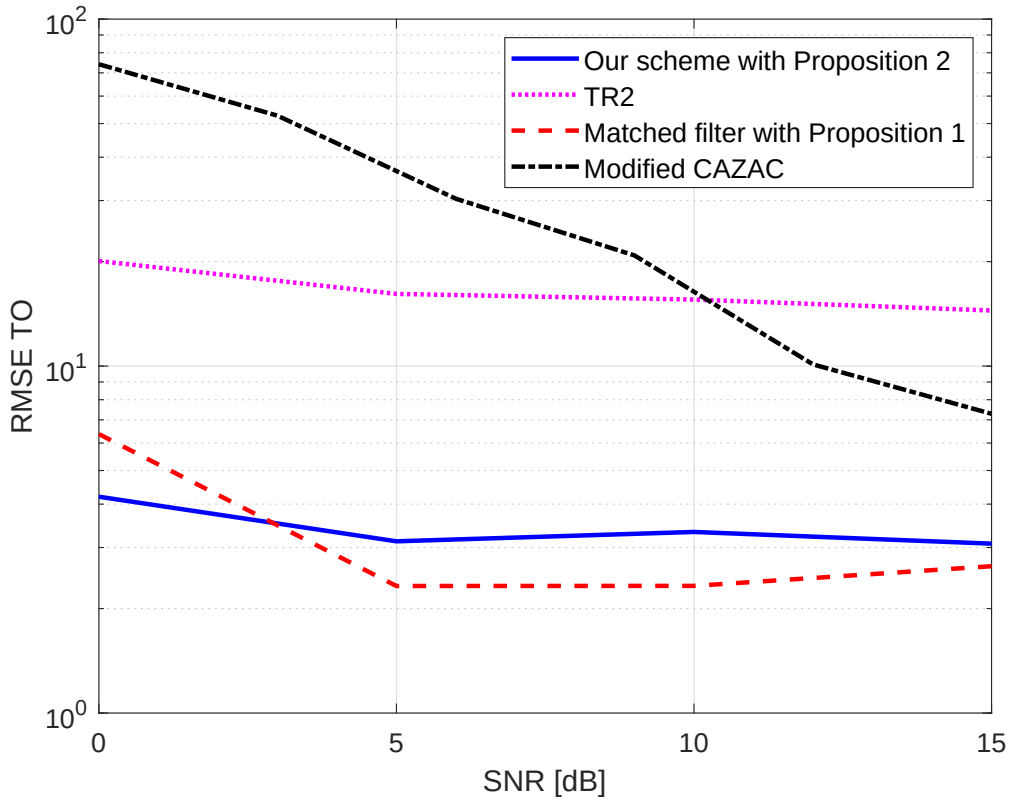

Figure 3.5: Performance of the TO estimation compared with the existing methods over EVA channels with SISO-FBMC.

3.3.2 Performance of the Timing Estimation

In Fig. 3.5, we illustrate the performance of timing estimation algorithms in terms of root mean squared error (RMSE) of TO estimation $\left(\sqrt{E\left[|d-\hat{d}|^2\right]}\right)$. Since both the proposed scheme in (3.25) and the existing schemes in [34, 32, 31] provide sharp peaks, we only illustrate the performance of TO estimation with multipath fading channels. Moreover, the 63-long C-sequences are employed for [34]. Finally, we assume the first path $d = 0$ in (3.6).

As shown in Fig. 3.5, the cross-correlation-based timing metrics in [34, 31] show worse performance than self-correlation-based timing metrics with conjugate symmetric properties. Since the self-correlation-based timing metrics in [32] employed the matched filter, the multi-path effects can be mitigated. Therefore, the RMSE of TO estimation

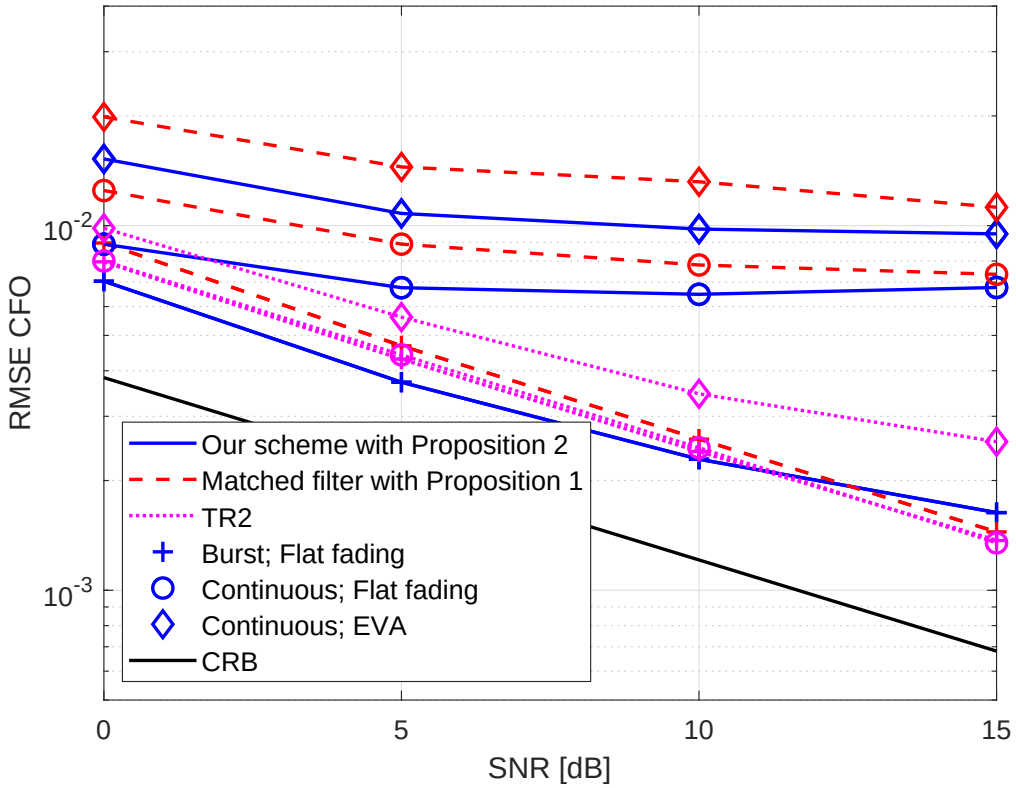

Figure 3.6: Performance of the CFO estimation over the burst and continuous transmission mode with SISO-FBMC.

in [32] shows the best performance. However, the proposed scheme also offers similar performance as [32] without using the matched filter.

3.3.3 Performance of the Carrier Frequency Offset Estimation

SISO-FBMC

In Fig. 3.6, we illustrate the performance of CFO estimation, in terms of RMSE of CFO estimation $\left(\sqrt{E\left[|f-\hat{f}|^2\right]}\right)$, with the proposed algorithm compared to existing schemes in [32, 31]. We also plot the Cramér-Rao bound (CRB) in [31] as the reference for the CFO estimation. We evaluate the CFO estimation with various scenarios: $1)$ the burst transmission mode over flat fading channels; $2)$ the continuous transmission mode over flat fading channels; $3)$ the continuous transmission mode over multipath fading channels.

As shown in Fig. 3.6, the RMSE of CFO estimations show similar performances with the burst transmission mode over flat fading channels. The proposed CFO estimation shows the better performance for lower SNR values while degrading the accuracy for higher SNRs.

In the case of continuous transmission, the training symbols are inserted between data symbols. Therefore, the training blocks over FBMC transmissions contain the interferences from adjacent data symbols. As we expected, the proposed scheme in (3.28) shows better performance than the correlation-based CFO estimation with identical blocks in [32]. The results indicate that the proposed scheme in (3.28) can reduce the interference from adjacent data symbols. Obviously, the performance of CFO estimation in [31] shows equivalent for both transmission mode because the large number of training symbols perform as guard signals.

Finally, the performance CFO estimation over multipath fading channels is illustrated. The estimate CFO in [31] shows the best estimation accuracy. But, the proposed ratio-based CFO estimation still provides better estimation performance than the correlation-based CFO estimations in [32].

MIMO-FBMC with STBC

In Fig.3.7, we evaluate the CFO estimation for MIMO-FBMC systems with STBC [35]. Since different timing metrics should be considered for MIMO-FBMC, we assumed the perfect timing synchronization for [32, 31]. As expected, the proposed scheme is less affected by STBC encoding because the STBC encoded training symbols can be considered as uncorrelated training symbols satisfying Proposition 2. However, the CFO estimation algorithms in [32, 31] show a severe performance degradation because of the STBC structure.

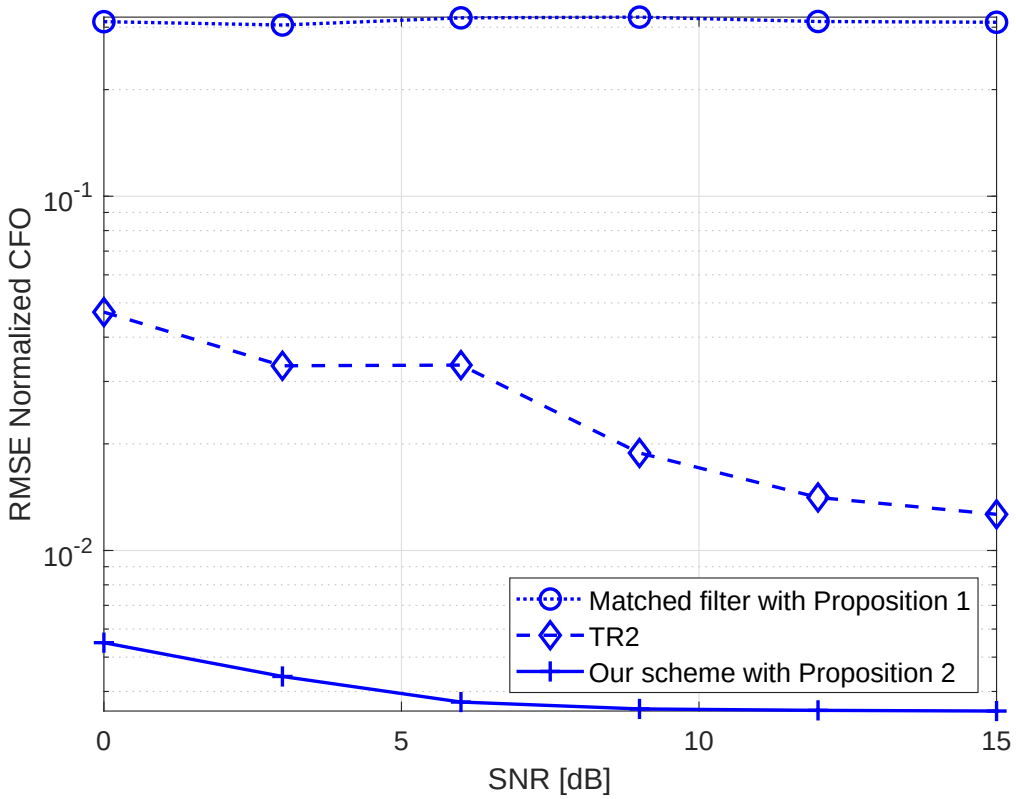

Figure 3.7: Performance of CFO estimation with 2×2 MIMO-FBMC with STBC over flat fading channels.

3.3.4 Performance of Bit Error-Rate

SISO-FBMC

Fig. 3.8 shows the comparison of bit error-rate (BER) performance with the proposed joint synchronization algorithm compared to the existing methods in [31, 32]. We employed a one-tap frequency domain zero-forcing (ZF) equalizer. Since the even indices of sub-carriers are carrying the training sequences while we inserted null signals at the odd indices, we use a frequency domain linear interpolation for the odd indices of sub-carriers for the channel estimation. We draw the perfect synchronization as the benchmark generated by the simulation with the flat fading channels. We also assume the perfect knowledge of the complex channel coefficient, the TO, and the CFO for the perfect synchronization. In

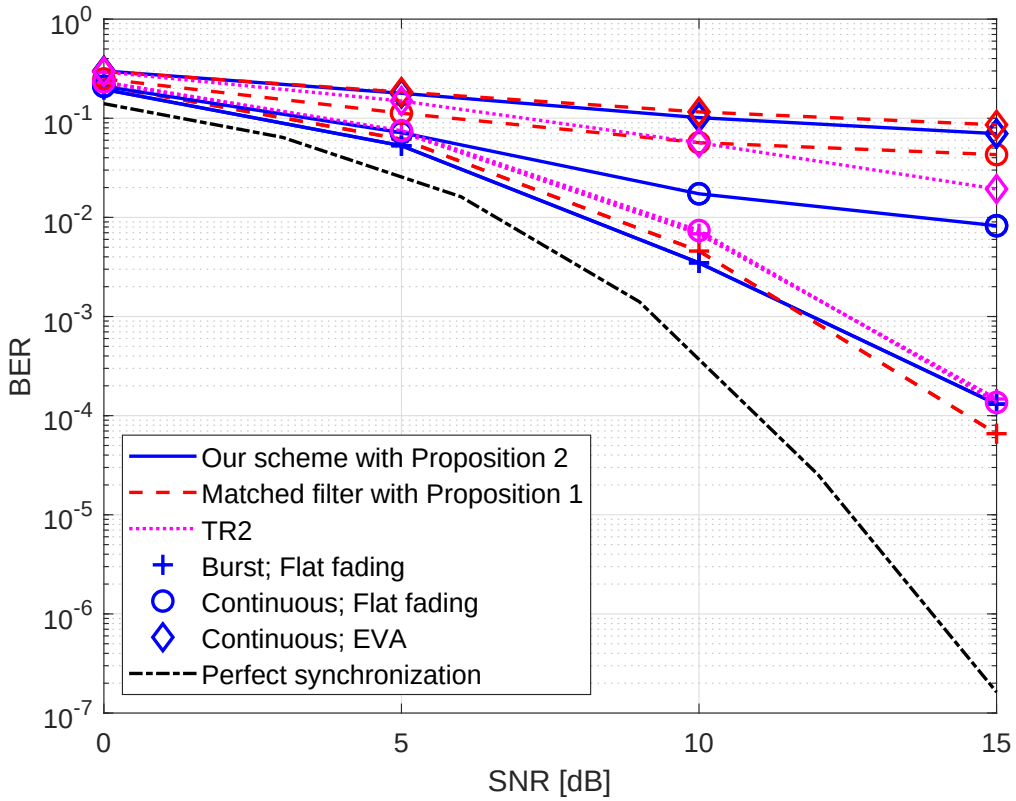

Figure 3.8: Comparison of bit error-rate performance with burst and continuous transmission mode with SISO-FBMC.

burst transmission mode, the BER performance is similar while the proposed scheme shows slight performance degradation for high SNRs because of less CFO estimation accuracy. As we expected, the proposed method shows better BER performance than [32] over continuous transmission mode while [31] shows equivalent performance as burst transmission mode. The BER performance with [31] shows the best performance with continuous transmission over EVA channel while the BER performance with the proposed method and [32] is similar performance. The results indicate that the FBMC systems are more sensitive to the CFO mismatch than the TO mismatch.

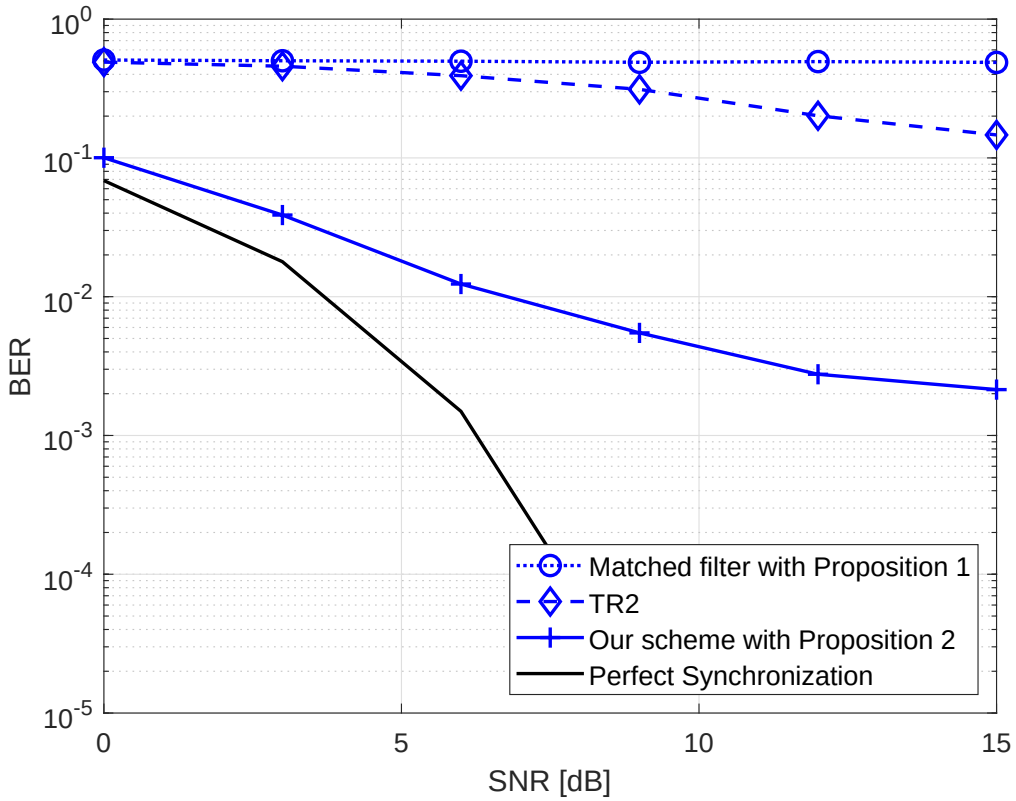

Figure 3.9: Comparison of bit error-rate performances with 2×2 MIMO-FBMC over flat fading channels.

MIMO-FBMC

Fig. 3.9 shows the BER performance for the 2×2 MIMO-FBMC system with the STBC encoding. We also illustrate the perfect synchronization as the benchmark for 2×2 MIMO-FBMC system with flat fading channels. Although we assume the perfect timing estimation for [31, 32], the severe performance degradation is observed because of the inaccuracy of the estimate CFO. The simulation shows that the proposed method shows the performance degradation compared to SISO-FBMC systems. However, the proposed method provides the best BER performance than the existing schemes.

CHAPTER 4

JOINT TIME AND FREQUENCY SYNCHRONIZATION FOR UFMC SYSTEMS

In this chapter, we present a joint timing and frequency synchronization in the presence of integer CFO along with cell ID detection procedure. The proposed algorithms is data-aided with using single binary sequences with null sub-carriers in frequency domain. The design of training sequences for UFMC systems is first discussed followed by analyzing the UFMC modulated symbol. Based on the analysis of the UFMC modulated training symbol, the criterion for selecting filter parameters to maintain the useful properties of training symbol from the specially designed training sequences. We develop the new normalization techniques to set a simple threshold. The statistical signal detection is also derived in this chapter for the reference. By analyzing the relationship between the effect of integer CFO and proposed training sequences, we develop the weight function to increase the accuracy of the integer CFO estimation. Simulation results have been illustrated with comparing existing synchronization methods in the literature.

4.1 Training Sequence Design

Let us assume that the training sequences are allocated in certain sub-carrier regions within a given bandwidth. Then, training sequences are divided into multiple sub-bands for the UFMC modulation. To make the training signals consisted of Q repeated signals in time-domain similar to preamble in [61], the training sequences allocated at the bth sub-band can be written as

$$X_b[k] = \begin{cases} \pm\mu, \ \mathrm{mod}\,(k, Q) = Q_0, \quad k \in RB_b \\ 0, \ \text{otherwise}, \end{cases} \tag{4.1}$$

where mod$(\cdot)$ is a modular function and $Q_0 \in [0, \cdots, Q-1]$ is the offset for sub-carrier index. Moreover, the binary sequences are weighted by μ to make an unit energy of training sequences as $E[\mathbf{X}_b] = 1$, where $\mathbf{X}_b = [X_b[0], X_b[1], \cdots, X_b[N_{sc}]]$ and N_{sc} is the number of sub-carriers in bth sub-band. Therefore, the allocated training sequences for the UFMC systems with $Q = 2$, and $Q_0 = 0$ can be written as

$$\mathbf{X}_{TR} = \left[\mathbf{X}_0^T, \mathbf{X}_1^T, \cdots, \mathbf{X}_B^T\right]^T, \tag{4.2}$$

where the bth sub-band contains training sequences with null sub-carriers as

$$\mathbf{X}_b = [X_b[RB_0 + bN_{sc}], 0, X_b[RB_0 + bN_{sc} + 2], \cdots, X_b[RB_0 + (b+1)N_{sc} - 2, 0]]^T, \tag{4.3}$$

where RB_0 is the reference even sub-carrier index at the 0th sub-band. To support cell ID search, training sequences should satisfy the following properties

$$\left.\begin{array}{l} \mathbf{X}_{TR,1}^T \mathbf{X}_{TR,2} \\ \mathbf{X}_{TR,1}^T \mathbf{X}_{TR,3} \\ \mathbf{X}_{TR,2}^T \mathbf{X}_{TR,3} \end{array}\right\} = 0, \tag{4.4}$$

where $\mathbf{X}_{TR,u}$ is training sequences for the uth cell ID. Then, the $N \times 1$ IFFT output of training symbols in (4.2) can be written as

$$\mathbf{x}_{TR,u} = \mathbf{F}^H \mathbf{X}_{TR,u}, \tag{4.5}$$

where $\mathbf{F}$ is the $N \times N$ Fourier transform matrix. It is well known that the IFFT output with real value input shows the conjugate symmetry properties. The training signals contain identical signal blocks. Finally, the output in (4.5) with (4.3) provide the repeated conjugate

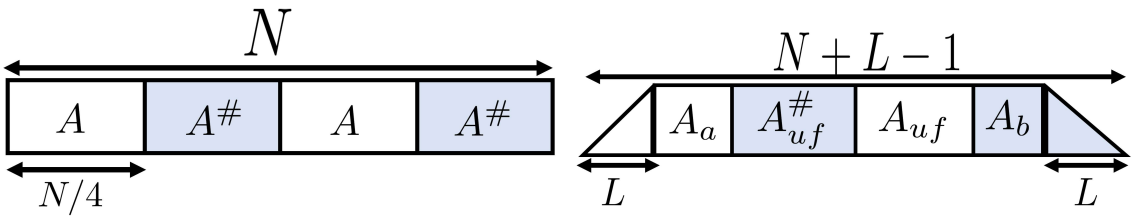

(a) OFDM modulated training symbol (b) UFMC modulated training symbol

Figure 4.1: Comparison of OFDM and UFMC modulated training signals in time domain with $Q = 2$ in (4.1). UFMC modulated training signals provide semi-conjugate and repeated properties.

symmetric as illustrated in Fig. 4.1 (a). Specifically, the properties of $\mathbf{x}_{TR}$ are written as

$$\begin{aligned} x_{TR,u}[n] &= x_{TR,u}\left[\frac{N}{2} - n\right]^*, \quad n \neq 0,\ \frac{N}{4}, \\ x_{TR,u}[n] &= x_{TR,u}\left[n + \frac{N}{2}\right], \quad n \in \{0, \cdots, \frac{N}{2} - 1\}, \end{aligned} \tag{4.6}$$

To detect training symbol and estimate timing offset, we employ the following auto-correlation-based metric

$$z[l] = \frac{2}{N} \sum_{n=0}^{N/2-1} r\left[l + n\right] r\left[N + l + 1 - n\right]. \tag{4.7}$$

However, the summation of multiple sub-bands signals which contain the linear convolution with sub-band filters in (2.8) can change the properties of training sequences in (4.6). Therefore, the correlation gain in (4.7) can be affected by the sub-band filter responses.

4.1.1 Sub-band Waveform Filter Design for Training Symbol

Due to the linear convolution with filter response and the IFFT output of the sub-band in (2.9), the first and the last L samples of training symbol are not identical to corresponding signal blocks. As illustrated in Fig. 4.1 (b), only partial signal blocks maintain the conjugate symmetry and repetition properties. By assuming uncorrelated and independent signals among multiple subbands, UFMC modulated training signals for the uth cell ID

provide identical samples as following

$$\begin{aligned}&\left[s_{TR}^{u}\left[L\right],\ s_{TR}^{u}\left[L+1\right],\ \cdots,\ s_{TR}^{u}\left[\frac{L+N-1}{2}-L\right]\right]^{T}\\&=\left[s_{TR}^{u}\left[L+\frac{N}{2}\right],\ s_{TR}^{u}\left[L+1+\frac{N}{2}\right],\ \cdots,\ s_{TR}^{u}\left[\frac{L+N-1}{2}-L+\frac{N}{2}\right]\right]^{T}\end{aligned}\tag{4.8}$$

where conjugate symmetric is partially maintained similar to

$$x_{TR}^{u}\left[\frac{L+N-1}{2}-n\right]=x_{TR}^{u}\left[\frac{L+N-1}{2}+n+1\right],\quad n\in[0,\frac{N}{4}].\tag{4.9}$$

However, the summation of each sub-band outputs can change the properties of training symbols in 4.6. Specifically, the UFMC modulation is consisted of the summation of multiple sub-band signals with different filter coefficients. Therefore, the properties in (4.8) and (4.9) may not be satisfied in certain cases. To avoid the lose of useful properties in training symbols, we suggest the criterion for choosing the filter length.

Proposition 3. *If the length of filter L is $\lfloor N/\kappa \rfloor$, where κ is a positive divisor of N_{sc} then the repeated conjugate symmetry properties of the UFMC modulated training symbols are partially maintained.*

Proof. See Appendix C. □

By combining Proposition 3 and training sequence in (4.3), good correlation properties are expected. The visualization of correlation outputs in (4.7) with different filter lengths are illustrated at Fig. 4.2. As we proved in Proposition. 3, the CSP properties are maintained when the length of the filter L satisfied the certain conditions as illustrated in Fig. 4.2. (a)-(d). As increasing the filter lengths, the side-lobe gain of correlation output is also increasing by losing the CSP properties. But we can still observe the good correlation properties. However, the correlation outputs provide the ambiguity of correlation gain as illustrated in Fig. 4.2. (e)-(h). Without satisfying Proposition. 3, the performance of

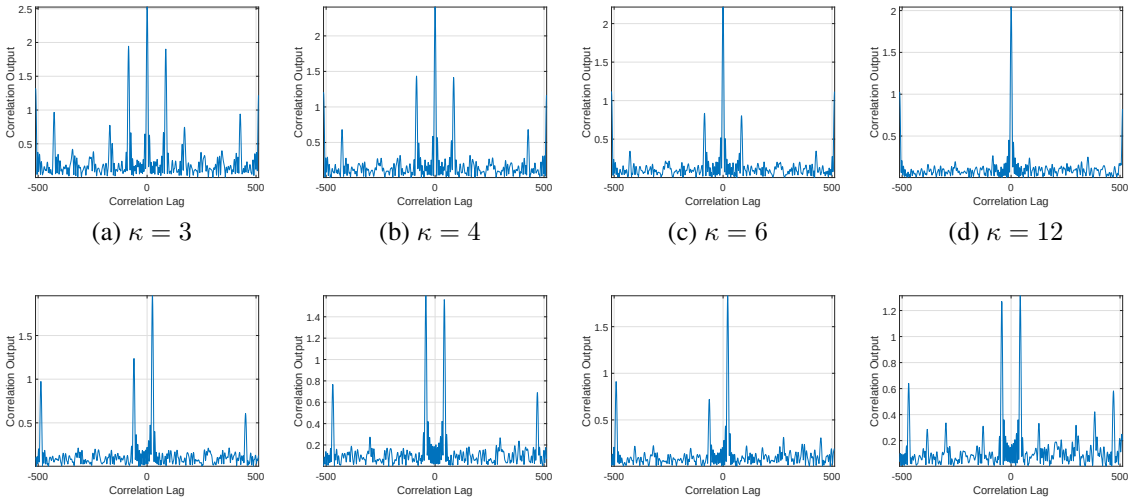

(a) $\kappa = 3$ (b) $\kappa = 4$ (c) $\kappa = 6$ (d) $\kappa = 12$

(e) $\kappa = 7$ (f) $\kappa = 8$ (g) $\kappa = 16$ (h) $\kappa = 24$

Figure 4.2: Comparison of correlation output in (4.7) with different κ to set the filter length L. Dolph-Chebyshev is adopted as a reference filter. Integer CFO and flat-fading channels are assumed with SNR = 10 dB.

TO estimate shows severe performance degradation. Therefore, sub-band waveform filters should be carefully designed to keep the useful properties of training signals.

4.1.2 Robustness of CFO effects

So far, we showed the relation between the length of filter and RCS properties. Since the auto-correlation output is independent to the cell ID, we drop the index u. To detect the

training signals, we derive the correlation output in (4.7) as

$$
\begin{aligned}
z[l] &= \frac{2}{N}\sum_{n=0}^{\frac{N}{2}-1} r\left[l+n\right] r\left[N+l+1-n\right], \\
&= \frac{2}{N}\left(\sum_{n=0}^{\frac{N}{2}-1}\left(e^{j\frac{2\pi}{N}f(l+n)}\sum_{m=0}^{M-1} h[m]s[n+l-m-d]+w[n+l]\right)\right. \\
&\times \left.\left(e^{j\frac{2\pi}{N}f(N+l+1-n)}\sum_{m^{'}=0}^{M^{'}-1} h[m^{'}]s[N+l+1-m^{'}-d-n]+w[N+l+1-n]\right)\right) \\
&= e^{j\frac{2\pi}{N}f(N+2l+1)}\frac{2}{N}\sum_{n=0}^{\frac{N}{2}-1}\left(\sum_{m=0}^{M-1}|h[m]|^2 s[n+l-m-d]s[N+l+1-n-d-m]\right)+\Psi[l]+\eta[l],
\end{aligned}
\tag{4.10}
$$

where

$$
\begin{aligned}
\Psi[l] &= e^{j\frac{2\pi}{N}f(N+2l+1)}\frac{2}{N}\sum_{n=0}^{\frac{N}{2}-1}\left(\sum_{m=0}^{M-1}\sum_{m^{'}=0,m^{'}\neq m}^{M^{'}-1} h[m]h[m^{'}]s[n+l-m-d]s[N+l+1-n-d-m^{'}]\right), \\
\eta[l] &= \frac{2}{N}\sum_{n=0}^{\frac{N}{2}-1}\left(e^{j\frac{2\pi}{N}f(l+n)}\sum_{m=0}^{M-1} h[m]s[n+l-m-d]w[N+l+1-n]\right) \\
&+ \frac{2}{N}\sum_{n=0}^{\frac{N}{2}-1}\left(e^{j\frac{2\pi}{N}f(N+l+1-n)}\sum_{m^{'}=0}^{M^{'}-1} h[m^{'}]s[N+l+1-m^{'}-d-n]w[n+l]\right) \\
&+ \frac{2}{N}\sum_{n=0}^{\frac{N}{2}-1} w[n+l]w[N+l+1-n].
\end{aligned}
\tag{4.11}
$$

As each channel tap $h[m] \sim C\mathcal{N}\left(0,\sigma_m^2\right)$ is assumed to be uncorrelated for different channel taps, the summation of the product of zero-mean uncorrelated channel gains where $m^{'} \neq m$ should be small. Therefore, we ignore $\Psi[l]$ in (4.10). Then, (4.11) is rewritten as

$$
z[l] \simeq e^{j\frac{2\pi}{N}f(N+2l+1)}\frac{2}{N}\sum_{n=0}^{\frac{N}{2}-1}\left(\sum_{m=0}^{M-1}|h[m]|^2 s[n+l-m-d]s[N+l+1-n-d-m]\right)+\eta[l].
\tag{4.12}
$$

According to (4.12), the CFO term $e^{j\frac{2\pi}{N}f(N+2l+1)}$ is independent to the index n. Specifically, both integer and fractional CFOs do not affect to the magnitude of the correlation outputs $|z[l]|$. Therefore, the auto-correlation-based method provides the robustness of the integer CFO and is applicable to the initial timing synchronization in the presence of unknown CFOs.

4.2 Detection and Coarse Timing Offset Estimation With Large CFO

In the previous section, we showed that the magnitude of auto-correlation outputs was not affected by the unknown CFOs. Therefore, we expect to observe the strong correlation gain in (4.12) when $l = d$ as

$$|z[d]| \approx E_{sh} \triangleq E\left[\left|\sum_{m=0}^{M-1} h[m]s[n-m]\right|^2\right], \tag{4.13}$$

where E_{sh} is received signal energy. To detect the training signals while avoiding false alarm from the noise samples, threshold should be well designed.

In this section, we derive the statistical signal detection by exploring the statistics of correlation outputs. Then, we propose the normalization schemes to simplify setting the threshold for training signal detection and the TO estimation.

4.2.1 Statistical Signal Detection

The correlation outputs in (4.12) are approximately distributed as follows:

$$\begin{aligned} z[l] &\sim C\mathcal{N}\left(E_{sh}, \frac{2E_{sh}\sigma_w^2}{N} + \frac{\sigma_w^4}{2N}\right), \quad \text{for } l = d, \\ z[l] &\sim C\mathcal{N}\left(0, \frac{2E_{sh}\sigma_w^2}{N} + \frac{\sigma_w^4}{2N}\right), \quad \text{for } l \neq d, \end{aligned} \tag{4.14}$$

where σ_w^2 is the variance of noise $w[n]$. Based on the distributions of correlation outputs in (4.14), we employ the Neyman-Pearson (NP) test [58] as a statistical signal detection. The

NP test evaluate the presence of training signals with using the magnitude of correlation outputs $|z[l]|$. Specifically, the NP test use following hypotheses for the decision-making as

Null Hypothesis ($\mathcal{H}_0$):

$$|z[l]| \sim \frac{x}{\sigma_\eta^2} \exp\left(-\frac{x^2}{2\sigma_\eta^2}\right), \tag{4.15}$$

Alternative Hypothesis ($\mathcal{H}_1$):

$$|z[l]| \sim \frac{x}{\sigma_\eta^2} \exp\left(-\frac{(x^2+\sigma_{sh}^2)}{2\sigma_\eta^2}\right) I_0\left(\frac{x\sigma_{sh}^2}{\sigma_\eta^2}\right), \tag{4.16}$$

where I_0 is the modified Bessel function of the first kind and zero order and $\sigma_\eta^2 = 2E_{sh}\sigma_w^2/N + \sigma_w^4/2N$. We assume that the absolute value of non-zero-mean complex Gaussian distributed random variables follow Rician distribution in $\mathcal{H}_1$ while $\mathcal{H}_0$ follows Rayleigh distribution. When signal-to-noise ratio (SNR) is high, the Rician distribution is well-approximated as Gaussian distribution. By assuming high SNR, the distribution of $\mathcal{H}_1$ is rewritten as

$$(|z[l]||\mathcal{H}_1) \sim \frac{1}{\sqrt{2\pi\sigma_\eta^2}} \exp\left(-\frac{(x-E_{sh})^2}{2\sigma_\eta^2}\right), \quad \text{when} \quad E_{sh} > \sigma_\eta^2, \tag{4.17}$$

Then likelihood ratio test (LRT) is written as

$$\begin{aligned} \frac{\Pr\left[|z[l]|\,|\mathcal{H}_1\right]}{\Pr\left[|r[l]|\,|\mathcal{H}_0\right]} &= \frac{\sigma_\eta}{\sqrt{2\pi}\,|z[l]|} \exp\left(\frac{2\,|z[l]|\,E_{sh} - E_{sh}^2}{2\sigma_\eta^2}\right) > \gamma \\ &\approx \left(\frac{2\,|z[l]|\,E_{sh} - E_{sh}^2}{2\sigma_\eta^2}\right) > \gamma' \\ |z[l]| &> \frac{2\gamma'\sigma_\eta^2 + E_{sh}^2}{2E_{sh}}, \end{aligned} \tag{4.18}$$

where the threshold γ' is calculated by using the NP criterion with a given probability of

false alarm P_{FA} under $\mathcal{H}_0$ as

$$\begin{aligned} &\Pr\left[|z[l]|\,|\mathcal{H}_0 > \gamma^{'}\right] = P_{FA}, \\ &\gamma^{'} = \sqrt{-2\ln(P_{FA})\sigma_{\eta}^2}. \end{aligned} \tag{4.19}$$

To detect training signal and estimate the TO, we search for the first l crossing the threshold with the NP criterion in (4.18). Then, the estimate TO is written as

$$\hat{d}_{NP} = l, \quad \text{when } |z[l]| > \frac{2\sigma_{\eta}^2\sqrt{-2\ln(P_{FA})\sigma_{\eta}^2} + E_{sh}^2}{2E_{sh}}. \tag{4.20}$$

However, the knowledge of noise variance and received signal power in (4.20) may be unknown and difficult to estimate at the receiver.

4.2.2 Proposed Signal Detection and Coarse Timing Estimation

To set a threshold without knowledge of the noise variance and received signal power, we propose new signal detection and TO estimation algorithms by using the normalization schemes. Let us assume that E_{sh} is known but σ_w^2 is unknown. Then, the normalized correlation outputs can be approximately calculated as

$$\begin{aligned} |\tilde{z}[l]| = \frac{|z[l]|}{E_{sh}} \approx \frac{E_{sh} + \sigma_{\eta}^2}{E_{sh}} \approx 1 \quad \text{for} \quad l = d, \\ |\tilde{z}[l]| = \frac{|z[l]|}{E_{sh}} \approx 0 \quad \text{for} \quad l \neq d, \end{aligned} \tag{4.21}$$

where we assume that $E_{sh} \gg \sigma_{\eta}^2$. Therefore, the threshold can be selected between $[0, 1]$. Since E_{sh} is varying depends on the channel condition, the channel information should be known at the receiver to avoid the power fluctuation of normalization. However, the prior knowledge of E_{sh} may be unavailable or time-varying at the receiver. Therefore, the normalization with using E_{sh} can be impractical in real scenario.

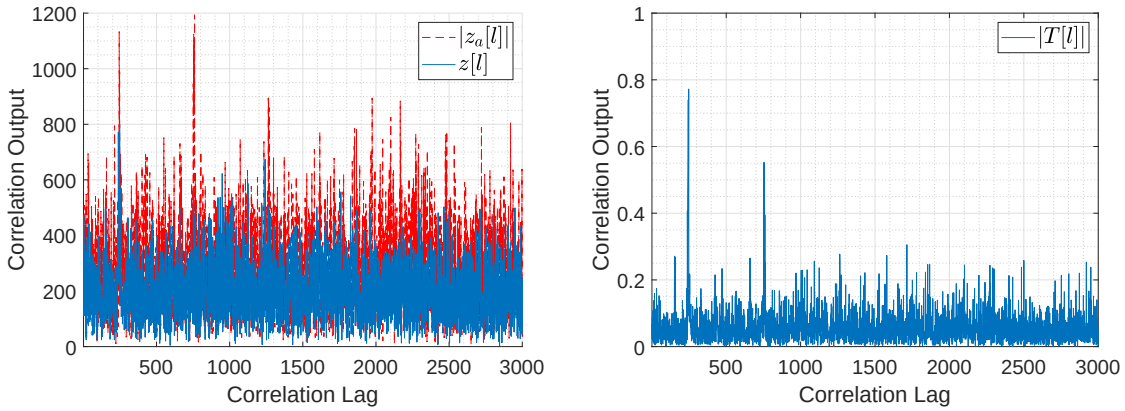

(a) Comparisons of correlation outputs

(b) Proposed normalized correlation output

Figure 4.3: The visualization of the correlation outputs over multipath channel with EVA profile in the presence of the integer CFO. With SNR = -12dB, the correlation outputs $|z[l]|$ and $|z_n[l]|$ have large noise variance. Normalized correlation gain $T[l]$ can increase correlation gain in low SNR.

To normalize the correlation output without knowledge of the channel conditions, received signal power, or noise variance, we propose a new normalization techniques by using an additional correlation function. From the RCS properties of training symbols in time-domain, the additional correlation output is defined as

$$
\begin{aligned}
z_a[l] &= \frac{4}{N} \sum_{n=0}^{\frac{N}{4}-1} r\left[l+n\right] r\left[\frac{N}{2}+l+1-n\right], \\
|z_a[l]| &\approx E_{sh}^2 + 2\sigma_\eta^2, \quad \text{for} \quad l = d, d+\frac{N}{4}, d+\frac{N}{2}, \\
|z_a[l]| &\approx 2\sigma_\eta^2, \quad \text{for otherwise.}
\end{aligned} \tag{4.22}
$$

By reducing correlation region in (4.22), consecutive correlation gains can be observed with $N/4$ interval. The comparison of correlation outputs in (4.7) and (4.22) is illustrated at Fig. 4.3 (a). In low SNR, we can observe the ambiguity of correlation output. Therefore, neither statistical-derived threshold nor conventional normalization scheme in (4.21) are applicable. By combining two correlation outputs in (4.7) and (4.22) with using point-to-point multiplication, we can simply increase the correlation gain with low SNR. Finally,

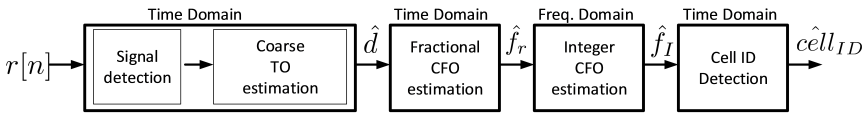

Figure 4.4: Block diagram of proposed downlink synchronization methods for UFMC systems

we can simply set the threshold to detect training signals by using proposed normalization schemes as

$$T[l] = \frac{|z[l]|\,|z_a[l]|}{\mu N_{TR} E_r[l]} \approx \frac{\left(E_{sh} + \sigma_\eta^2\right)\left(E_{sh} + 2\sigma_\eta^2\right)}{E_{sh}^2 + E_{sh}\sigma_\eta^2} \approx 1, \quad \text{when} \quad l = d, \tag{4.23}$$

where we use the received signal energy as

$$E_r[l] = \frac{1}{N + L - 1} \sum_{n=0}^{N+L-1} |r[n + l]|^2 . \tag{4.24}$$

As illustrated in Fig. 4.3 (b), the normalization output at $l = d$ is close to 1 with low SNR while the normalized correlation output is close to 0 at $l \neq d$. Therefore, we can detect the training signal while avoiding false alarm by simply setting the threshold $0.6 < \alpha < 1$. Finally, we estimate the coarse TO as

$$\hat{d} = l, \quad \text{when} \quad T[l] > \alpha, \tag{4.25}$$

The performance of signal detection and TO estimation will be evaluated through simulations with the different values of α.

4.3 CFO estimation and cell ID detection

After coarse timing estimation, the integer and fractional CFO should be estimated and compensated to avoid ICI as illustrated in Fig. 4.4. In this section, we proposed the integer and fractional CFO estimation by combining time and frequency domain-based estimation.

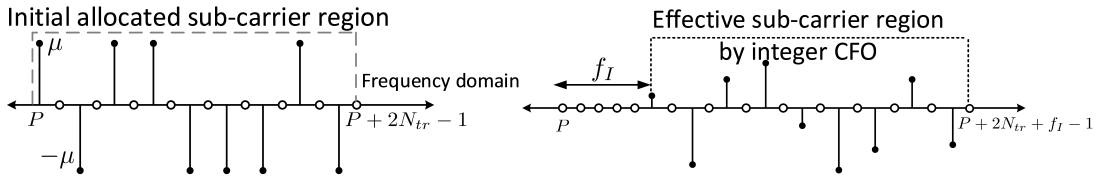

(a) Initial allocated resource at the transmitter (b) Observed allocated resource at the receiver

Figure 4.5: The example of the impact of the integer CFO f_I with frequency selective channels. The in-phase components of received signal are illustrated.

4.3.1 Fractional CFO estimation

As we illustrated in Fig. 4.1 (b), the UFMC modulated training signals contain semi-repeated signal blocks. Therefore, we use auto-correlation-based CFO estimation with identical signal blocks similar in [38] by modifying the correlation region as

$$\begin{aligned} \Gamma_{ufmc} &= \sum_{n=L}^{\frac{N}{2}-L} r(\hat{d}+n) r^*(\hat{d}+n+\frac{N}{2}), \\ \tilde{f}_r &= -\frac{1}{\pi} \angle \Gamma_{ufmc}, \end{aligned} \tag{4.26}$$

where $\tilde{f}_r$ is an initial estimated fractional CFO which can exceed the normalized sub-carrier spacing $[-0.5, 0.5]$ But, the actual estimated fractional CFO is easily calculated with following conditions

$$\begin{aligned} \hat{f}_r &= \tilde{f}_r - 1, \quad \text{when} \quad 0.5 < \tilde{f}_r < 1, \\ \hat{f}_r &= \tilde{f}_r + 1, \quad \text{when} \quad -1 < \tilde{f}_r < -0.5. \end{aligned} \tag{4.27}$$

Finally, the received signal with compensating the fractional CFO is written as

$$r_f[n] = e^{-j\frac{2\pi}{N}\hat{f}_r n} r\left[n + \hat{d}\right]. \tag{4.28}$$

4.3.2 Integer CFO estimation

Since the integer CFO is not estimated by using (4.26), we adopt the frequency domain correlation with local copy. After compensating the fractional CFO, the frequency domain equivalent received signal in (4.28) is represented as

$$R_f[k] = \begin{cases} F[k-f_I]H[k-f_I]X_{TR,u}[k-f_I] + W[k] & k \in \mathbf{RB}_t, \\ 0 \quad \text{otherwise}, \end{cases} \tag{4.29}$$

where $H[k]$ is the channel frequency response of $h[m]$, $F[k]$ is the filter frequency response, f_I is the integer CFO, and $\mathbf{RB}_t = \left[\mathrm{RB}_{t,0}, \mathrm{RB}_{t,1}, \mathrm{RB}_{t,2}, \cdots, \mathrm{RB}_{t,(B+1)N_{sc}-2}, \mathrm{RB}_{t,(B+1)N_{sc}-1}\right]^T$ is the initial allocated set of sub-carrier indices at the transmitter. Since the integer CFO lead to frequency shift at the receiver as illustrated in Fig. 4.5, the relationship between $\mathbf{RB}_t$ and the set of effective sub-carrier indices at the receiver ($\mathbf{RB}_r$) is written as

$$\mathbf{RB}_r = \mathbf{RB}_t + f_I. \tag{4.30}$$

Since the integer CFO affects sub-carrier indices, we will find the maximum frequency domain correlation gain by using point-to-point multiplication with the local sequences as

$$\begin{aligned} \Gamma_u &= \left| \sum_{k \in \mathbf{RB}_t} \frac{R^*[k] X_{TR,\tilde{u}}[k]}{F^*[k]} \right| \\ &= \left| \sum_{k \in \mathbf{RB}_t} \frac{F^*[k-f_I]}{F^*[k]} H[k-f_I]^* X_{TR,u}[k-f_I] X_{TR,\tilde{u}}[k] \right|, \end{aligned} \tag{4.31}$$

where $X_{TR,\tilde{u}}$ is the local template training sequences for the uth cell ID. We also assume the filter frequency response is known at the receiver. To estimate the integer CFO, we propose a simple method by comparing several correlation gain with changing the effective

region as

$$\Gamma\left[\tilde{f}_I, \tilde{u}\right] = \left| \sum_{k \in \mathbf{RB}_t + \tilde{f}_I} \frac{F^*[k - f_I + \tilde{f}_I]}{F^*[k]} H[k - f_I + \tilde{f}_I]^* X_{TR,u}[k - f_I + \tilde{f}_I] X_{TR,\tilde{u}}[k] \right|. \tag{4.32}$$

Then, we expect the highest correlation gain when $\tilde{f}_I = f_I$ and $\tilde{u} = u$ as

$$\Gamma\left[\tilde{f}_I, \tilde{u}\right] = \left| \sum_{k \in \mathbf{RB}_t + \tilde{f}_I} H[k] \left| X_{TR,u}[k] \right|^2 \right| = \mu^2 \left| \sum_{k \in \mathbf{RB}_t + \tilde{f}_I} H[k] \right|. \tag{4.33}$$

By using 2-dimension search with (4.32), we can estimate the integer CFO and cell ID over the flat fading channels. However, the outputs of $\Gamma[\tilde{f}_I, \tilde{u}]$ is not reliable over the frequency selective channel. To avoid the uncertainty of estimation by using (4.32), we proposed the weight function as following

$$\beta\left[\tilde{f}_I\right] = R\left[RB_{t,0} + \tilde{f}_I\right] R\left[RB_{t,2N_{tr}-2} + \tilde{f}_I\right], \tag{4.34}$$

where $\beta\left[\tilde{f}_I\right]$ contains the product of the frequency response of the first and last effective sub-carrier indices at the receiver. Specifically, the proposed training sequences are allocated to even sub-carrier indices, $\beta\left[\tilde{f}_I\right]$ contain null sub-carrier index when $\tilde{f}_I \neq f_I$. For example, $\beta\left[\tilde{f}_I\right]$ in Fig. 4.5 contains the largest value when $\beta\left[f_I\right] = \left|R\left[P + f_I\right]\right| \left|R\left[P + 2N_{tr} + f_I\right]\right|$. Finally, the weight function $\beta\left[\tilde{f}_I\right]$ provides the following properties

$$\left|\beta\left[\tilde{f}_I\right]\right| \approx \begin{cases} \left|F[RB_{r,0}]H[RB_{r,0}]|F[RB_{r,2N_{tr}-2}]|H[RB_{r,2N_{tr}-2}]|\mu^2\right|, & \text{when} \quad \tilde{f}_I = f_I, \\ 0, & \text{otherwise.} \end{cases} \tag{4.35}$$

By combining the proposed weight function and (4.32), the integer CFO is estimated as

$$\hat{f}_I = \arg\max_{\tilde{f}_I} \left| \beta \left[\tilde{f}_I \right] \right| \Gamma \left[\tilde{f}_I, \tilde{u} \right], \quad \forall \tilde{u} \tag{4.36}$$

Since all cell ID utilize the identical resource allocation $\mathbf{RB}_t$, the high correlation gain is expected in each different set of training sequences when $\tilde{f}_I = f_I$. Finally, the coarse synchronized signal by compensating the coarse TO and the CFO as

$$\tilde{r}[n] = e^{-j\frac{2\pi\hat{f}_I}{N}n} r_f[n], \quad n \in [0, N_s(N + L_f - 1)]. \tag{4.37}$$

By using 2-dimensional search algorithm, (4.36) may be applicable for the cell ID detection. However, the frequency selective channel leads the following properties

$$\left| \sum_{k \in \mathbf{RB}_t + \tilde{f}_I} \frac{F^*[k - f_I + \tilde{f}_I]}{F^*[k]} H[k - f_I + \tilde{f}_I]^* X_{TR,u}[k - f_I + \tilde{f}_I] X_{TR,\tilde{u}}[k] \right| \neq 0 \quad \text{for} \quad u \neq \tilde{u}. \tag{4.38}$$

Since the outputs in (4.38) is dependent to $H[k]$, the training sequence for different cell ID can introduce the highest correlation gain as the worst case. Therefore, the alternative way to detect the cell ID should be considered.

4.3.3 Cell ID detection

Since the integer and fraction CFO effects have been compensated, we can use the good properties of cross-correlation by employing local templates in time-domain for cell ID detection as

$$\Delta^u = \sum_{n=0}^{N+L_f-1} \tilde{r}[n] s_{TR}^u[n]^*,$$

$$\hat{SectorID} = \arg\max_u \{\Delta^u\}, \quad u \in \{0, 1, 2\} \tag{4.39}$$

where the local templates are UFMC modulated reference signal with three different training sequences for each cell ID. Therefore, the cell ID can be easily estimated by comparing the cross-correlation output in (4.39).

4.4 Simulation Results

In this section, we compare the performance of some of the existing synchronization schemes in the literature with the proposed algorithms through Monte Carlo simulations. The total number of sub-carriers is $N = 2048$, number of sub-bands $B = 6$, and each sub-bands contain $N_{sc} = 12$ sub-carriers. We adopt the Dolph-Chebyshev filter with 40dB sidelobe attenuation as a prototype waveform filter [20]. Then, we choose the filter-length based on Proposition. 3. The extended vehicular A (EVA) channel model [60] is used as multipath fading channels with Rayleigh fading. The range of the integer CFO f_I is randomly chosen between $[-2, 2]$, the fractional CFO f_r is generated between $[-0.5, 0.5]$, and TO d is generated between $[0, N/8]$. The number of 20 data symbols are transmitted followed by the training symbol. Since the proposed synchronization algorithms use the training sequences with null sub-carriers, the frequency-domain linear interpolation is used for channel estimation. Then, simple one-tap frequency domain zero forcing equalizer is employed at the decoder. In the case of time-domain generated preambles in [44, 45], the QPSK modulated symbols for channel estimation are inserted between training symbols and data symbols. Moreover we combine algorithms for integer CFO estimation in [62] and the coarse TO and fractional CFO estimation in [37], by using two identical training symbols in frequency domain.

4.4.1 Performance of the Training Block Detection

In Fig. 4.6, we compare the performance of signal detection P_d with statistical threshold with the NP criterion in (4.20) and proposed normalization techniques with different values α in (4.25). As we expected, the proposed normalization schemes provide higher chance of

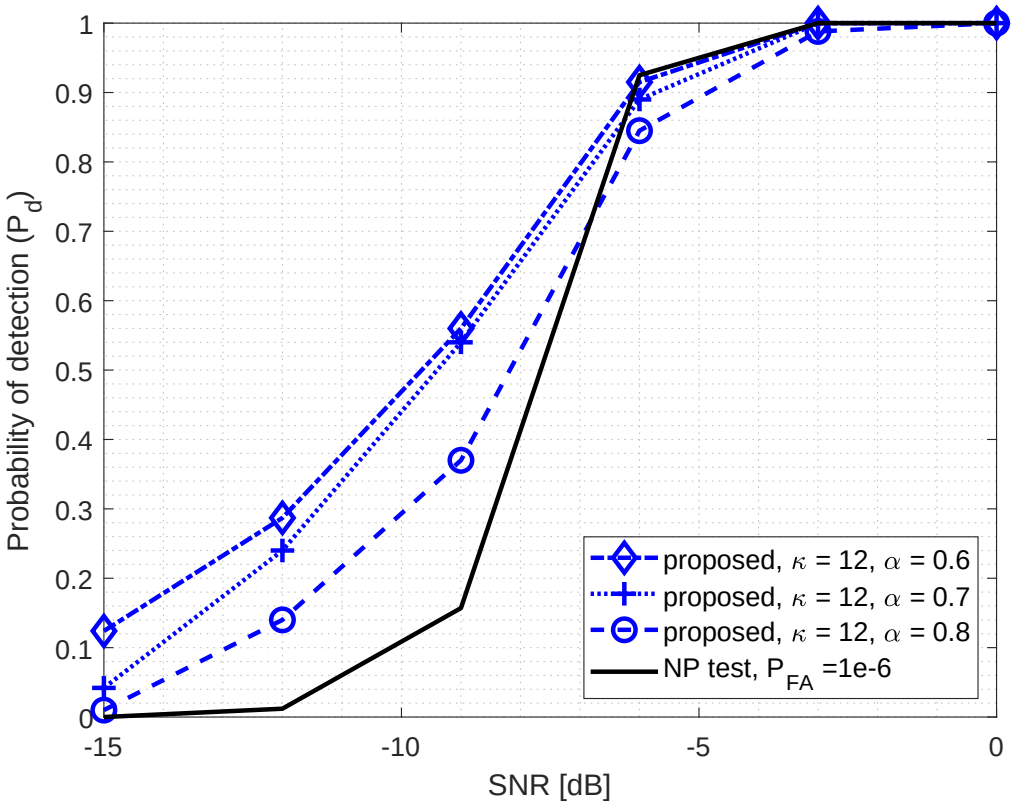

Figure 4.6: Comparison of the probability of detection P_d for the training block detection with the NP criterion and proposed normalization method over the multipath fading channels

signal detection in low SNRs compared to signal detection with the NP-derived threshold. Obviously, large value of α shows the worse performance. Specifically, $\alpha = 0.8$ shows the worst performance among the proposed scheme with different α. By using the proposed normalization methods we observe that the detection probability of proposed scheme is approximately 99% at -3dB SNR. Finally, the proposed scheme provides similar detection performance as statistical-derived threshold-based detection for SNR > -3dB.

4.4.2 Performance of the coarse timing estimation

In Fig, 4.7, we compare the performance of various TO estimation algorithms in terms of root mean square error (RMSE). The RMSE of TO is calculated by $\left(\sqrt{E\left[|d-\hat{d}|^2\right]}\right)$. In [44], the coarse TO is estimated by using cross-correlation with local copy of ZC se-

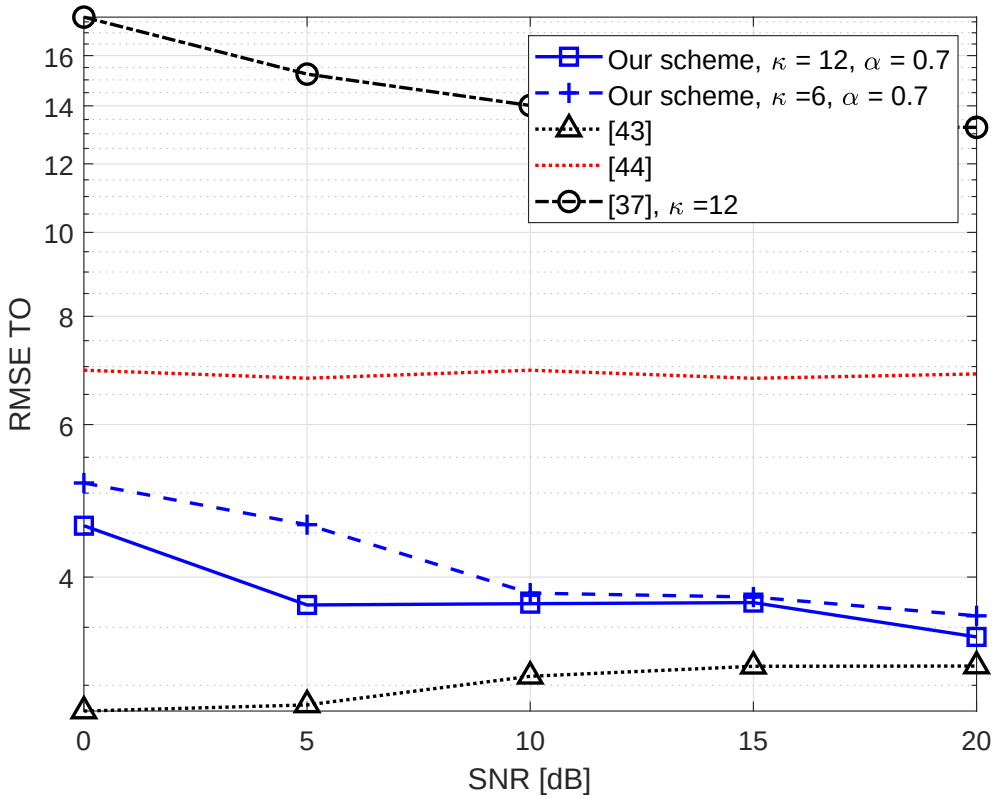

Figure 4.7: Performance of the coarse TO estimation compared with the existing methods over multipath fading channels

quences. After estimating the integer and fractional CFO, the estimated TO is refined. Therefore, the fine timing synchronization in [44] provides the best accuracy by removing the bias of the integer CFO. In [45], the auto- and cross-correlation are combined with using arbitrary generated conjugate symmetric training sequence by employing m-sequences for the TO estimation. Since auto-correlation-based scheme is robust to the multipath fading channels, the performance of TO estimation in [45] is worse than proposed algorithms. Moreover, the integer CFO is not considered in [45]. Unlike to training sequences in [44, 45], the proposed training sequences are inserted over multiple sub-carriers in the frequency domain. By using the RCS properties of UFMC training symbol, TO is estimated in (4.25) with combining proposed normalization techniques. We observe that the performances of different filter lengths with $L = \lfloor N/12 \rfloor, \lfloor N/6 \rfloor$ are similar. Finally, we illustrate the auto-

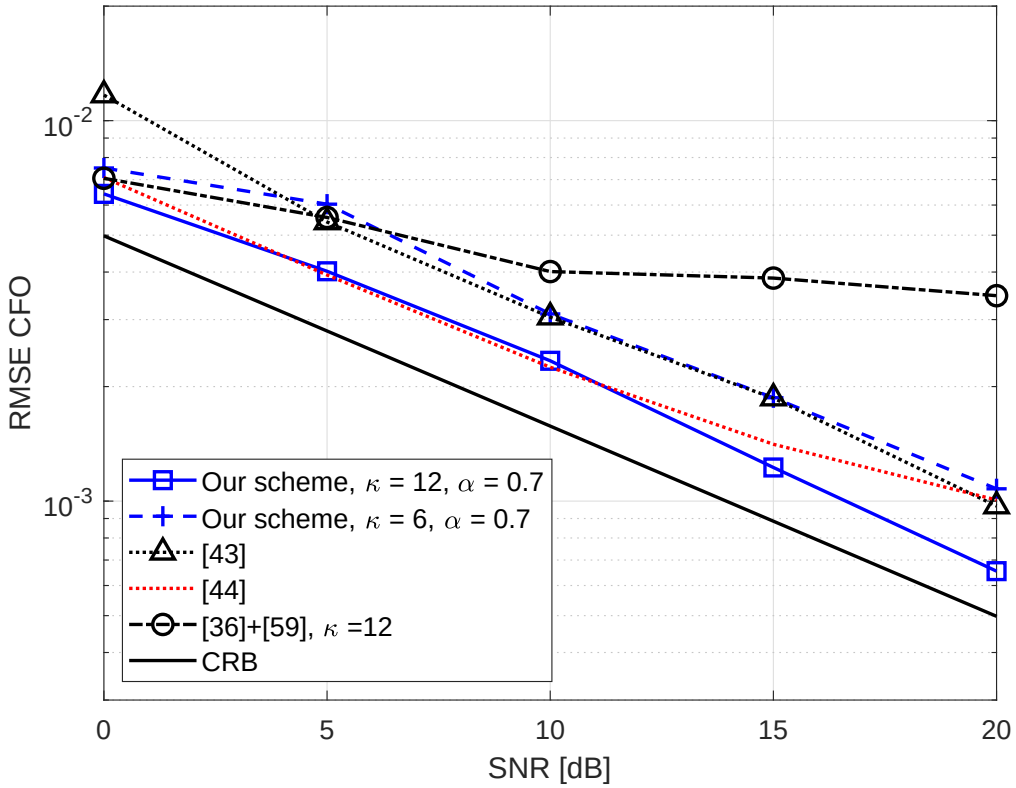

Figure 4.8: Performance of the CFO estimation compared with the existing methods over multipath fading channels

correlation with two identical training symbols [38] in the presence of the integer CFO. Since the metric in [38] has a plateau, the RMSE of TO is the worst from the uncertainty of the starting point.

4.4.3 Performance of the CFO estimation

In Fig. 4.8, we illustrate the performance of CFO estimation with RMSE of the CFO estimation $\left(\sqrt{E\left[|f-\hat{f}|^2\right]}\right)$. The Cramér-Rao bound (CRB) in [38] is included for a reference. In [44], the integer CFO is estimated by comparing correlation outputs with two set of ZC sequences. In [45], only performance of the fractional CFO estimation is evaluated. The CFO estimation in [38] with different correlation regions is employed for the fractional CFO estimation. By analyzing the time-domain CFO estimation, the

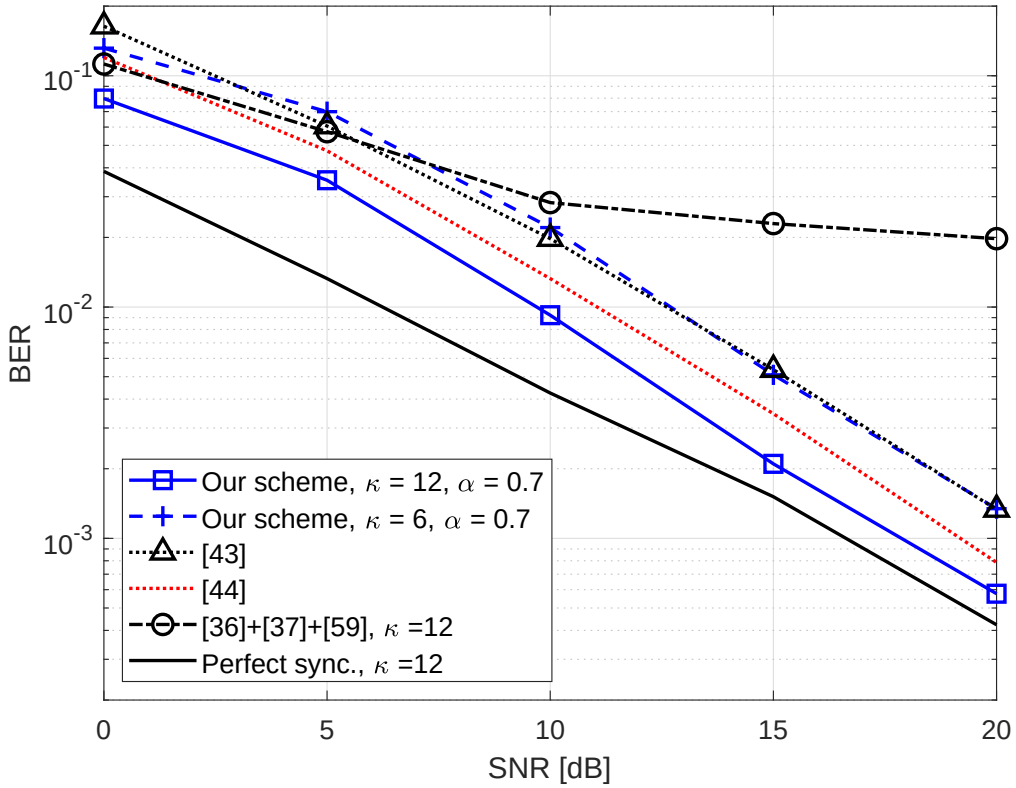

Figure 4.9: Comparison of bit error-rate performances over multipath fading channels.

sequences in [45] is more robust to the multipath channels than sequences in [44]. However, the frequency domain integer CFO estimation in [62] and fractional CFO estimation in [37] show the worst performance in high SNR due to the filter frequency responses. Finally, we observe that the proposed algorithm with $\kappa = 12, \alpha = 0.7$ provide the best CFO estimation accuracy. However, the performance of CFO is degraded when increasing the length of filter with $\kappa = 6$ by losing the identical signal blocks.

4.4.4 Performance of Bit Error-Rate

Fig. 4.9 shows the comparison of bit error-rate (BER) performance. We assume that the training sequences are known at the receiver. Then, we employ a one-tap frequency domain zero-forcing equalizer. Since training sequences in [44, 45] are generated in time-domain, UFMC modulated reference symbols with QPSK modulation are transmitted for the chan-

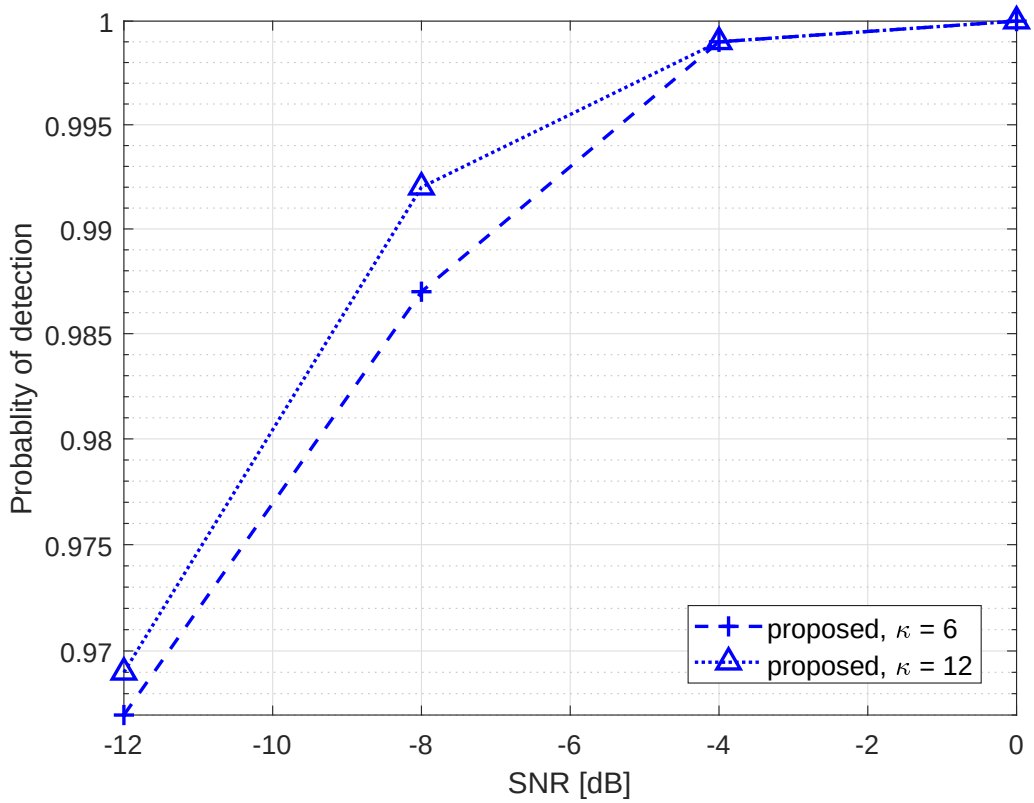

Figure 4.10: Comparison of cell ID detection with different filter length.

nel equalization. Moreover, the perfect synchronization with channel estimation has been plotted as a reference. We observe that the proposed methods with $\kappa = 12$ provide the best performance. Although the timing synchronization in [44] provides the best performance, less accuracy of estimated CFO leads to the performance degradation. While the performance of CFO estimation is similar in [45] and proposed methods, the system performance with [45] is worse than the proposed scheme because of inaccuracy of TO estimation. Moreover, the combination of [37, 38, 62] for joint synchronization methods with two identical training symbols provide the worst system performance. Finally, we observe that the UFMC systems are more sensitive to the CFO mismatch than TO mismatch similar to OFDM systems.

4.4.5 Performance of cell ID detection

In Fig. 4.10, we illustrate the performance of cell ID detection in (4.39) after compensating TO and CFO with proposed algorithms. We calculate the probability of cell ID detection after detecting training signals. Obviously, the shorter filter length provides better detection performance. Finally, we observe that proposed training sequences in frequency-domain provide the signal orthogonality in time domain among different training signals from different cells.

CHAPTER 5

ASYNCHRONOUS MULTI-USER UPLINK TRANSMISSIONS FOR 5G WITH UFMC WAVEFORM

In this chapter, we propose a new UFMC receiver structure to support asynchronous uplink transmission with FDMA. Since UFMC transmitter contains multiple sub-band filters, we adopt equivalent filters at the receiver to separate and extract different sub-band signals among multi-users. Moreover, we suggest the coarse timing synchronization algorithm with using a single synchronization symbol. The analysis of the proposed system performance has been illustrated with conventional SC-FDMA systems. We also present the demonstration of the proposed systems and algorithms.

5.1 Coarse TO and CFO Estimation

As illustrated in Fig. 2.3, the mixed MU received signal is filtered with multiple sub-band filters at the receiver. The target UE signal in the ith sub-band signal is illustrated in (2.13). To determine the presence of signals in the ith sub-band, we first detect the training symbols then estimate TO. The prosed signaling frame structure is illustrated in Fig. 3.1. Single resource block (RB) is carrying the training sequences with using ZC sequences [43] as

$$a_{zc}^{m}(n) = e^{j\frac{\pi}{N_{zc}}u^{(m)}n^2}, \quad 0 \leq n \leq N_{ZC} - 1 \tag{5.1}$$

where $N_{zc} = \lfloor TRB_i/2 \rfloor$ is the length of ZC sequence, TRB_i is the total number of sub-carriers at ith RB, $\lfloor \cdot \rfloor$ is the floor function, and $u^{(m)}$ is the root index for the mth user which is the positive integer and relatively prime to N_{zc}. Since our proposed UFMC receiver contains sub-band filters $f_i(l)$, multi-user interference (MUI) can be removed from filtering operation. Therefore, users can transmit the synchronization symbol with either different

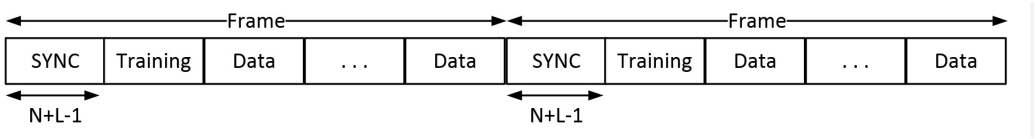

Figure 5.1: Proposed signaling frame structure for UFMC systems.

$u^{(m)}$ or shared u through different sub-band RB_i. Now, we introduce the useful properties of IFFT to detect the synchronization symbol. Since the length of ZC sequence is half size of RB, ZC sequence at the ith RB can be allocated as

$$\begin{aligned} X_i(k)^m &= a_{zc}^m(k), \quad \text{if } k \text{ is even} \\ X_i(k)^m &= 0, \qquad \text{if } k \text{ is odd.} \end{aligned} \tag{5.2}$$

Therefore, IFFT output in (2.10) with even-subcarrier allocation scheme shows a repetition property as

$$x_i(n) = x_i(n + \frac{N}{2}), \quad 0 \leq n \leq \frac{N}{2} - 1. \tag{5.3}$$

Finally, the ith sub-band correlation function can be derived as [38]

$$\Lambda_i(l) = \left| \sum_{n=l}^{l+\frac{N}{2}-1} r_i(n) r_i^*(n + \frac{N}{2}) \right|, \tag{5.4}$$

where l is the correlation lag, $|\cdot|$ is an absolute function, and $*$ indicates the complex conjugate. Unlike OFDM signal, UFMC signal contains filter ramp up/down at the beginning/end of symbol as illustrated in Fig. 5.2. We observe that dominant UFMC signal region is considered as $[L/2, \quad L/2 + N - 1]$. However, our proposed receiver adopts FIR filters, the dominant information of UFMC symbol is allocated at $[L, \quad L + N - 1]$. Finally, we can estimate the symbol timing as

$$\hat{d}_i = \text{argmax}\{\Lambda_i(l)\} - L, \quad d \in (-\infty, \infty). \tag{5.5}$$

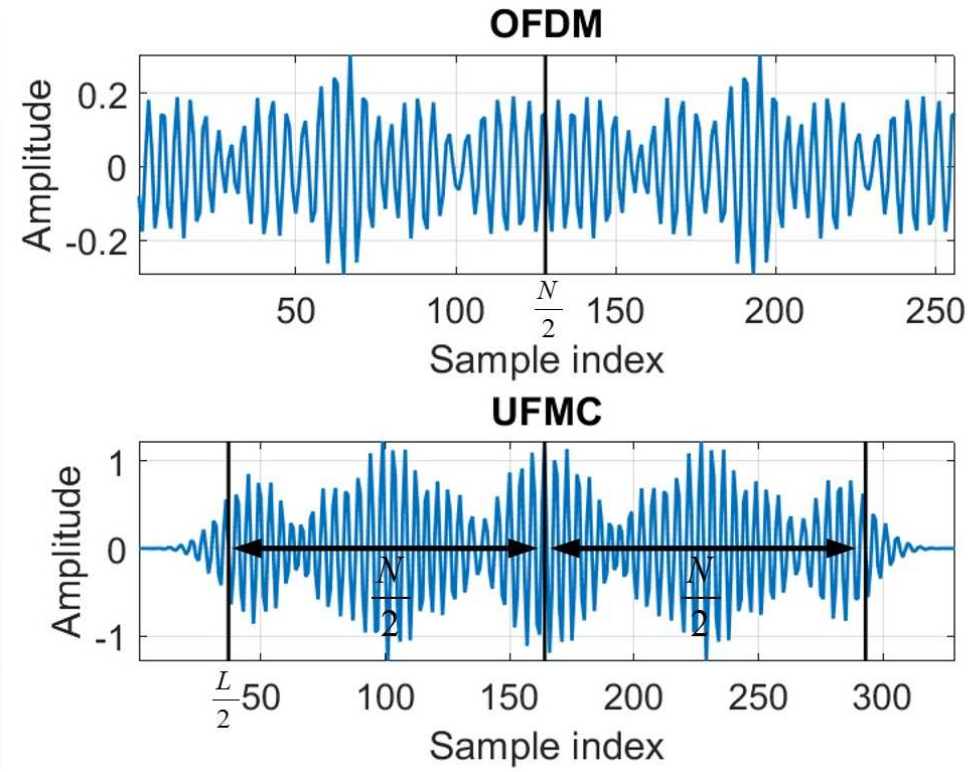

Figure 5.2: Comparison In-phase transmitted synchronization symbol waveform between OFDM and UFMC.

5.2 Decoder

After estimating the symbol timing, corresponding sub-band received signals are free from MUI because of filter operation in (2.12) and (2.13). However, the received symbol introduces inter-symbol interference (ISI) from another filtering at the receiver which is illustrated in Fig. 5.3. We already observed that UFMC waveform contains dominant information between $[L/2, L/2 + N - 1]$. Therefore, we can keep the equivalent FFT window as conventional UFMC system to decode filtered-received symbol as drawn in Fig. 5.3.

After coarse timing synchronization, the FFT window contains following signals

$$\hat{\mathbf{r}}_i = \left[\hat{r}_i(\lfloor\frac{L}{2}\rfloor), \hat{r}_i(\lfloor\frac{L}{2}\rfloor + 1), \cdots, \hat{r}_i(\lfloor\frac{L}{2}\rfloor + N + L - 1)\right], \tag{5.6}$$

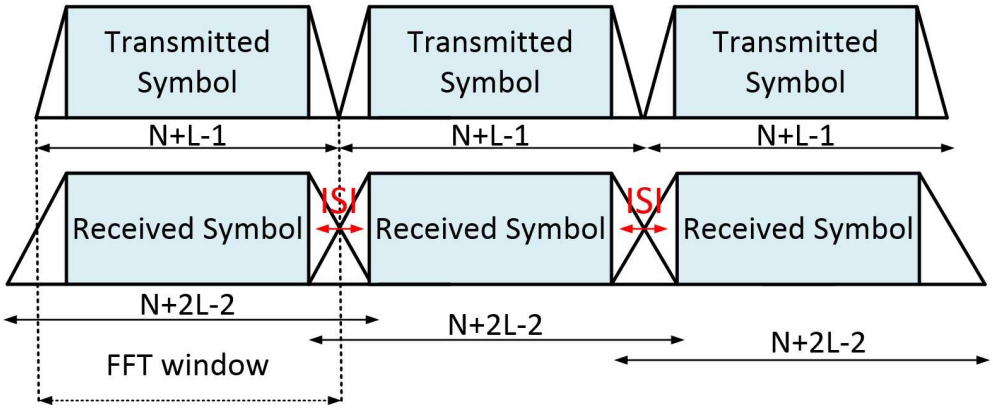

Figure 5.3: Comparison between transmitted and filtered-received UFMC symbol.

where $\hat{r}_i(n) = r_i(n + \hat{\tau}_i)$. Therefore, a $2N-$point FFT output can be obtained as

$$\hat{\mathbf{R}}_i = \text{FFT}\{\hat{\mathbf{r}}_i, 0, \cdots, 0\}, \tag{5.7}$$

where $\hat{\mathbf{R}}_i$ is the length of $2N$ frequency domain received signal and the length of $N - L + 1$ zeros are appended. As similar as conventional UFMC decoder, we discard odd sub-carriers to recover the length of N frequency domain received signal $\tilde{\mathbf{R}}_i$. Then frequency domain received signal, corresponding to ith sub-band, can be extracted as $\tilde{\mathbf{R}}_{RB_i}$. Since data symbols are transmitted following the training symbol, polluted received data symbol by filters, noise, and channel can be easily recovered by conventional OFDM equalization schemes.

5.3 Simulation Results

In this section, we compare the performance of proposed UFMC system with the conventional UFMC system and SC-FDMA system for multi-user uplink transmission. Moreover, we present the comparison of system performance without synchronization. Then, we examine the performance of proposed coarse TO estimation along with symbol error rate (SER). Transmitted signal structure is simulated in the form of proposed frame structure, where each frame contains a single synchronization symbol, single training symbol for

channel estimation, and 4 data symbols. The simulations are performed using the following configuration. We adopt the length of $L = 74$ Dolph-Chebyshev FIR filter where the side-lobe attenuation of filter is set as 80 dB. The IFFT size at each UE is $N = 256$, while 512-point FFT is used at BS. Moreover, UEs are allocated at 4 different sub-bands, where each sub-band contains 13 sub-carriers. For multiple access scheme, we adopt FDMA. Synchronization symbols contain 7-length ZC sequences $N_{ZC} = 7$, where the root index is set as $u^m = 23 + 3m$, m is user index. Training symbols and data symbols are modulated with QPSK. To decode the symbols, we adopt a frequency domain zero-forcing (ZF) equalizer with the known training symbol. Moreover, multiple TOs are randomly generated within $[0,\ N + L - 1]$.

5.3.1 TO and CFO effects

In Fig. 5.4 (a) and Fig. 5.4 (b), we illustrate the system performance degradation from TO and CFO. As we mentioned, UFMC systems support relaxed synchronization requirements compare to OFDM systems. However, TO and CFO still degrade the system performance. As illustrate in Fig. 5.4 (a), the conventional UFMC systems show the robustness of TO mismatch without using CP. Similar to OFDM system, SC-FDMA systems require strict synchronization requirements. If the TO is smaller than CP length, there is no performance degradation with compensating the phase shift in frequency domain. However, we observe the performance degradation when the TO is larger than the CP or TO < 0. Therefore, SC-FDMA uplink systems require TAS which make arriving MU signals at BS within the CP duration. Although proposed systems for asynchronous transmission shows less sensitivity of TO mismatch compare to SC-FDMA systems, the proposed receiver structures have severe performance degradation from TO. Unlike to the TO effect, most of multi-carrier systems are sensitive to the CFO mismatch as illustrated in fig 5.4 (b). Since the proposed UFMC systems with sub-band filters at receiver introduce the ISI, the ISI can be increasing if the FFT window in fig 5.3. Therefore, TO and CFO should be estimated and compensated

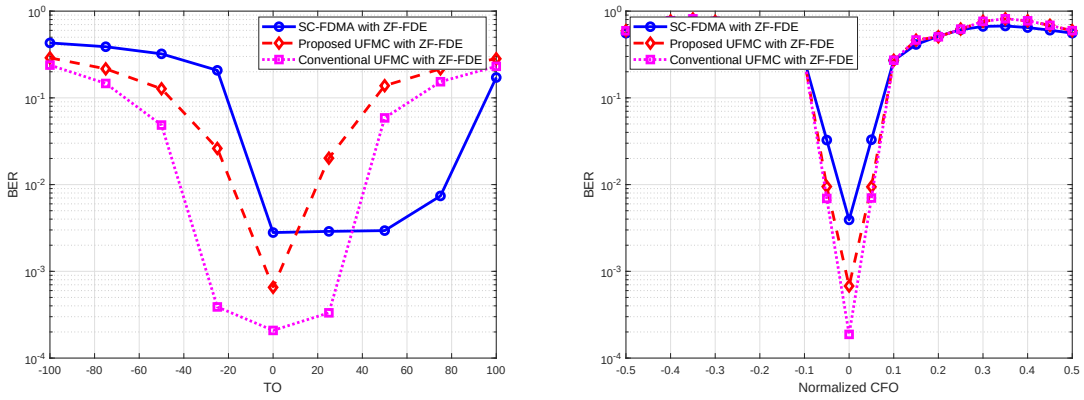

(a) TO effect to system performance

(b) CFO effect to system performance

Figure 5.4: System performance degradation from TO and CFO over flat fading channel with SNR=10dB.

to avoid performance degradation.

5.3.2 Filter responses and Guard sub-carriers

We analyze the filter responses with various filter lengths. It is obvious that longer filter responses in time domain provide sharp cut-off frequency. Since the proposed UFMC receiver contains multiple sub-band filters to extract MU signals, the cut-off frequency is one of the important factor to avoid MUI. In Fig. 5.5, the comparison of filter responses with different filter length is illustrated. The filter length is selected $L \in [74, 128, 256, 384, 512]$ and FFT size 2048. As shown in Fig. 5.5, the cut-off frequency is larger with shorter filter length. Specifically, the filter with $L = 512$ extract the 6 sub-carriers and interferences from adjacent sub-carriers can be reduced. Moreover, the 1 guard sub-carrier may be required to avoid the MUI from adjacent sub-band UE. Unlike to filter with $L = 512$, the output of sub-band filter with $L = 256$ contains 12 sub-carriers. In other words, the sub-band filter output contains not only target UE signal but also MU signals. Therefore, at least 6 guard sub-carriers are required to avoid MUI for $L = 256$ lengths of sub-band filter.

We also evaluate the system performance in terms of bit-error rate (BER) with different number of guard sub-carriers with $L = 256$ lengths of sub-band filters along with 2048

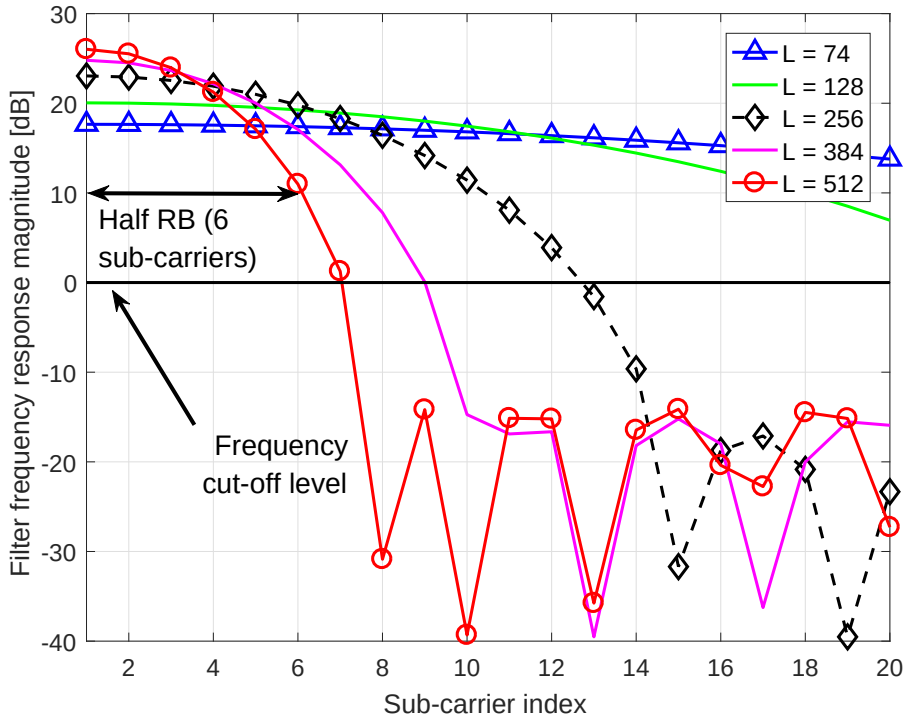

Figure 5.5: The visualization of filter frequency response with various filter lengths

FFT size. As illustrated in Fig. 5.6, the MUI level is increasing by decreasing the number of guard sub-carriers compared to single UE case. As we expected, the MUI is minimized when we use the 6 sub-carriers (half RB) as the guard band. However, severe performance degradation is observed with insufficient guard sub-carriers. Therefore, filter length and guard sub-carriers are well selected to support asynchronous transmission with minimizing the MUI.

5.3.3 Performance Evaluation

We evaluate the performance of coarse timing synchronization for the target user in (5.5) in terms of mean squared error (MSE) of coarse TO estimation where the MSE is calculated as $\mathrm{E}[|\hat{d}_i - d_i|^2]$. As illustrated in Fig. 5.7, the proposed receiver shows similar performance between single user and MU transmission. This results indicate that the proposed system can extract the target UE signal by reducing MUI.

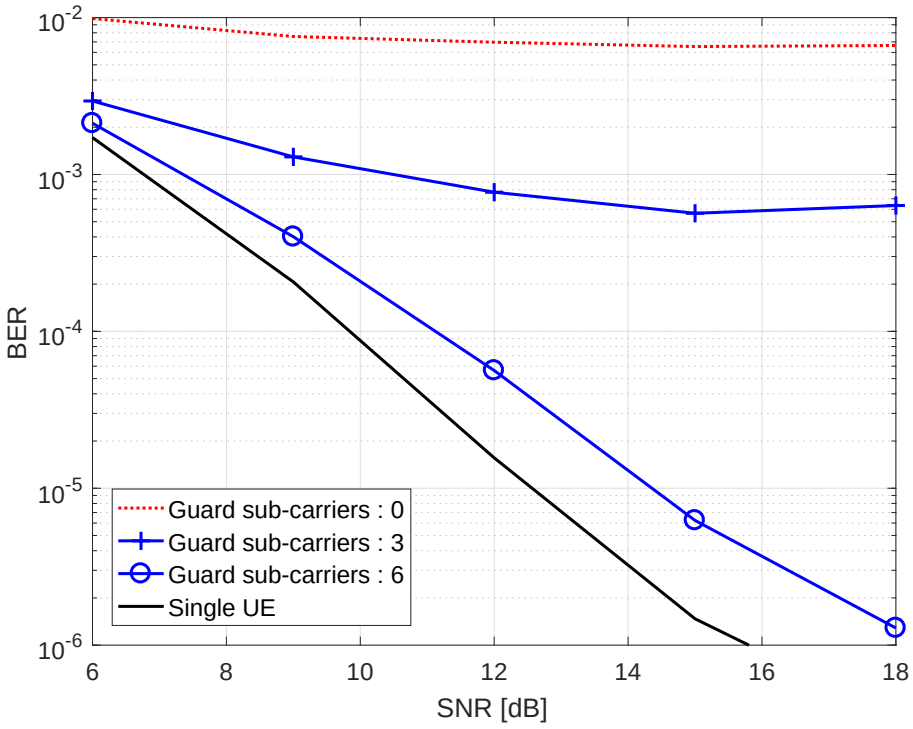

Figure 5.6: The performance comparison of proposed UFMC system with different number of guard sub-carriers

In the presence of 4 multi-user signals with different root index u^m, where $m = \{0, 1, 2, 3\}$, where $\hat{\tau_0}$ is the estimated TO for the target UE signal. The simulation result shows that the MSE of symbol timing estimation with asynchronous multi-user signals is similar to that of single user case. Therefore, our receiver can separate target UE signals and remove MUI near perfectly.

Secondly, we compared the symbol error rate (SER) of the proposed UFMC receiver over asynchronous uplink transmission to synchronous uplink transmission with conventional UFMC and SC-FDMA system in Fig. 5.8. In the case of synchronous uplink transmissions, we ignored TO from each user. Therefore multi-user signals are perfectly aligned. With above condition, the conventional UFMC system shows the best performance compared to others. Since our proposed UFMC system ignored some portions of UFMC symbol, we lose information from filter ramp up/down. Moreover, filtering operation introduces ISI as shown in Fig. 5.3. Therefore, the SER performance of proposed

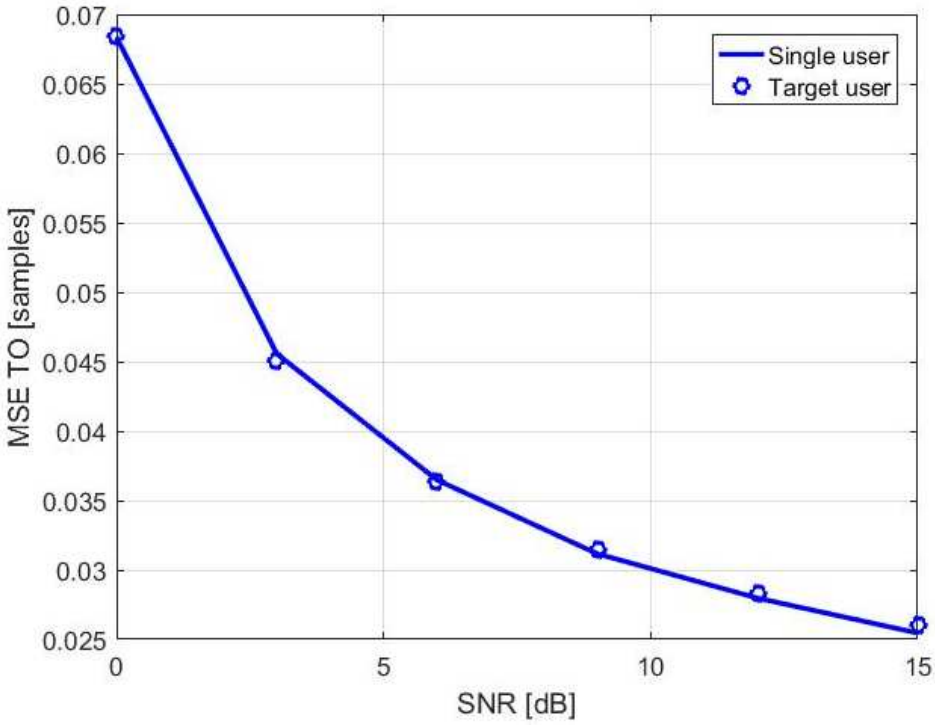

Figure 5.7: The performance comparison of a coarse TO estimation between single user case and target user signal in the presence of asynchronous multi-user signals with proposed UFMC receiver.

system is worse than the conventional UFMC system, but shows better performance than SC-FDMA with synchronous multi-user transmission. In the case of asynchronous uplink transmission, multiple TOs are randomly generated within one symbol length. Since we adopt coarse timing synchronization, imperfect timing offset estimation will degrade system performance. However, our proposed system over asynchronous transmission still shows better SER performance than conventional SC-FDMA.

Finally, we analyzed peak to average power ratio (PAPR) with the complementary CDF (CCDF) as illustrated in Fig. 5.9. It is well known that the PAPR is one of the major issues for battery-based UE. As shown in Fig. 5.9, current SC-FDMA modulation still shows the best PAPR reduction compared to that of DFT-spread UFMC, inserting DFT operation before sub-carrier allocation similar to SC-FDMA, and conventional UFMC. For example, when $CCDF = 10^{-3}$, the PAPRs are 7.5dB, 9.5dB, and 11.6dB for SC-FDMA, DFT-

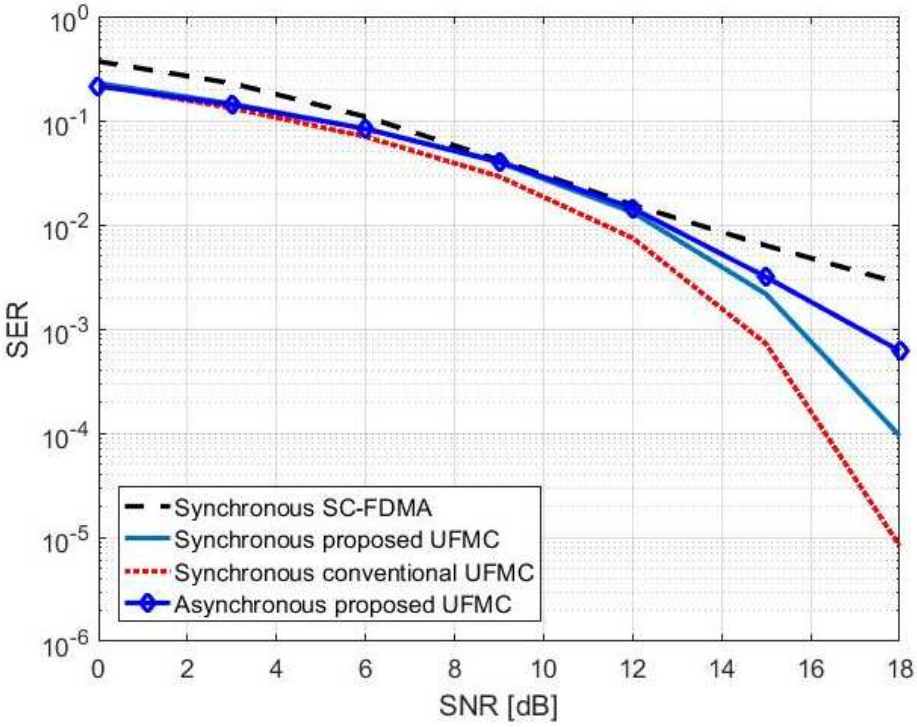

Figure 5.8: Target user SER performance comparison between asynchronous transmission and synchronous transmission over AWGN with 4 multi-users.

UFMC, and UFMC signals, respectively. Therefore, alternative PAPR reduction techniques should be researched for battery-based UEs.

5.4 Demonstration Over-the-air Transmission

This section presents the details of wireless test-bed demonstration for asynchronous multi-user uplink transmission with UFMC waveforms. We have implemented a 1 base-station and 2 MUs, each with one antenna as illustrated in Fig 5.10. But two MU are not synchronized each other. Therefore, the test-bed acts like asynchronous MU uplink transmission. The test-bed is implemented with using USRP[1]-based platform provided by National Instruments (NI) corporation. To program and control the USRP, LabVIEW® is used for the software tool.

[1]USRP stands for Universal Software Radio Peripheral

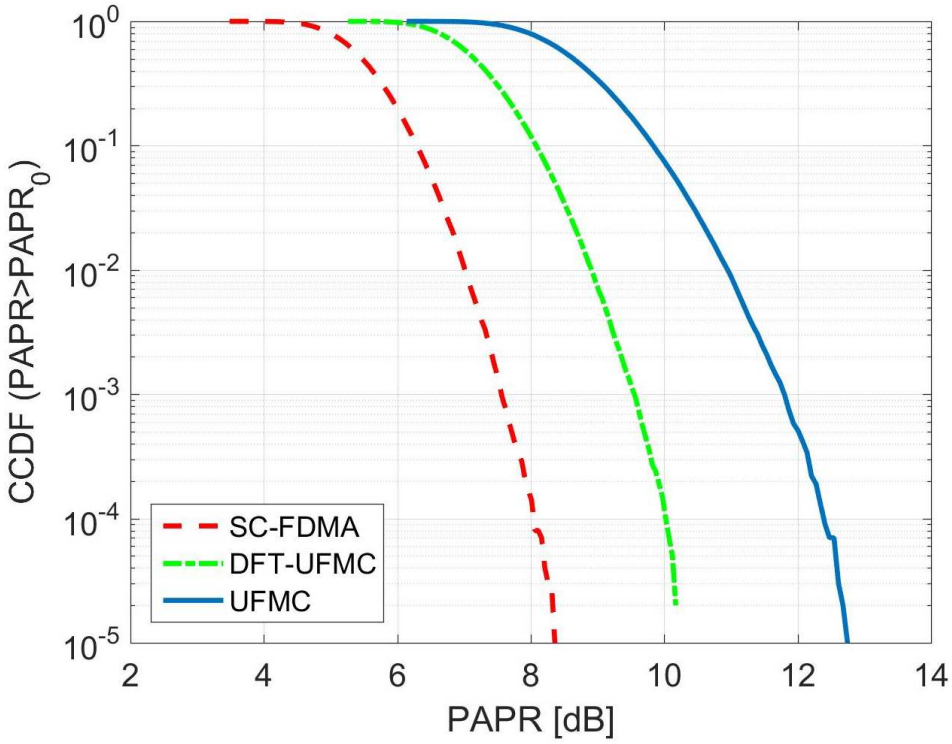

Figure 5.9: Analysis of transmitted signal PAPR among UFMC, DFT-spread UFMC, and SC-FDMA with 4 sub-bands.

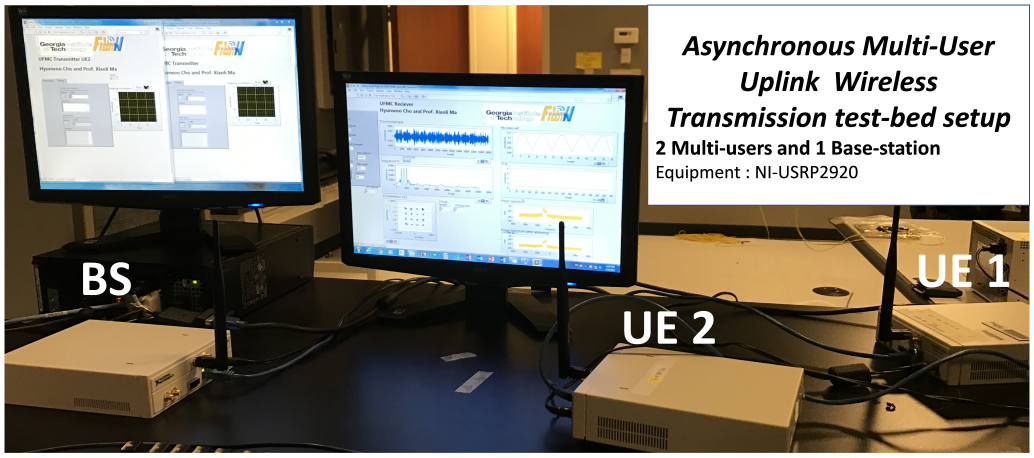

Figure 5.10: Over-the-air transmission demonstration

5.4.1 Introduction to NI USRP platform

NI's USRP platform, software defined radio device, is suitable for prototyping wireless communication systems. A snapshot for NI USRP−2920 support the carrier frequency

Table 5.1: UFMC system parameters used in wireless test-bed

Parameter	Value
Sampling Frequency	500 kHz
FFT Size	2048
Filter Length	256
Sub-carrier Spacing	244 Hz
Bandwidth for each UE	30 kHz
Allocated Sub-carrier for each UE	120
Modulation scheme	QPSK, 16-QAM

range between 50 MHz to 2.2 GHz. The RF transceiver supports up to 40 MHz bandwidth (BW) and 50 MS/s sampling rate with 8-bit sample width while 20 MHz BW and 25 MS/s sampling rate with 16-bit sample width. LabVIEW® software provides a graphical programming language to control NI-USRP system parameters such as sampling rate, carrier frequency, and transmit power. Moreover, any user-defined function can be programmed by combining multiple function nodes in the Labview.

5.4.2 UFMC System Parameters

The physical layer parameters have been chosen based on hardware specification. To avoid the data overflow among NI-USRPs and PC, the parameters are carefully selected as listed in Table 5.1. Each UE follows the frame structure illustrated in Fig. 5.1 with 20 data symbols.

5.4.3 System Demonstration

In Fig. 5.12, we observed the received signal and power spectral density (PSD) from two uplink transmissions. Since UE 2 is closer to the BS compared to UE 1, it is obvious that the received signal power of UE 2 is stronger than UE 1. By using the receiver structure in Fig. 2.3, the target signal will be extracted while filter out other UE signals. Therefore, we expect that the multi-user interference from asynchronous transmission can be reduced.

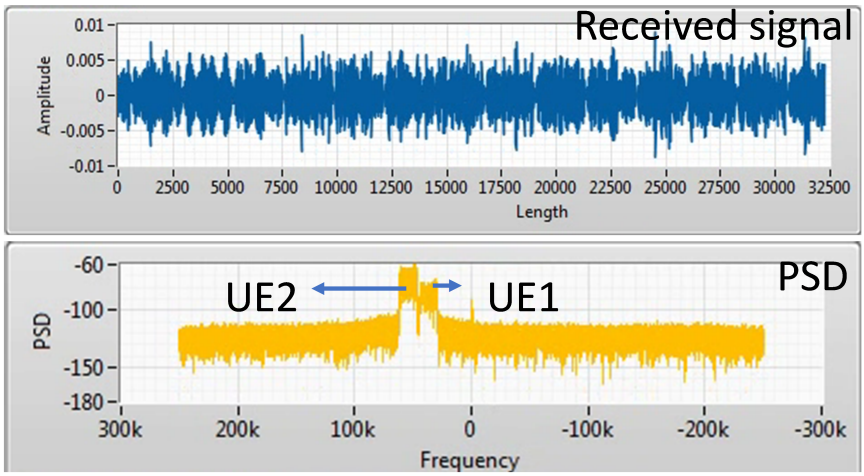

Figure 5.11: Received signal and power spectral density

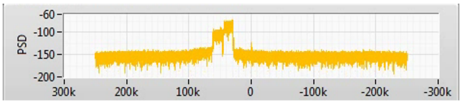

(a) Power spectral density of UE 1

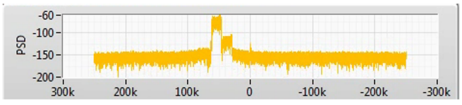

(b) Power spectral density of UE 2

Figure 5.12: Comparison of power spectral density for each target UE

In Fig. 5.12, the comparisons of PSD are illustrated. From the sub-band filters at the receiver, the target sub-bands are extracted. Moreover, the multi-user-interference can be reduced. As illustrated in Fig. 5.12 (a), we observe that the signal power for UE 1 is higher than UE 2 from the filtered output. Even the distance gap between UE 1 and BS is larger than that of UE 1, the system can extract target UE. Similarly, we easily observe that the interference from UE 2 is reduced in the case of UE 2 at Fig. 5.12 (b). In Fig. 5.13, the comparisons of demodulated data symbols are illustrated as constellation symbols. Once target UE signals are extracted, each TO and CFO are estimated and compensated by combining (5.5) and [38]. Then, reference symbols followed by synchronization symbol in Fig. 5.12 are used for frequency domain channel equalization. As observed in Fig. 5.13, the BS can decode asynchronous MU signals.

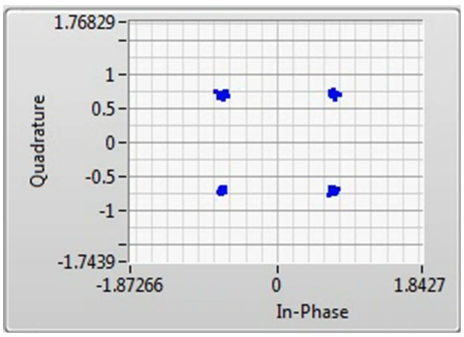

(a) Constellation of UE 1

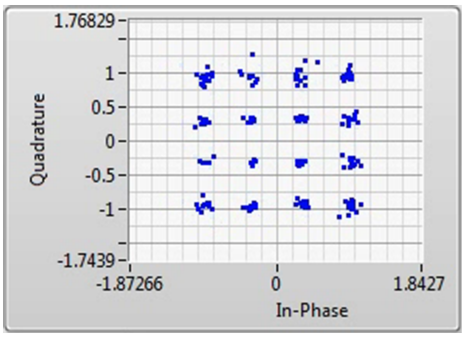

(b) Constellation of UE 2

Figure 5.13: Comparison of equalized constellation symbols for each target UE

CHAPTER 6

MULTI-SERVICE COMMUNICATION SYSTEMS WITH UFMC-FDMA

In this chapter, we suggest the system structures based on (2.12) to support multi-service communications (MSC) with shared bandwidth. As viable solutions to support different services such as mMTC, URLLC in 5G network, combining signals, contain different numerology, in same frequency band has been considered in [51]. Similar to asynchronous uplink transmission, MSC destroy the orthogonality of signals by inter-services interference (ISVI). In [51], three types of subband filtering (e.g. RB-based, user-based, and service-based filtering) are proposed to support MSC with reducing the ISVI. In our approach, we develop the new receiver structure with service-based filtering by extending our previous research in [23]. We assume that MU signals in each services arrive at the BS within filter length. Moreover, the proposed receiver structures employ non-contiguous sub-band filters which reduce the number of required sub-band filters at the receiver. Based on the theoretical analysis of filter characteristics, we calculate the required filters to extract target service bands. In our approach, the number of baseband filters at the receiver can be significantly reduced compared to that of in [23]. The analysis of the proposed system performance has been illustrated with various scenarios along with the radio-over-fiber experiments results.

6.1 All-in-One Receiver design with service-based filtering

To support the MSC in (2.14), we consider the service-based filtering as illustrated in Fig. 6.1. If the allocated BW at each services is fixed, designing filters can be simple but leads to inefficient resource usage. To provide efficient resource management among multi-services with MU, we propose new sub-band filters to support flexible resource allocation.

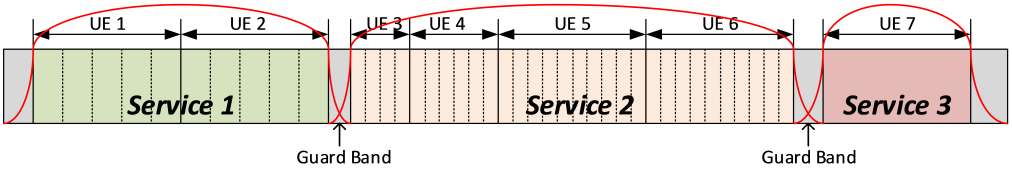

Figure 6.1: Service-based filtering technique to support MSC systems

6.1.1 Receiver Filter Design

We first analyze the prototype sub-band filters with Dolph-Chebyshev window. As we analyzed the properties of sub-band-based filters in Fig. 5.5, sharp cut-off frequency requires the longer filter-length. Moreover, the sub-band-based filtering techniques adopt continuous sub-band window (CSBW) allocation to cover given BW. Therefore, the number of filters is increasing for larger BW systems. Unlike to the CSBW at the receiver, we design a service-based filtering with using distributed subband-based windowing (DSBW) allocation. By analyzing the characteristic of the Dolph-Chebyshev filter, we determine the minimum required number of filters for the service k. The relationship between the filter BW and filter parameters are given as [63]

$$\begin{aligned} \gamma_{sv_k} &= \cosh\left(\frac{\cosh^{-1}\left(\frac{1}{\alpha_{sv_k}}\right)}{2L_{sv_k}}\right), \\ \beta_{sv_k} &= 2\cos^{-1}\left(\frac{1}{\gamma_{sv_k}}\right), \end{aligned} \tag{6.1}$$

where L_{sv_k} is the sub-band filter length in kth service, α_{sv_k} is the stop-band attenuation factor, and $\beta_{sv_k} \in [0, \pi]$ is the normalized single-side BW. As illustrated in Fig. 5.5, the wider sub-band filters with CSBW can contain not only target sub-bands signals but also interference from adjacent multi-services. To avoid IsvI and MsvI, the narrow filters are required by increasing the hardware complexity. To support MSC systems with reducing the hardware complexity, we suggest the filter structures with (6.1). Specifically, we minimize the overlapped sub-carriers among entire filtered sub-bands output with using following

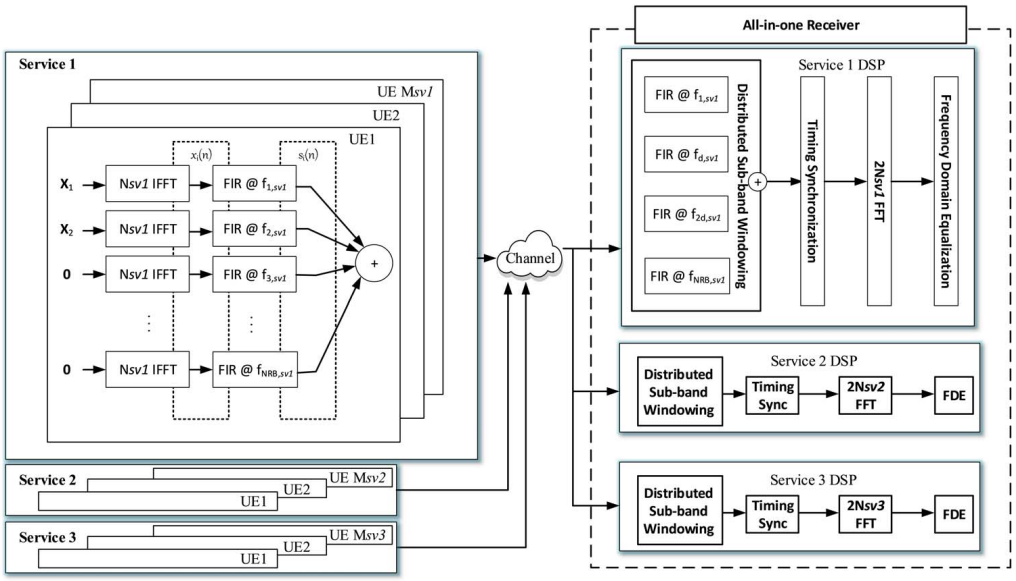

Figure 6.2: Proposed receiver structure to support multi-service communication

metrics as

$$\begin{aligned} N_{sv_k}^{sb} &= \frac{BW_{sv_k}}{\beta_{sv_k}}\pi, \\ g_{sv_k} &= \left\lfloor \frac{N_{sv_k}^{rb}}{N_{sv_k}^{sb}} \right\rfloor, \end{aligned} \tag{6.2}$$

where $N_{sv_k}^{sb}$ is the total number of sub-band filters to extract the kth service, BW_{sv_k} is the normalized BW allocated at the kth service, g_{sv_k} is the distance between adjacent filtered RB, $N_{sv_k}^{rb} = \frac{BW_{sv_k}}{\Delta f_k}$ is the allocated resource block, and Δf_k is the sub-carrier spacing for the kth services . Therefore, the DSBW contains group of sub-band filters as

$$\mathbf{f}_{sv_k} = [f_0, f_{g_{sv_k}}, f_{2g_{sv_k}}, \cdots, f_{N_{sv_k}^{sb} g_{sv_k}}]^T, \tag{6.3}$$

where the sub-band filter is defined in (2.10) with the center sub-carrier index $c_{g_{sv_k}}$ at the gth sub-band in the kth service.

6.1.2 Proposed Receiver Structure

By employing the service-based filtering with DSBW scheme in (6.3), the filtered signal for the kth service is written as

$$\begin{aligned}\tilde{r}_{sv_k}(n) &= \sum_{m=0}^{N_{sv_k}^{sb}} \sum_{l=0}^{L_{sv_k}-1} f_{mg_{sv_k}}(l) r(n-l) \\ &= \sum_{m=0}^{N_{sv_k}^{sb}} \sum_{l=0}^{L_{sv_k}-1} f_{mg_{sv_k}}(l) r_{sv_k}(n-\tau_{sv_k}-l) + \sum_{m=0}^{N_{sv_k}^{sb}} \sum_{l=0}^{L_{sv_k}-1} f_{mg_{sv_k}}(l) w(n-l), \quad (6.4)\end{aligned}$$

where we assume that MsvI and IsvI are perfectly removed from the DSBW. As shown in Fig.6.2, multi-user signals in each service are filtered with corresponding DSBW filter structure. Since we assume that CFO is pre-compensated at each UE before UL transmission and TAS is adopted for synchronous transmission among MU transmission in each service, UL signals do not require synchronization symbols. However, the coarse TO estimation may be required to compensate the time-varying propagation delay. But synchronous transmission among multi-services are not required.

6.1.3 Coarse Timing Estimation

In (6.4), the average TO τ_{sv_k} may be estimated and compensated to provide reliable system performance in fast time-varying channel. Since the UL signals are transmitted with using TAS, we use the filter ramp up/down properties of UFMC waveform as illustrated in Fig. 5.2. As the UFMC waveform has the filter ramp up/down at the beginning/end of each symbol, the relatively smaller signal energy at the certain region is expected. Thus, the proposed energy detection-based coarse synchronization method is written as following:

$$\begin{aligned}\Gamma_k(ii) &= \sum_{n=ii}^{ii+L_{sv_k}} |\tilde{r}_{sv_k}(n)|^2, \quad ii \in [0, N_{sv_k} + 2L_{sv_k} - 2], \\ \hat{\tau}_{sv_k} &= \arg\min_{ii}\{\Gamma_k(ii)\} - L_{sv_k}, \quad (6.5)\end{aligned}$$

where $\Gamma_k(ii)$ is the received signal energy at the iith lag, and $\hat{\tau}_{sv_k}$ is the estimate average TO for the kth service. Since another filtering at the receiver increases the length of filter ramp up/down, actual symbol/frame starting point is L_{sv_k} shifted from τ_{sv_k} in (6.5).

6.2 Simulation Results

In this section, we illustrate the solutions of asynchronous multi service with a different subcarrier spacing in single carrier frequency. Then, the performance of the proposed system is quantified through numerical simulations. The following configurations are considered to perform the simulations. The sampling frequency is set as 30.72 MHz for all services and users. We assume that the available bandwidth is 25 MHz which is uniformly divided into 3 different services. Thus, each service can utilize the 8.64 MHz bandwidth but different subcarrier spacings. Specifically, the 1th service utilizes the 288 number of active sub-carriers with 30 kHz sub-carrier spacing, $N_{sv_1} = 1024$-point IFFT, and $L_{sv_1} = 64$-length filter for 12 users. Then, the 576 number of active sub-carriers with 15 kHz sub-carrier spacing, $N_{sv_2} = 2048$, $L_{sv_2} = 128$, and 8 users are assigned for the 2th service. Finally, the 144 number of active sub-carriers is used with 60 kHz subcarrier spacing, 512-point IFFT, and $L_{sv_3} = 43$ with 6 users are assigned in the 3th service. Finally, 180 kHz guard bands are inserted between different services. Based on the filtering metric in (6.2), the distance between adjacent sub-band filters can be obtained as $g_{sv_1}, g_{sv_2}, g_{sv_3} = 2, 3, 2$, respectively.

Frequency division multiple access (FDMA) scheme is considered at each services for the multi-user scheduling. The training symbols for the channel estimation are modulated with QPSK while the data symbols are modulated with 16-QAM. The zero-forcing (ZF) equalizer is adopted as a simple 1-tap FDE and the channel is modeled as the extended vehicular A (EVA) model [60].

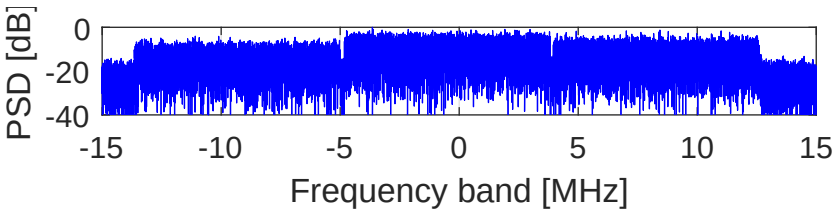

(a) PSD of received MSC signal

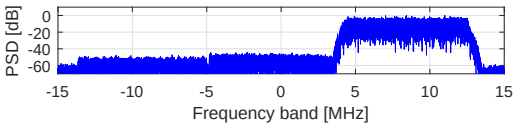

(b) PSD of the service 1 with the DSBW

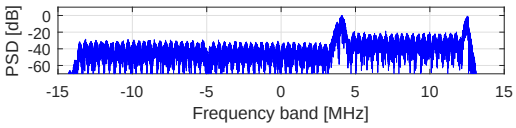

(c) PSD of the service 1 with the CSBW

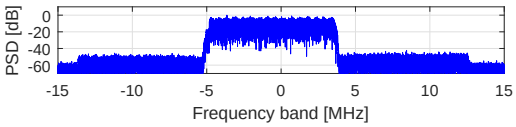

(d) PSD of the service 2 with the DSBW

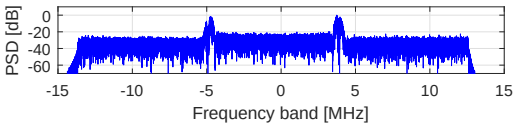

(e) PSD of the service 2 with the CSBW

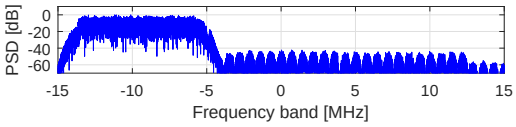

(f) PSD of the service 3 with the DSBW

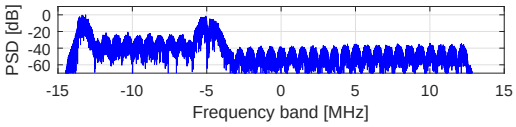

(g) PSD of the service 3 with the CSBW

Figure 6.3: The comparison of power spectrum density among filtered signals with the proposed DSBW and CSBW.

6.2.1 The performance of DSBW

In Fig. 6.3, the visualization of two different filtering techniques with using sub-band-based and service-based filtering are illustrated. To evaluate the performance of filters, multi-path channels are not considered. In Fig. 6.3 (a), the power spectrum density of multi-service MU received signals are illustrated. Both CSBW, and DSBW, we use sub-band filter parameters same as transmitter. We observe that the CSBW filtering contains not only target service signals but also adjacent services. In Fig. 6.3 (c), the CSBW reduced major MsvI and IsvI from other services. However, the filter outputs at edge still contains the adjacent service signals. In Fig. 6.3 (e), we observe interesting features that the CSBW reduce not only MsvI from adjacent services but also introduce self-interference. This results indicate that the summation of CSBW may not satisfy the orthogonality of each

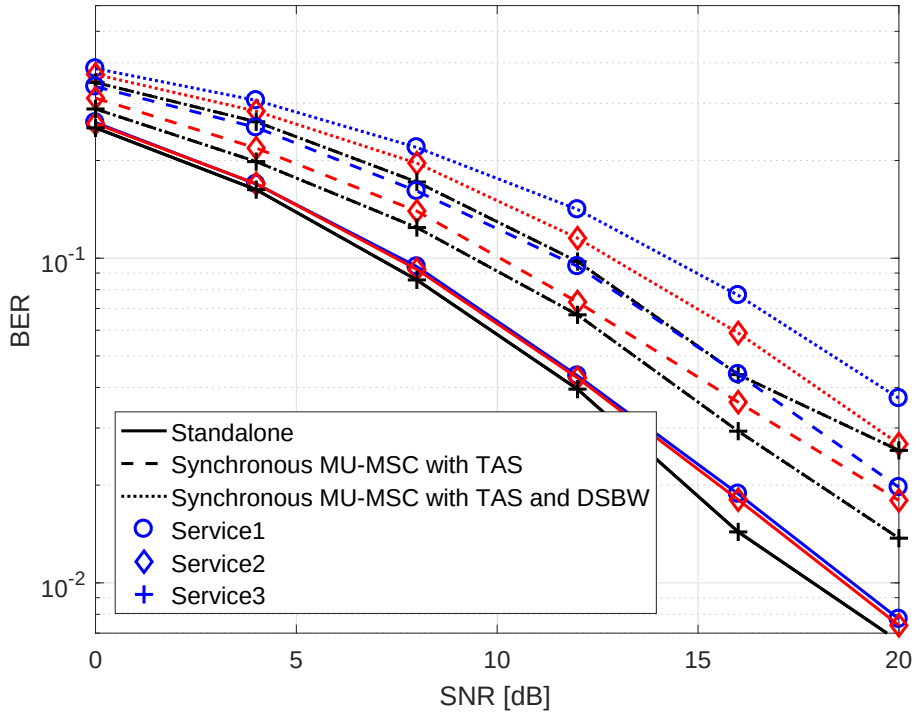

Figure 6.4: The comparison of bit-error-rate over various cases over multi-path fading channels.

sub-band signals. Similarly the self-interference is observed in Fig. 6.3 (g). However, the proposed DSBW scheme does not introduce the self-interference while reducing MsvI and IsvI. Since the proposed DSBW minimize the duplicated sub-carriers from adjacent sub-band filters, each services are clearly extracted as illustrated in Fig. 6.3 (b), (d), and (f).

6.2.2 The performance systems

In Fig. 6.4, the system performances are evaluated in terms of BER over various scenario. By using different radio frequency for each services, each service bands are protected from adjacent services. Therefore, the standalone can be considered as benchmark. We observe that the service 3 shows slight better performance from larger sub-carrier spacing. Without using any filtering techniques at the receiver, the synchronous multi-user UL transmission in MSC systems with using TAS show severe performance degradation. It is obvious that

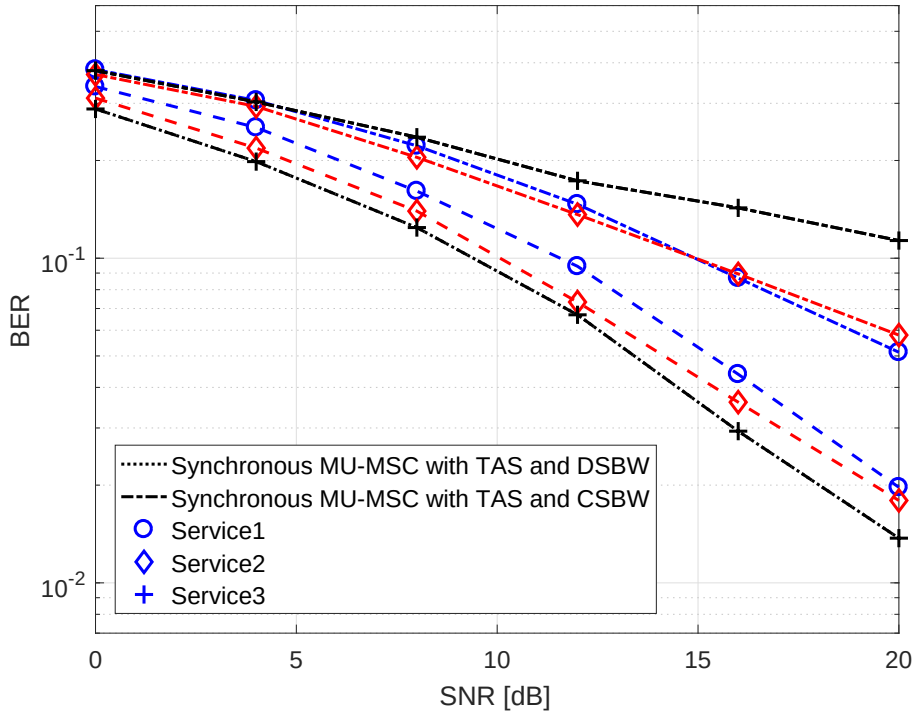

Figure 6.5: The comparison of bit-error-rate with using DSBW and CSBW.

combining multiple signals with different radio specification destroyed the orthogonality of signals by MsvI and IsvI. Although the proposed DSBW techniques cannot perfectly remove the MsvI and IsvI, the system performances show better than the MSC system without filtering. In Fig. 6.5, we also compare the BER performance with using DSBW and CSBW for service-based filtering in MSC systems. Generally, the CSBW techniques show worse system performance than using DSBW scheme. Specifically, the service-based filtering with using CSBW not only contains the adjacent multi-service signals but also introduces the self-interference. We observe the severe performance degradation for service 3 with using CSBW. This results indicate that the sub-band filters at service 3 have large main-lobe which leads increasing number of duplicated sub-carriers at each sub-band filters with different coefficient. Unlike to the CSBW scheme, the proposed DSBW scheme shows better performance by reducing the number of duplicated sub-carriers at filtered sub-band signals.

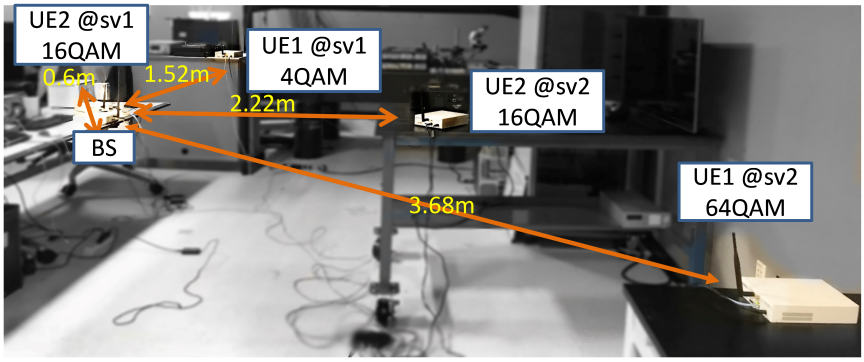

Figure 6.6: Testbed environment for multi-user and multi-service uplink transmission.

Table 6.1: UFMC system parameters in each services used at wireless test-bed

Parameter	Service 1	Service 2
Sampling Frequency	500 kHz	500 kHz
FFT Size	1024	2048
Filter Length	64	128
Sub-carrier Spacing	488 Hz	244 Hz
Symbol duration	2ms	4ms
Allocated bandwidth for each UE	35 kHz	17.5 kHz

6.3 Demonstration of Over-the-Air Transmission for MSC system

To demonstrate the proposed algorithm for supporting MSC with using same radio frequency, we design the wireless test-bed with using NI-USRP in section 5.4.1. System parameters for each services are presented in Table. 6.1. Due to the limitation of hardware, the sampling frequency is lower than current mobile devices. However, this demonstration proves the system concept as the prototype. We assume that the service 1 is satisfying the lower latency requirements from smaller TTI than the service 2. Specifically, the symbol duration for the service 1 is 2 ms while 4 ms for the service 2. 2 multi-users are considered in each services with different distance between BS and UEs. Finally, data symbols are modulated with QPSK, 16-QAM, and 64-QAM.

As illustrated in Fig. 6.7, the proposed systems can decode MU signals in each services by using the DSBW schemes. Since the test-bed only provides UL transmission, TAS

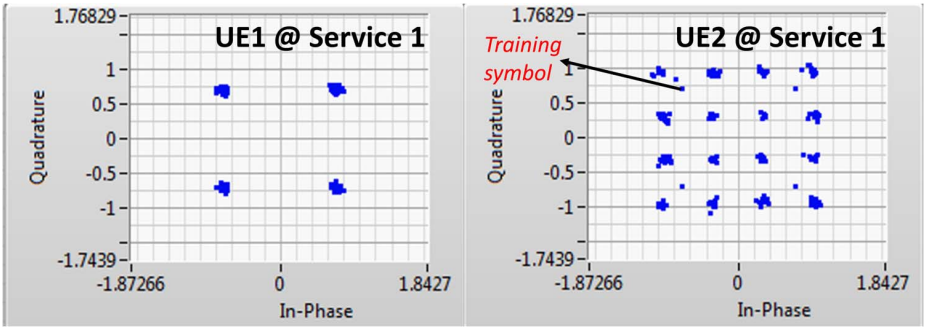

(a) Demodulated constellation for service 1

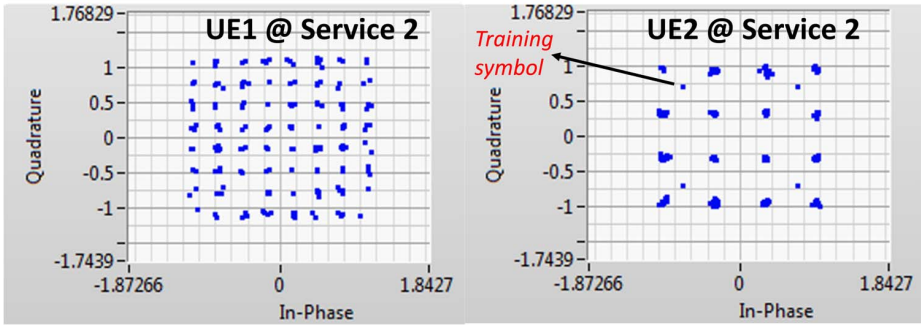

(b) Demodulated constellation for service 2

Figure 6.7: Demodulated constellation at the receiver with DSBW

cannot be applied. Therefore, we manually find the frame starting positions. Finally, QPSK modulated reference symbols are inserted for channel equalization.

CHAPTER 7
CONCLUDING REMARKS

7.1 Contributions

In this dissertation, we have presented joint timing and carrier frequency synchronization schemes for FBMC-OQAM and UFMC transmissions. We have presented that FBMC-OQAM and UFMC systems are more robust to synchronization mismatch compared to OFDM. However, TO and CFO still degrade the system performance from ISI and ICI. Since FBMC-OQAM and UFMC systems have different structures, the conventional synchronization for OFDM may not be applicable. Therefore, the objective of the proposed research was to analyze and develop synchronization algorithms for FBMC-OQAM and UFMC systems. The main contributions of this dissertation are illustrated as follow:

- We proposed joint TO and CFO estimation for FBMC-OQAM transmissions. Two uncorrelated and independent binary training sequences with null sub-carriers generate the repeated conjugate-symmetric property. By analyzing the correlation outputs of proposed training sequences, we developed new signal detection and coarse TO estimation algorithms. The proposed TO estimation algorithms do not require the threshold or the matched filters to detect training symbol. We also proposed the ratio-based CFO estimation schemes by analyzing two consecutive strong correlation gain. Since the proposed synchronization for FBMC-OQAM is developed with using two uncorrelated and independent training sequences, the proposed algorithms can be applicable for not only MIMO-STBC systems but also burst/continous transmission. Finally, the proposed method reduced the computational complexity than the existing schemes while providing similar system performance in SISO-FBMC.

- We presented a new joint timing and carrier frequency offsets estimation method for

UFMC systems. We suggested using the auto-correlation-based timing synchronization by exploiting the repeated conjugate-symmetric properties of training signals. We also proposed the criterion to select the filter parameters to keep the useful properties of training signals. To detect the training signals, we derived the statistical threshold by using Neyman-Pearson criterion as the reference. To simplify designing the threshold, we proposed a normalization schemes. Thus, receiver do not require estimating noise variance or received signal power to set the threshold. Moreover, we proposed an weight function to increase the accuracy of integer CFO estimation in frequency domain. Then, fractional CFO is estimated with suggested correlation region of received signals. Finally, the cell ID is detected with using local templates after compensating coarse TO and CFO.

- We presented a single resource block-based coarse TO estimation for asynchronous multi-user UL transmissions with using UFMC-FDMA systems. By analyzing the identical signal blocks in training symbol, the residual CFO of each UE is estimated. We also demonstrated over-the-air transmission with NI-USRP to prove the asynchronous UL transmission with proposed algorithms. Finally, the proposed filtering scheme, coarse TO estimation, and residual CFO estimation provide the resource block-based asynchronous multi-user UL transmissions.

- We developed the service-based filtering techniques to support multi-service communication. In multi-service communication systems, multiple numerology of systems are combined and shared single radio frequency to provide efficient resource management. We proposed the service-based filtering solution with using same sub-band filters in UFMC systems. By reducing the duplicated filtered sub-carriers at each sub-band outputs with using distributed sub-band filters, the proposed filtering schemes are outperformed than using continuous sub-band filters. Finally, we demonstrated the multi-service and multi-user transmission with using NI-USRP to evaluate the

proposed algorithms over-the-air transmission.

7.2 Future Research Topics

The following is a list of possible research topics as extensions of this dissertations:

- We have presented the synchronization methods for FBMC-OQAM systems. The proposed algorithms support both continuous/burst transmissions and MIMO-STBC systems. However, the integer CFO and cell search procedures are not considered. As extension of [36], we will develop the integer CFO estimation along with cell ID detection.

- We have presented the asynchronous UL transmission with using sub-band filtering-based schemes. Since low-latency communication is one of key features of 5G networks, the extension of the analysis to asynchronous UL transmission will be an interesting research topics. Specifically, future research topics include the analysis of grant-free multiple access scheme with UFMC for asynchronous and low latency UL transmissions.

APPENDIX A

PROOF OF PROPOSITION 1

Since the training block provides the repeated conjugate symmetry in (4.1), the distance between adjacent peaks of the correlation output in (3.8) is $\frac{N}{4}$. Thus, we only consider the correlation outputs when the correlation lag $l \in \{0, \frac{N}{4}, \frac{N}{2}, \frac{3N}{4}\}$ over multiple observation windows based on the overlapping factor V. We showed that the FBMC-OQAM transmitted blocks are consisted of previous signals with different the filter coefficients from (2.5) to (2.7). Since the proposed training sequences do not generate quadrature components, we only consider the inphase components of FBMC-OQAM signals. Therefore, the correlation outputs of training blocks can be derived in the absence of channel and noise as

$$
\begin{aligned}
& r_{\lfloor \frac{g}{4} \rfloor}[\psi_g] = \\
& \Bigg[\left(b^{TR}_{\lfloor \frac{g}{4} \rfloor, \psi_g} h_{\lfloor \frac{g}{4} \rfloor, \psi_g} + b^{TR}_{\lfloor \frac{g}{4} \rfloor + 1, \psi_g} h_{\lfloor \frac{g}{4} \rfloor - 1, \psi_g} \right), \\
& \left(b^{TR}_{\lfloor \frac{g}{4} \rfloor, \psi_g + 1} h_{\lfloor \frac{g}{4} \rfloor, \psi_g + 1} + b^{TR}_{\lfloor \frac{g}{4} \rfloor + 1, \psi_g + 1} h_{\lfloor \frac{g}{4} \rfloor - 1, \psi_g + 1} \right), \cdots \\
& , \left(b^{TR}_{\lfloor \frac{g}{4} \rfloor + 1, \psi_g - 1} h_{\lfloor \frac{g}{4} \rfloor + 1, \psi_g - 1} + b^{TR}_{\lfloor \frac{g}{4} \rfloor + 2, \psi_g - 1} h_{\lfloor \frac{g}{4} \rfloor, \psi_g - 1} \right) \Bigg], \\
& \times \Bigg[\left(b^{TR}_{\lfloor \frac{g}{4} \rfloor, \psi_g} h_{\lfloor \frac{g}{4} \rfloor + 2, \psi_g} + b^{TR}_{\lfloor \frac{g}{4} \rfloor + 1, \psi_g} h_{\lfloor \frac{g}{4} \rfloor + 1, \psi_g} \right), \\
& \left(b^{TR}_{\lfloor \frac{g}{4} \rfloor, \psi_g + 1} h_{\lfloor \frac{g}{4} \rfloor + 2, \psi_g - 1} + b^{TR}_{\lfloor \frac{g}{4} \rfloor + 1, \psi_g + 1} h_{\lfloor \frac{g}{4} \rfloor + 1, \psi_g - 1} \right), \cdots \\
& , \left(b^{TR}_{\lfloor \frac{g}{4} \rfloor + 1, \psi_g - 1} h_{\lfloor \frac{g}{4} \rfloor + 1, \psi_g + 1} + b^{TR}_{\lfloor \frac{g}{4} \rfloor + 2, \psi_g - 1} h_{\lfloor \frac{g}{4} \rfloor, \psi_g + 1} \right) \Bigg]^T,
\end{aligned}
\tag{A.1}
$$

where $\psi_g = \left(\frac{g}{4} - \lfloor \frac{g}{4} \rfloor \right) N$. By defining the correlation output in (3.8) as $r_{b, \lfloor \frac{g}{4} \rfloor}[\psi_g]$ when the pulse-shaper is a rectangular function ($h_{i,m_s} = 1,\ i \in [0, V-1],\ m_s \in [0, N-1]$),

(A.1) can be simplified based on (3.3) as follows:

$$\begin{aligned} r_{b,\lfloor \frac{g}{4} \rfloor}[\psi_g] = & \left| b^{TR}_{\lfloor \frac{g}{4} \rfloor, \psi_g} \right|^2 + \left| b^{TR}_{\lfloor \frac{g}{4} \rfloor + 1, \psi_g} \right|^2 \\ & + b^{TR}_{\lfloor \frac{g}{4} \rfloor, \psi_g} b^{TR}_{\lfloor \frac{g}{4} \rfloor + 1, \psi_g} + b^{TR}_{\lfloor \frac{g}{4} \rfloor, \psi_g} b^{TR}_{\lfloor \frac{g}{4} \rfloor + 1, \psi_g} \\ & + \cdots + \left| b^{TR}_{\lfloor \frac{g}{4} \rfloor + 1, \psi_g - 1} \right|^2 + \left| b^{TR}_{\lfloor \frac{g}{4} \rfloor + 2, \psi_g - 1} \right|^2 \\ & + b^{TR}_{\lfloor \frac{g}{4} \rfloor + 1, \psi_g - 1} b^{TR}_{\lfloor \frac{g}{4} \rfloor + 2, \psi_g - 1} \\ & + b^{TR}_{\lfloor \frac{g}{4} \rfloor + 1, \psi_g - 1} b^{TR}_{\lfloor \frac{g}{4} \rfloor + 2, \psi_g - 1}. \end{aligned} \tag{A.2}$$

If two training symbols are identical ($A^{TR}_{0,n} = A^{TR}_{1,n}$) $\quad \forall n$, then $r_{b,\lfloor \frac{g}{4} \rfloor}[\psi_g]$ shows the correlation gain at certain region as following properties

$$\begin{aligned} & r_{b,\lfloor \frac{g}{4} \rfloor}[\psi_g] = VE_T, \quad \forall g \in \{2V-4, \cdots, 2V\}, \\ & r_{b,\lfloor \frac{g}{4} \rfloor}[\psi_g] < VE_T, \quad 2V-6 \leq g < 2V-4,\ 2V < g \leq 3V, \\ & r_{b,\lfloor \frac{g}{4} \rfloor}[\psi_g] \simeq 0, \qquad \text{otherwise}, \end{aligned} \tag{A.3}$$

where E_T is the transmitted energy of the block defined as

$$E_T \triangleq \frac{1}{N} \sum_{m_s=0}^{N-1} b_{0,m_s} b^*_{0,m_s} = \frac{1}{N} \sum_{n=0}^{N-1} |b_{0,m_s}|^2. \tag{A.4}$$

Since the prototype filter response h_{i,m_s} in [12] illustrated in Fig. A.1 is not flat but symmetric both in time and frequency domain, the properties in (A.3) can be changed depends on the energy of the filter response. Specifically, the main lobe of the waveform contains dominant energy. Therefore, the signal with including the main lobe will provide the highest correlation gain. By defining the correlation output in Eq. (3.8) as $r_{h,k}[l]$ when two identical training symbols are set as $A^{TR}_{0,n} = A^{TR}_{1,n} = 1$, $r_{h,k}[l]$ provides following

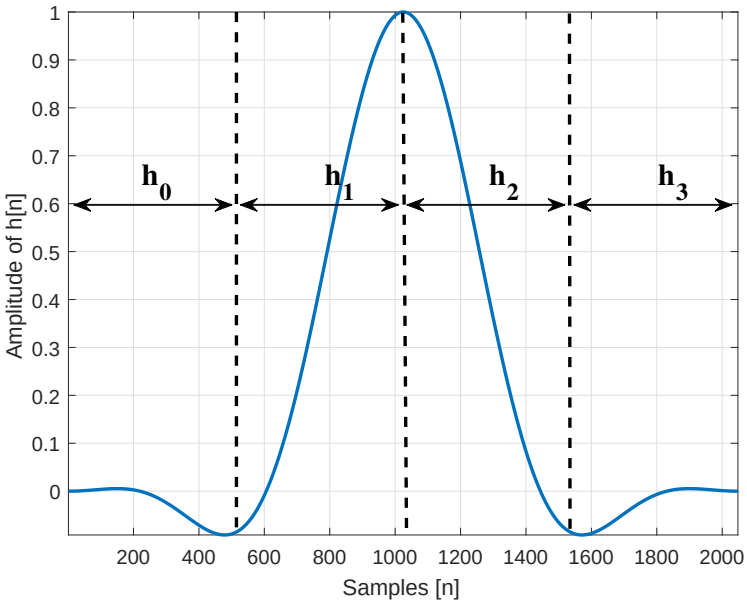

Figure A.1: The visualization of the prototype filter response of $h[n]$ with $V = 4$ in (2.6). The $N \times 1$ filter response vectors $\mathbf{h}_1$ and $\mathbf{h}_2$ contain the main lobe of waveform.

properties

$$r_{h,\frac{V}{2}-2}\left[\frac{3}{4}N\right] < r_{h,\frac{V}{2}-1}[0] < r_{h,\frac{V}{2}-1}\left[\frac{N}{4}\right] < r_{h,\frac{V}{2}-1}\left[\frac{N}{2}\right], \tag{A.5}$$

where $r_{h,\frac{V}{2}-1}\left[\frac{N}{4}\right]$ and $r_{h,\frac{V}{2}-1}\left[\frac{N}{2}\right]$ contain the portion of main lobe of the waveform from two identical signal blocks. Moreover, following properties are provided from the symmetry of the filter response $h_{m,n}$

$$\begin{aligned} r_{h,\frac{V}{2}-2}\left[\frac{3}{4}N\right] &= r_{h,\frac{V}{2}}\left[\frac{N}{4}\right], \\ r_{h,\frac{V}{2}-1}\left[\frac{N}{4}\right] &= r_{h,\frac{V}{2}-1}\left[\frac{3}{4}N\right], \\ r_{h,\frac{V}{2}-1}[0] &= r_{h,\frac{V}{2}}[0]. \end{aligned} \tag{A.6}$$

According to Eq. (A.3) - (A.6), we derive the following property by using Cauchy-Schwarz

inequality

$$r_{\lfloor \frac{g}{4} \rfloor} [\psi_g]^2 \leq r_{b,\lfloor \frac{g}{4} \rfloor} [\psi_g]^2 r_{h,\lfloor \frac{g}{4} \rfloor} [\psi_g]^2 . \tag{A.7}$$

Finally, we prove Proposition 1 as

$$\begin{aligned} &\left(\left| r_{\frac{V}{2}-2} \left[\frac{3}{4} N \right] \right| \simeq \left| r_{\frac{V}{2}} \left[\frac{1}{4} N \right] \right| \right) < \left(\left| r_{\frac{V}{2}-1} [0] \right| \simeq \left| r_{\frac{V}{2}} [0] \right| \right) \\ < &\left(\left| r_{\frac{V}{2}-1} \left[\frac{1}{4} N \right] \right| \simeq \left| r_{\frac{V}{2}-1} \left[\frac{3}{4} N \right] \right| \right) < \left| r_{\frac{V}{2}-1} \left[\frac{N}{2} \right] \right| . \end{aligned} \tag{A.8}$$

■

APPENDIX B

PROOF OF PROPOSITION 2

If two consecutive training symbols are uncorrelated and independent, the sum of the product of two training blocks in (A.2) is written as

$$\frac{1}{N}\sum_{m_s=0}^{N-1} b_{0,m_s} b_{1,m_s} \simeq 0. \tag{B.1}$$

Since two consecutive training blocks are uncorrelated, overlapped adjacent training blocks which contain the portion of the main lobe of waveform do not increase the correlation gain. Therefore, the properties in (A.5) are rewritten as

$$\begin{aligned} r_{h,\frac{V}{2}-2}\left[\frac{3}{4}N\right] &\simeq r_{h,\frac{V}{2}-1}\left[\frac{N}{4}\right] < r_{h,\frac{V}{2}-1}[0], \\ r_{h,\frac{V}{2}-1}\left[\frac{3}{4}N\right] &\simeq r_{h,\frac{V}{2}}\left[\frac{N}{4}\right] < r_{h,\frac{V}{2}}[0], \\ r_{h,\frac{V}{2}-1}\left[\frac{N}{2}\right] &\simeq 0. \end{aligned} \tag{B.2}$$

Similar as Proposition 1, Cauchy-Schwarz inequality leads to

$$\begin{aligned} \left(r_{\frac{V}{2}-2}\left[\frac{3N}{4}\right] \simeq r_{\frac{V}{2}-1}\left[\frac{N}{4}\right]\right) &< r_{\frac{V}{2}-1}[0], \\ \left(r_{\frac{V}{2}-1}\left[\frac{3N}{4}\right] \simeq r_{\frac{V}{2}}\left[\frac{N}{4}\right]\right) &< r_{\frac{V}{2}}[0]. \end{aligned} \tag{B.3}$$

Finally, the unique peak patterns are repeated from two uncorrelated and independent training sequences where the highest peaks are located at $r_{\frac{V}{2}-1}[0]$ and $r_{\frac{V}{2}}[0]$. ■

APPENDIX C

PROOF OF PROPOSITION 3

As shown in (2.9), the bth sub-band FIR filter coefficients $f_b(l)$ contain frequency shift components Θ_b. Then the inner product of adjacent frequency shift components are defined as

$$\begin{aligned} |\left\langle \boldsymbol{\Theta}_b, \boldsymbol{\Theta}_{b+1} \right\rangle| &= \left| \sum_{n=0}^{L-1} \exp\left(j2\pi \frac{c_b - c_{b+1}}{N} n \right) \right| \\ &= \left| \sum_{n=0}^{L-1} \exp\left(j2\pi \frac{N_{sc}}{N} n \right) \right|, \end{aligned} \tag{C.1}$$

where c_b is the center sub-carrier index of the bth sub-band. We can easily show the orthogonality of different filter coefficients as

$$\left\langle \boldsymbol{\Theta}_b, \boldsymbol{\Theta}_{b+1} \right\rangle \simeq \begin{cases} 0, & \text{for } \; c_b \neq c_{b+1} \\ L, & \text{for } \; c_b = c_{b+1} \end{cases}, \text{if } L = N/\kappa,$$

$$\left\langle \boldsymbol{f}_b, \boldsymbol{f}_{b+1} \right\rangle = \left\langle \boldsymbol{f} \odot \boldsymbol{\Theta}_b, \boldsymbol{f} \odot \boldsymbol{\Theta}_{b+1} \right\rangle \simeq \begin{cases} 0, & \text{for } \; c_b \neq c_{b+1} \\ E_f, & \text{for } \; c_b = c_{b+1} \end{cases}, \text{if } L = N/\kappa, \tag{C.2}$$

where κ is a positive divisor of N_{sc}. Therefore, the orthogonality condition can be maintained with minimizing the interference when the filter length L is choose based on Proposition 1. Finally, so the preamble structure of $x_b[n]$ in (2.9) can be maintained because of the linearity of orthogonal signal. ■

REFERENCES

[1] 3rd Generation Partnership Project (3GPP); Technical Specification Group, "LTE evolved universal terrestrial radio access (E-UTRA) physical channels and modulation (release 8)," *3GPP TS 36.211, V8.9.0.*, pp. 1–83, Jan. 2010.

[2] "IEEE standard for information technology-telecommunications and information exchange between systems local and metropolitan area networks-specific requirements part 11: Wireless lan medium access control (MAC) and physical layer (PHY)," *IEEE Std 802.11-2012*, pp. 1–91, Jun. 2012.

[3] M. Speth, S. A. Fechtel, G. Fock, and H. Meyr, "Optimum receiver design for wireless broad-band systems using OFDM. i," *IEEE Transactions on Communications*, vol. 47, no. 11, pp. 1668–1677, 1999.

[4] J. V. D. Beek and F. Berggren, "Out-of-band power suppression in OFDM," *IEEE Communications Letters*, vol. 12, no. 9, pp. 609–611, 2008.

[5] L. Zhang, A. Ijaz, P. Xiao, and R. Tafazolli, "Multi-service system: An enabler of flexible 5G air interface," *IEEE Communications Magazine*, vol. 55, no. 10, pp. 152–159, 2017.

[6] 3rd Generation Partnership Project (3GPP); Technical Specification Group Radio Access Network, "NR physical channels and modulation (release 15)," *3GPP TS 38.211, V15.3.0.*, pp. 1–96, Sep. 2018.

[7] A. Osseiran, F. Boccardi, V. Braun, K. Kusume, P. Marsch, M. Maternia, O. Queseth, M. Schellmann, H. Schotten, H. Taoka, H. Tullberg, M. A. Uusitalo, B. Timus, and M. Fallgren, "Scenarios for 5G mobile and wireless communications: The vision of the METIS project," *IEEE Communications Magazine*, vol. 52, no. 5, pp. 26–35, 2014.

[8] G. Wunder, P. Jung, M. Kasparick, T. Wild, F. Schaich, Y. Chen, S. T. Brink, I. Gaspar, N. Michailow, A. Festag, L. Mendes, N. Cassiau, D. Ktenas, M. Dryjanski, S. Pietrzyk, B. Eged, P. Vago, and F. Wiedmann, "5GNOW: Non-orthogonal, asynchronous waveforms for future mobile applications," *IEEE Commun. Mag.*, vol. 52, no. 2, pp. 97–105, Feb. 2014.

[9] 3rd Generation Partnership Project (3GPP); "Study on scenarios and requirements for next generation access technologies," *3GPP TR 38.913, V. 0.3.0*, Feb. 2016.

[10] P. Siohan, C. Siclet, and N. Lacaille, "Analysis and design of OFDM/OQAM systems based on filterbank theory," *IEEE Trans. Signal Process.*, vol. 50, no. 5, pp. 1170–1183, 2002.

[11] B. Farhang-Boroujeny, "OFDM versus filter bank multicarrier," *IEEE Signal Process. Mag.*, vol. 28, no. 3, pp. 92–112, 2011.

[12] M Bellanger, D Le Ruyet, D Roviras, M Terré, J Nossek, L Baltar, Q Bai, D Waldhauser, M Renfors, T Ihalainen, *et al.*, "FBMC physical layer: A primer," *PHYDYAS*, 2010.

[13] A. Viholainen, T. Ihalainen, T. H. Stitz, M. Renfors, and M. Bellanger, "Prototype filter design for filter bank based multicarrier transmission," in *Proc. 17th European Signal Processing Conference*, Glasgow, Scotland, Aug. 2009, pp. 1359–1363.

[14] P. Banelli, S. Buzzi, G. Colavolpe, A. Modenini, F. Rusek, and A. Ugolini, "Modulation formats and waveforms for 5G networks: Who will be the heir of OFDM?: An overview of alternative modulation schemes for improved spectral efficiency," *IEEE Signal Processing Magazine*, vol. 31, no. 6, pp. 80–93, 2014.

[15] R. Gerzaguet, D. Demmer, J. B. Dore, and D. Ktienas, "Block-filtered OFDM: A new promising waveform for multi-service scenarios," in *Proc. IEEE Int. Conf. Communications (ICC)*, May 2017, pp. 1–6.

[16] W. Chung, B. Kim, M. Choi, H. Nam, H. Yu, S. Choi, and D. Hong, "Synchronization error in QAM-based FBMC system," in *Proc. IEEE Military Communications Conference (MILCOM)*, Baltimore, MD, Oct. 2014, pp. 699–705.

[17] H. Lin, M. Gharba, and P. Siohan, "Impact of time and carrier frequency offsets on the FBMC/OQAM modulation scheme," *Signal Processing*, vol. 102, pp. 151–162, Sep. 2014.

[18] V. Vakilian, T. Wild, F. Schaich, S. ten Brink, and J. F. Frigon, "Universal-filtered multi-carrier technique for wireless systems beyond LTE," in *Proc. IEEE Globecom Workshops*, Atlanta, GA, 2013, pp. 223–228.

[19] F. Schaich, T. Wild, and Y. Chen, "Waveform contenders for 5G - suitability for short packet and low latency transmissions," in *Proc. IEEE 79th Vehicular Technology Conf. (VTC Spring)*, 2014, pp. 1–5.

[20] T. Wild, F. Schaich, and Y. Chen, "5G air interface design based on universal filtered (UF-)OFDM," in *Proc. 19th International Conference on Digital Signal Processing*, Hong Kong, 2014, pp. 699–704.

[21] 5th Generation Non-Orthogonal Waveforms for Asynchronous Signalling (5GNOW), "5G waveform candidate selection," *5GNOW, D3.2, v1.3*, pp. 1–100, Aug. 2014.

[22] R. Gerzaguet, N. Bartzoudis, L. G. Baltar, V. Berg, J.-B. Doré, D. Kténas, O. Font-Bach, X. Mestre, M. Payaró, M. Färber, *et al.*, "The 5g candidate waveform race: A comparison of complexity and performance," *EURASIP Journal on Wireless Communications and Networking*, vol. 2017, no. 1, p. 13, 2017.

[23] H. Cho, Y. Yan, G. K. Chang, and X. Ma, "Asynchronous multi-user uplink transmissions for 5G with UFMC waveform," in *Proc. IEEE Wireless Communications and Networking Conference (WCNC)*, San Francisco, CA, 2017, pp. 1–5.

[24] S. A. Cheema, K. Naskovska, M. Attar, B. Zafar, and M. Haardt, "Performance comparison of space time block codes for different 5g air interface proposals," in *WSA 2016; 20th International ITG Workshop on Smart Antennas*, 2016, pp. 1–7.

[25] A. Aminjavaheri, A. Farhang, A. RezazadehReyhani, and B. Farhang-Boroujeny, "Impact of timing and frequency offsets on multicarrier waveform candidates for 5G," in *Proc. IEEE Signal Processing and Signal Processing Education Workshop (SP/SPE),*, Salt Lake City, UT, 2015, pp. 178–183.

[26] X. Wang, T. Wild, and F. Schaich, "Filter optimization for carrier-frequency- and timing-offset in universal filtered multi-carrier systems," in *2015 IEEE 81st Vehicular Technology Conference (VTC Spring)*, 2015, pp. 1–6.

[27] H. Minn, V. K. Bhargava, and K. B. Letaief, "A robust timing and frequency synchronization for OFDM systems," *IEEE Transactions on Wireless Communications*, vol. 2, no. 4, pp. 822–839, 2003.

[28] H. Bölcskei, "Blind estimation of symbol timing and carrier frequency offset in wireless OFDM systems," *IEEE Trans. Commun.*, vol. 49, no. 6, pp. 988–999, Jun. 2001.

[29] T. Fusco and M. Tanda, "Blind frequency-offset estimation for OFDM/OQAM systems," *IEEE Trans. Signal Process.*, vol. 55, no. 5, pp. 1828–1838, 2007.

[30] T. Fusco, A. Petrella, and M. Tanda, "Non-data-aided carrier-frequency offset estimation for pulse-shaping OFDM/OQAM systems," *Signal Processing*, vol. 88, no. 8, pp. 1958–1970, Aug. 2008.

[31] T. Fusco, A. Petrella, and M. Tanda, "Data-aided symbol timing and CFO synchronization for filter bank multicarrier systems," *IEEE Trans. Wireless Commun.*, vol. 8, no. 5, pp. 2705–2715, 2009.

[32] D. Mattera and M. Tanda, "Data-aided synchronization for OFDM/OQAM systems," *Signal Processing*, vol. 92, no. 9, pp. 2284–2292, Sep. 2012.

[33] Y. Zeng and M. W. Chia, "Joint time-frequency synchronization and channel estimation for FBMC," in *Proc. IEEE 25th Annual International Symposium on Personal, Indoor, and Mobile Radio Communication (PIMRC)*, 2014, pp. 438–442.

[34] W. Chung, C. Kim, S. Choi, and D. Hong, "Synchronization sequence design for FBMC/OQAM systems," *IEEE Transactions on Wireless Communications*, vol. 15, no. 10, pp. 7199–7211, 2016.

[35] M. Renfors, T. Ihalainen, and T. H. Stitz, "A block-Alamouti scheme for filter bank based multicarrier transmission," in *European Wireless Conference (EW)*, Lucca, Italy, Apr. 2010, pp. 1031–1037.

[36] H. Cho and X. Ma, "Generalized synchronization algorithms for FBMC-OQAM systems," *IEEE Transactions on Vehicular Technology*, vol. 67, no. 10, pp. 9764–9774, Oct. 2018.

[37] P. H. Moose, "A technique for orthogonal frequency division multiplexing frequency offset correction," *IEEE Trans. Commun.*, vol. 42, no. 10, pp. 2908–2914, Oct. 1994.

[38] T. M. Schmidl and D. C. Cox, "Robust frequency and timing synchronization for OFDM," *IEEE Trans. Commun.*, vol. 45, no. 12, pp. 1613–1621, Dec. 1997.

[39] H. Minn, M. Zeng, and V. K. Bhargava, "On timing offset estimation for OFDM systems," *IEEE Commun. Lett.*, vol. 4, no. 7, pp. 242–244, Jul. 2000.

[40] B. Park, H. Cheon, C. Kang, and D. Hong, "A novel timing estimation method for OFDM systems," *IEEE Communications Letters*, vol. 7, no. 5, pp. 239–241, 2003.

[41] F. Tufvesson, O. Edfors, and M. Faulkner, "Time and frequency synchronization for OFDM using PN-sequence preambles," in *Gateway to 21st Century Communications Village. VTC 1999-Fall. IEEE VTS 50th Vehicular Technology Conference (Cat. No.99CH36324)*, vol. 4, 1999, 2203–2207 vol.4.

[42] C. Wang and H. Wang, "On joint fine time adjustment and channel estimation for ofdm systems," *IEEE Transactions on Wireless Communications*, vol. 8, no. 10, pp. 4940–4944, 2009.

[43] D. Chu, "Polyphase codes with good periodic correlation properties," *IEEE Trans. Inf. Theory,*, vol. 18, no. 4, pp. 531–532, Jul. 1972.

[44] M. M. U. Gul, X. Ma, and S. Lee, "Timing and frequency synchronization for OFDM downlink transmissions using Zadoff-Chu sequences," *IEEE Trans. Wireless Commun.*, vol. 14, no. 3, pp. 1716–1729, Mar. 2015.

[45] Y. Li, B. Tian, K. Yi, and Q. Yu, "An efficient and hybrid timing offset estimation approach for universal-filtered multi-carrier based systems over multipath rayleigh fading channel," *Digital Signal Processing*, vol. 73, pp. 128 –134, 2018.

[46] 3rd Generation Partnership Project (3GPP); Technical Specification Group Radio Access Network, "Evolved universal terrestrial radio access (E-UTRA) physical layer procedures (release 10)," *3GPP TS 36.213, V10.2.0.*, pp. 1–120, 2011.

[47] R. Knopp, F. Kaltenberger, C. Vitiello, and M. Luise, "Universal filtered multicarrier for machine type communications in 5G," in *European Conference on Networks and Communications (EUCNC)*, Athens, Greece, 2016.

[48] Y. Chen, F. Schaich, and T. Wild, "Multiple access and waveforms for 5G: IDMA and Universal Filtered Multi-Carrier," in *Proc. IEEE 79th Vehicular Technology Conference (VTC Spring)*, Seoul, Korea, 2014, pp. 1–5.

[49] A. A. Zaidi, R. Baldemair, H. Tullberg, H. Bjorkegren, L. Sundstrom, J. Medbo, C. Kilinc, and I. D. Silva, "Waveform and numerology to support 5G services and requirements," *IEEE Communications Magazine*, vol. 54, no. 11, pp. 90–98, Nov. 2016.

[50] X. Zhang, M. Jia, L. Chen, J. Ma, and J. Qiu, "Filtered-OFDM-enabler for flexible waveform in the 5th generation cellular networks," in *Proc. IEEE Global Communications Conference (GLOBECOM)*, San Diega, CA, Dec. 2015, pp. 1–6.

[51] L. Zhang, A. Ijaz, P. Xiao, A. Quddus, and R. Tafazolli, "Subband filtered multi-carrier systems for multi-service wireless communications," *IEEE Transactions on Wireless Communications*, vol. 16, no. 3, pp. 1893–1907, Mar. 2017.

[52] G. A. Shah, V. C. Gungor, and O. B. Akan, "A cross-layer QoS-aware communication framework in cognitive radio sensor networks for smart grid applications," *IEEE Transactions on Industrial Informatics*, vol. 9, no. 3, pp. 1477–1485, 2013.

[53] S. H. R. Bukhari, M. H. Rehmani, and S. Siraj, "A survey of channel bonding for wireless networks and guidelines of channel bonding for futuristic cognitive radio sensor networks," *IEEE Communications Surveys Tutorials*, vol. 18, no. 2, pp. 924–948, 2016.

[54] H. J. Cho, H. Cho, X. Mu, F. Lu, S. Shen, X. Ma, and G. Chang, "Asynchronous transmission using universal filtered multicarrier for multiservice applications in 5G fiber-wireless integrated mobile fronthaul," in *2018 Optical Fiber Communications Conference and Exposition (OFC)*, 2018, pp. 1–3.

[55] M. Tanda, "Blind symbol-timing and frequency-offset estimation in OFDM systems with real data symbols," *IEEE Trans. Commun.*, vol. 52, no. 10, pp. 1609–1612, Oct. 2004.

[56] D. Mattera and M. Tanda, "Blind symbol timing and CFO estimation for OFDM/OQAM systems," *IEEE Trans. Wireless Commun.*, vol. 12, no. 1, pp. 268–277, Jan. 2013.

[57] Q. Wang, C. Qian, X. Guo, Z. Wang, D. G. Cunningham, and I. H. White, "Layered ACO-OFDM for intensity-modulated direct-detection optical wireless transmission," *Optics express*, vol. 23, no. 9, pp. 12 382–12 393, 2015.

[58] S. M. Kay, *Fundamentals of Statistical Signal Processing, Volume II: Detection Theory*. PRENTICE HALL, Feb. 11, 1998, 672 pp., ISBN: 013504135X.

[59] S. I. Abramowitz M., *Handbook of Mathematical Functions with Formulas, Graphs, and Mathematical Tables*. U.S. Department of Commerce, NIST, 1974, ISBN: N/A.

[60] 3rd Generation Partnership Project (3GPP); Technical Specification Group, "LTE evolved universal terrestrial radio access (E-UTRA) base station (bs) radio transmission and reception (release 8)," *3GPP TS 36.104, V8.2.0.*, pp. 1–83, Jan. 2008.

[61] "Part 11 : Wireless LAN medium access control (MAC) and physical layer (PHY) specifications," *IEEE Std 802.11a-1999 (R2003)*, pp. 1–2793, Mar. 2003.

[62] F. Classen and H. Meyr, "Frequency synchronization algorithms for OFDM systems suitable for communication over frequency selective fading channels," in *Proceedings of IEEE Vehicular Technology Conference (VTC)*, 1994, 1655–1659 vol.3.

[63] P. Lynch, "The Dolph–Chebyshev window: A simple optimal filter," *Monthly weather review*, vol. 125, no. 4, pp. 655–660, 1997.

VITA

Hyunwoo Cho received the B.S degree in Information and Communication Engineering from Hanyang University, Seoul, Korea, in 2012. He is currently working towards the Ph.D degree in the School of Electrical and Computer Engineering at Georgia Institute of Technology, Atlanta, GA. His current research interests include timing and carrier frequency synchronization for multicarrier systems, design reference signals and detection algorithms in next generation wireless networks.